




















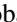






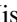









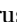









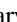






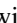


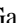


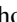



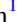




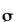

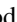












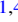

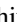

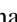






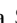

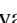








Kilonova Luminosity Function Constraints Based on Zwicky Transient Facility Searches for 13 Neutron Star Merger Triggers during O3

Mansi M. Kasliwal¹ , Shreya Anand¹ , Tomás Ahumada² , Robert Stein^{3,4} , Ana Sagués Carracedo⁵ , Igor Andreoni¹ , Michael W. Coughlin^{1,6} , Leo P. Singer^{7,8} , Erik C. Kool⁹ , Kishalay De¹ , Harsh Kumar¹⁰ , Mouza AlMualla¹¹ , Yuhan Yao¹ , Mattia Bulla¹² , Dougal Dobie^{13,14,15} , Simeon Reusch^{3,4} , Daniel A. Perley¹⁶ , S. Bradley Cenko^{7,8} , Varun Bhalerao¹⁰ , David L. Kaplan¹⁷ , Jesper Sollerman⁹ , Ariel Goobar⁵ , Christopher M. Copperwheat¹⁶ , Eric C. Bellm¹⁸ , G. C. Anupama¹⁹ , Alessandra Corsi²⁰ , Samaya Nisanke²¹ , Iván Agudo²² , Ashot Bagdasaryan¹ , Sudhanshu Barway¹⁹ , Justin Belicki²³ , Joshua S. Bloom^{24,25} , Bryce Bolin¹ , David A. H. Buckley²⁶ , Kevin B. Burdge¹ , Rick Burrows²³ , Maria D. Caballero-García²⁷ , Chris Cannella¹ , Alberto J. Castro-Tirado^{22,28} , David O. Cook²⁹ , Jeff Cooke^{15,30} , Virginia Cunningham² , Aishwarya Dahiwalé¹ , Kunal Deshmukh¹⁰ , Simone Dichiarà^{2,7} , Dmitry A. Duev¹ , Anirban Dutta¹⁹ , Michael Feeney²³ , Anna Franckowiak³ , Sara Frederick² , Christoffer Fremming¹ , Avishay Gal-Yam³¹ , Pradip Gatkine² , Shaon Ghosh³² , Daniel A. Goldstein^{1,54} , V. Zach Golkhou^{18,33,55} , Matthew J. Graham¹ , Melissa L. Graham¹ , Matthew J. Hankins¹ , George Helou³⁴ , Youdong Hu^{22,35} , Wing-Huen Ip³⁶ , Amruta Jaodand¹ , Viraj Karambelkar¹ , Albert K. H. Kong³⁷ , Marek Kowalski^{38,39} , Maitreya Khandagale¹⁰ , S. R. Kulkarni¹ , Brajesh Kumar¹⁹ , Russ R. Laher³⁴ , K. L. Li³⁷ , Ashish Mahabal^{1,40} , Frank J. Masci³⁴ , Adam A. Miller^{41,42} , Moses Mogotsi^{26,43} , Siddharth Mohite^{17,56} , Kunal Mooley¹ , Przemek Mroz¹ , Jeffrey A. Newman⁴⁴ , Chow-Choong Ngeow³⁶ , Samantha R. Oates⁴⁵ , Atharva Sunil Patil³⁶ , Shashi B. Pandey⁴⁶ , M. Pavana¹⁹ , Elena Pian⁴⁷ , Reed Riddle²³ , Rubén Sánchez-Ramírez⁴⁸ , Yashvi Sharma¹ , Avinash Singh¹⁹ , Roger Smith²³ , Maayane T. Soumagnac^{49,50} , Kirsty Taggart¹⁶ , Hanjie Tan³⁶ , Anastasios Tzanidakis¹ , Eleonora Troja^{2,7} , Azamat F. Valeev⁵¹ , Richard Walters²³ , Gaurav Waratkar¹⁰ , Sara Webb^{15,30} , Po-Chieh Yu³⁶ , Bin-Bin Zhang^{52,53} , Rongpu Zhou⁴⁹ , and Jeffry Zolkower²³ 

¹ Division of Physics, Mathematics, and Astronomy, California Institute of Technology, Pasadena, CA 91125, USA

² Department of Astronomy, University of Maryland, College Park, MD 20742, USA

³ Deutsches Elektronen Synchrotron DESY, Platanenallee 6, D-15738 Zeuthen, Germany

⁴ Institut für Physik, Humboldt-Universität zu Berlin, D-12489 Berlin, Germany

⁵ The Oskar Klein Centre, Department of Physics, Stockholm University, AlbaNova, SE-106 91 Stockholm, Sweden

⁶ School of Physics and Astronomy, University of Minnesota, Minneapolis, MN 55455, USA

⁷ Astrophysics Science Division, NASA Goddard Space Flight Center, MC 661, Greenbelt, MD 20771, USA

⁸ Joint Space-Science Institute, University of Maryland, College Park, MD 20742, USA

⁹ The Oskar Klein Centre, Department of Astronomy, Stockholm University, AlbaNova, SE-106 91 Stockholm, Sweden

¹⁰ Indian Institute of Technology Bombay, Powai, Mumbai 400076, India

¹¹ American University of Sharjah, Physics Department, P.O. Box 26666, Sharjah, UAE

¹² Nordita, KTH Royal Institute of Technology and Stockholm University, Roslagstullsbacken 23, SE-106 91 Stockholm, Sweden

¹³ Sydney Institute for Astronomy, School of Physics, University of Sydney, NSW 2006, Australia

¹⁴ CSIRO Astronomy and Space Science, P.O. Box 76, Epping, NSW 1710, Australia

¹⁵ Australian Research Council Centre of Excellence for Gravitational Wave Discovery (OzGrav), Swinburne University of Technology, Hawthorn, VIC 3122, Australia

¹⁶ Astrophysics Research Institute, Liverpool John Moores University, IC2, Liverpool Science Park, 146 Brownlow Hill, Liverpool L3 5RF, UK

¹⁷ Center for Gravitation, Cosmology and Astrophysics, Department of Physics, University of Wisconsin–Milwaukee, P.O. Box 413, Milwaukee, WI 53201, USA

¹⁸ DIRAC Institute, Department of Astronomy, University of Washington, 3910 15th Avenue NE, Seattle, WA 98195, USA

¹⁹ Indian Institute of Astrophysics, II Block Koramangala, Bengaluru 560034, India

²⁰ Department of Physics and Astronomy, Texas Tech University, Box 1051, Lubbock, TX 79409-1051, USA

²¹ Center of Excellence in Gravitation and Astroparticle Physics, University of Amsterdam, Netherlands

²² Instituto de Astrofísica de Andalucía (IAA-CSIC), Glorieta de la Astronomía s/n, E-18008, Granada, Spain

²³ Caltech Optical Observatories, California Institute of Technology, Pasadena, CA 91125, USA

²⁴ Department of Astronomy, University of California, Berkeley, CA 94720, USA

²⁵ Physics Division, Lawrence Berkeley National Laboratory, 1 Cyclotron Road, MS 50B-4206, Berkeley, CA 94720, USA

²⁶ South African Astronomical Observatory, P.O. Box 9, Observatory 7935, Cape Town, South Africa

²⁷ Astronomical Institute of the Academy of Sciences, Boční II 1401, CZ-14100 Praha 4, Czech Republic

²⁸ Unidad Asociada Departamento de Ingeniería de Sistemas y Automática, E.T.S. de Ingenieros Industriales, Universidad de Málaga, Spain

²⁹ Caltech/IPAC, California Institute of Technology, 1200 East California Boulevard, Pasadena, CA 91125, USA

³⁰ Centre for Astrophysics and Supercomputing, Swinburne University of Technology, Hawthorn, VIC 3122, Australia

³¹ Edna and K.B. Weissman Building of Physical Sciences, Weizmann Institute of Science, Rehovot 76100, Israel

³² Department of Physics and Astronomy, Montclair State University, Montclair, NJ 07043, USA

³³ The eScience Institute, University of Washington, Seattle, WA 98195, USA

³⁴ IPAC, California Institute of Technology, 1200 East California Boulevard, Pasadena, CA 91125, USA

³⁵ Universidad de Granada, Facultad de Ciencias Campus Fuentenueva S/N CP E-18071 Granada, Spain

³⁶ Graduate Institute of Astronomy, National Central University, 32001, Taiwan

³⁷ Institute of Astronomy, National Tsing Hua University, Hsinchu 30013, Taiwan

³⁸ Institute of Physics, Humboldt-Universität zu Berlin, Newtonstr. 15, D-124 89 Berlin, Germany

³⁹ Deutsches Elektronensynchrotron, Platanenallee 6, D-15738, Zeuthen, Germany

⁴⁰ Center for Data Driven Discovery, California Institute of Technology, Pasadena, CA 91125, USA

⁴¹ Center for Interdisciplinary Exploration and Research in Astrophysics (CIERA) and Department of Physics and Astronomy, Northwestern University, 1800 Sherman Road, Evanston, IL 60201, USA

⁴² The Adler Planetarium, Chicago, IL 60605, USA

⁴³ Southern African Large Telescope Foundation, P.O. Box 9, Observatory 7935, Cape Town, South Africa

⁴⁴ Department of Physics and Astronomy and PITT PACC, University of Pittsburgh, PA 15260, USA

- ⁴⁵ School of Physics and Astronomy & Institute for Gravitational Wave Astronomy, University of Birmingham, Birmingham, B15 2TT, UK
⁴⁶ Aryabhata Research Institute of Observational Sciences, Manora Peak, Nainital 263001, India
⁴⁷ INAF, Astrophysics and Space Science Observatory, via P. Gobetti 101, I-40129 Bologna, Italy
⁴⁸ INAF, Istituto di Astrofisica e Planetologia Spaziali, Rome, Italy
⁴⁹ Lawrence Berkeley National Laboratory, 1 Cyclotron Road, Berkeley, CA 94720, USA
⁵⁰ Department of Particle Physics and Astrophysics, Weizmann Institute of Science, Rehovot 76100, Israel
⁵¹ Special Astrophysical Observatory, Russian Academy of Sciences, Nizhnii Arkhyz, 369167, Russia
⁵² School of Astronomy and Space Science, Nanjing University, Nanjing 210093, People's Republic of China
⁵³ Key Laboratory of Modern Astronomy and Astrophysics (Nanjing University), Ministry of Education, People's Republic of China
 Received 2020 June 19; revised 2020 October 19; accepted 2020 October 19; published 2020 December 22

Abstract

We present a systematic search for optical counterparts to 13 gravitational wave (GW) triggers involving at least one neutron star during LIGO/Virgo's third observing run (O3). We searched binary neutron star (BNS) and neutron star black hole (NSBH) merger localizations with the Zwicky Transient Facility (ZTF) and undertook follow-up with the Global Relay of Observatories Watching Transients Happen (GROWTH) collaboration. The GW triggers had a median localization area of 4480 deg^2 , a median distance of 267 Mpc, and false-alarm rates ranging from 1.5 to 10^{-25} yr^{-1} . The ZTF coverage in the g and r bands had a median enclosed probability of 39%, median depth of 20.8 mag, and median time lag between merger and the start of observations of 1.5 hr. The O3 follow-up by the GROWTH team comprised 340 UltraViolet/Optical/InfraRed (UVOIR) photometric points, 64 OIR spectra, and three radio images using 17 different telescopes. We find no promising kilonovae (radioactivity-powered counterparts), and we show how to convert the upper limits to constrain the underlying kilonova luminosity function. Initially, we assume that all GW triggers are bona fide astrophysical events regardless of false-alarm rate and that kilonovae accompanying BNS and NSBH mergers are drawn from a common population; later, we relax these assumptions. Assuming that all kilonovae are at least as luminous as the discovery magnitude of GW170817 (-16.1 mag), we calculate that our joint probability of detecting zero kilonovae is only 4.2%. If we assume that all kilonovae are brighter than -16.6 mag (the extrapolated peak magnitude of GW170817) and fade at a rate of 1 mag day^{-1} (similar to GW170817), the joint probability of zero detections is 7%. If we separate the NSBH and BNS populations based on the online classifications, the joint probability of zero detections, assuming all kilonovae are brighter than -16.6 mag, is 9.7% for NSBH and 7.9% for BNS mergers. Moreover, no more than $<57\%$ ($<89\%$) of putative kilonovae could be brighter than -16.6 mag assuming flat evolution (fading by 1 mag day^{-1}) at the 90% confidence level. If we further take into account the online terrestrial probability for each GW trigger, we find that no more than $<68\%$ of putative kilonovae could be brighter than -16.6 mag. Comparing to model grids, we find that some kilonovae must have $M_{\text{ej}} < 0.03 M_{\odot}$, $X_{\text{lan}} > 10^{-4}$, or $\phi > 30^\circ$ to be consistent with our limits. We look forward to searches in the fourth GW observing run; even 17 neutron star mergers with only 50% coverage to a depth of -16 mag would constrain the maximum fraction of bright kilonovae to $<25\%$.

Unified Astronomy Thesaurus concepts: Neutron stars (1108); Black holes (162); Gravitational waves (678); Nucleosynthesis (1131); R-process (1324); Compact objects (288); Spectroscopy (1558); Sky surveys (1464); Photometry (1234)

1. Introduction

Gravitational-wave (GW) astrophysics is achieving a new frontier every 2 yr. On 2015 September 14, the Advanced LIGO/Virgo Collaboration (LVC) celebrated the revolutionary discovery of GWs from merging massive stellar black holes (BBHs; Abbott et al. 2016). On 2017 August 17, the physics and astronomy communities jointly celebrated the detection of GWs from the first binary neutron star (BNS) merger that lit up the entire electromagnetic (EM) spectrum (Abbott et al. 2017a, 2017b; Coulter et al. 2017; Evans et al. 2017; Goldstein et al. 2017; Haggard et al. 2017; Hallinan et al. 2017; Margutti et al. 2017; Troja et al. 2017; Kasliwal et al. 2019b). On 2019 April 26, the first candidate neutron star black hole (NSBH) merger was announced by Advanced LIGO/Virgo (Ligo Scientific Collaboration & VIRGO Collaboration 2019a, 2019b), and since then, there have been eight additional candidate NSBH events.

Unlike a BNS system, the very existence of an NSBH binary was observationally unconstrained. No pulsar in the Milky

Way is known to have a black hole companion. A compact BNS merger has a viable stellar evolutionary formation channel (Tauris et al. 2015), since a few ultrastripped supernovae (SNe) have been seen (De et al. 2018; Nakaoka et al. 2020; Yao et al. 2020). On the other hand, it has been argued that the supermassive black holes in the nuclei of galaxies assist in the formation of compact NSBH (and BBH) systems by the eccentric Kozai–Lidov (EKL) mechanism (Naoz 2016; Stephan et al. 2019). Unlike a BNS merger, for which GW170817 serves as the Rosetta Stone of what to look for, theoretical predictions of the EM counterparts to NSBH mergers span a wide spectrum, depending on the system parameters (e.g., mass ratio, spin of the black hole, equation of state of the neutron star). While some scenarios predict that the neutron star is swallowed whole by the black hole and there is no EM emission, others predict a luminous kilonova where, compared to the BNS case, more lanthanide-rich material is ejected dynamically while comparable masses are ejected from the disk (e.g., Rosswog 2005; Foucart 2012; Hotokezaka et al. 2013; Kiuchi et al. 2015; Kawaguchi et al. 2016; Kasen et al. 2017; Kruckow et al. 2018; Broekgaarden et al. 2019; Nakar 2020; Fernández et al. 2020).

⁵⁴ Hubble Fellow.

⁵⁵ Moore-Sloan, WRF, and DIRAC Fellow.

⁵⁶ LSSTC Data Science Fellow.

LIGO/Virgo’s third observing run (O3; from 2019 April to 2020 March) has yielded real-time alerts on six BNS mergers and nine NSBH mergers. Alerts and localization maps were publicly released within minutes to a few hours after the mergers. Updates to localization maps and false-alarm rates (FARs) were released days to weeks after the mergers. The median localization was 4480 deg^2 . The median distance to BNS mergers was 214 Mpc, and that to NSBH mergers was 377 Mpc.

Given that the optical counterpart of GW170817 was first observed only 10.8 hr after merger, there is considerable debate on how the early emission evolves. Different models predict different early evolution (e.g., Drout et al. 2017; Kasliwal et al. 2017; Arcavi 2018; Piro & Kollmeier 2018; Waxman et al. 2018). Thanks to the low latency in the public O3 alerts, prompt follow-up was undertaken. Despite the localizations being coarser and the distances being further than expected (Abbott et al. 2018), the Global Relay of Observatories Watching Transients Happen (GROWTH⁵⁷) collaboration undertook systematic searches and extensive follow-up of every trigger with a worldwide network of telescopes. We used three discovery engines, the Zwicky Transient Facility (ZTF; Bellm et al. 2018; Masci et al. 2018; Graham et al. 2019), Palomar Gattini-IR (PGIR; Moore & Kasliwal 2019; De et al. 2020a), and Dark Energy Camera (DECam; Goldstein et al. 2019), and a suite of 17 follow-up facilities. Candidate counterparts and follow-up results from these searches were promptly announced via Gamma-ray Coordinates Network (GCN) circulars. In addition to GROWTH, several teams undertook wide-field searches for optical counterparts in O3, including Electromagnetic counterparts of Gravitational wave sources at the Very Large Telescope (ENGRAGE; Levan 2020), Global Rapid Advanced Network Devoted to the Multi-messenger Addicts (GRANDMA; Antier et al. 2020), Gravitational-wave Optical Transient Observer (GOTO; Gompertz et al. 2020), All Sky Automated Survey for SuperNovae (ASAS-SN; Shappee et al. 2014), Asteroid Terrestrial Last Alert System (ATLAS; Tonry et al. 2018), Panoramic Survey Telescope and Rapid Response System (PanSTARRS; Chambers et al. 2016), MASTER-Net (Lipunov et al. 2017), Searches after Gravitational Waves Using ARizona Observatories (SAGUARO; Lundquist et al. 2019), Dark Energy Survey Gravitational Wave Collaboration (DES-GW; Soares-Santos et al. 2017), Burst Optical Observer and Transient Exploring System (BOOTES), KM3Net,⁵⁸ and VINROUGE⁵⁹ (PI: Tanvir). We also undertook a wide-field radio search with the Australian Square Kilometre Array Pathfinder (ASKAP; Dobie et al. 2019).

This paper focuses on events that contain at least one neutron star; see Graham et al. (2020) for our candidate counterpart to a binary black hole merger. The LVC published GW190425 as a confirmed astrophysical BNS with a total system mass of $3.4 M_{\odot}$ (Abbott et al. 2020a). The LVC also published GW190814 as a confirmed astrophysical merger of a $23 M_{\odot}$ black hole with a $2.6 M_{\odot}$ compact object (Abbott et al. 2020b). While we await the final LVC results on the candidature and binary parameters of all other merger candidates from O3, we use the classifications and parameters released via GCN circulars. We refer to GW190814 and GW190425 as “sources” or “confirmed events” and use a

“GW” prefix in the name. We refer to all others as “triggers” or “candidate events” with an “S” prefix in the name. We refer to the full set as “events.”

We have previously published our search results for the highest-significance mergers: GW190425 (Coughlin et al. 2019d), GW190814 (Dobie et al. 2019; Andreoni et al. 2020b), and S2001015ae and S200115j (Anand et al. 2020). Here we focus on ZTF searches of the full set of O3 triggers and the implications of the joint nondetection of kilonovae from all merger candidates. In Section 2, we summarize the GW trigger selection criteria. In Section 3, we detail the discovery, follow-up, and rejection of candidate optical counterparts. In Section 4, we examine the model-independent implications of the luminosity function of kilonovae. In Section 5, we summarize our key results and look ahead to future GW observing runs.

2. Summary of GW Triggers

During the third LIGO/Virgo observing run, we triggered target-of-opportunity (ToO) searches based on the following criteria: (a) an initial classification with the highest probability of either BNS, NSBH, or MassGap; (b) if MassGap, then a nonzero probability of containing a neutron star; and (c) a visibility and mapping speed allowing us to observe $>30\%$ of the initial BAYESTAR sky map (Singer & Price 2016) within 24 hr of merger.

A total of 15 GW events satisfied criteria (a) and (b). In Table 1, we summarize 13 GW triggers during O3 for which we obtained either serendipitous or triggered coverage with the ZTF (we did not get any ZTF data on S190510g, as the sky position was too far south, or S190924h, as the sky position was too close to the Moon). In Figures 1–3, we show the ZTF coverage overlaid on the GW localization contours. Since the public ZTF survey systematically covers the accessible northern sky at an average cadence of 3 days to a median depth of 20.5 mag (Bellm et al. 2018), we “serendipitously” covered several GW sky maps. Serendipitous coverage contributed to more than 30% enclosed probability for the following triggers: GW190814, S190910d, S190910h, S190923y, S190930t, S200105ae, and S200213t. To improve depth/coverage/response time, we triggered ZTF ToO observations for 11 out of 15 events (and undertook DECam searches for three events; see Andreoni et al. 2019c, 2020b; Goldstein et al. 2019). Our triggered ToO observations optimized the trade-off between depth (more exposure time per pointing) and coverage of the localization map (more pointings to enclose more probability) using the `gwemopt` algorithm. A detailed case study of the ToO observations can be found in Coughlin et al. (2019d) and Anand et al. (2020). For S191205ah, our triggered observations were not completed due to bad weather, and only a small fraction was covered serendipitously. For S190910h, given the coarse localization, we relied only on serendipitous coverage as part of regular ZTF operations. For S190923y, given the large time lag between GW alert and first target visibility, we also relied only on serendipitous coverage.

The location of Palomar Observatory relative to LIGO’s quadrupolar antenna sensitivity pattern helps minimize the time lag to respond to triggers in real time (see Figure 4); the latency to first observation was between 11 s and 13.7 hr. (The lowest latency of 11 s was enabled by serendipitous coverage.) As predicted by simulations (Nissanke et al. 2013; Kasliwal & Nissanke 2014), all (but one) GW public alerts were accessible from Palomar Observatory, and more than half could be

⁵⁷ <http://growth.caltech.edu/>

⁵⁸ <https://www.km3net.org/>

⁵⁹ <https://www.star.le.ac.uk/nrt3/VINROUGE/>

Table 1
Summary of ZTF Follow-up of 13 GW Triggers in O3

Name	FAR (P_t)	Localization	Distance	Class	P_1	P_2	Time Lag	Depth	$E(B - V)$
GW190425	1 per 69,000 yr (1%)	7461 deg ²	156 ± 41 Mpc	BNS	24.13% (45.92%)	23.90% (44.62%)	0.003 hr	21.5	0.03
S190426c	1 per 1.6 yr (58%)	1131 deg ²	377 ± 100 Mpc	NSBH	52.33% (59.69%)	51.57% (57.40%)	13.06 hr	21.5	0.34
GW190814	1 per 10 ²⁵ yr (1%)	23 deg ²	267 ± 52 Mpc	NSBH	88.57% (87.00%)	78.37% (70.60%)	0.00 hr	21.0	0.02
S190901ap	1 per 4.5 yr (14%)	14,753 deg ²	241 ± 79 Mpc	BNS	56.94% (50.67%)	49.39% (42.76%)	3.61 hr	21.0	0.03
S190910d	1 per 8.5 yr (2%)	2482 deg ²	632 ± 186 Mpc	NSBH	32.99%(42.50%)	31.17% (39.64%)	1.51 hr	20.3	0.04
S190910h	1 per 0.9 yr (39%)	24,264 deg ²	230 ± 88 Mpc	BNS	33.26% (42.95%)	28.92% (38.44%)	0.015 hr	20.4	0.08
S190923y	1 per 0.67 yr (32%)	2107 deg ²	438 ± 133 Mpc	NSBH	NA (38.99%)	NA (19.22%)	13.73 hr	20.1	0.09
S190930t	1 per 2.0 yr (26%)	24,220 deg ²	108 ± 38 Mpc	NSBH	NA (50.63%)	NA (43.42%)	11.91 hr	21.1	0.05
S191205ah	1 per 2.5 yr (7%)	6378 deg ²	385 ± 164 Mpc	NSBH	NA (5.68%)	NA (4.85%)	10.66 hr	17.9	0.04
S191213g	1 per 0.89 yr (23%)	4480 deg ²	201 ± 81 Mpc	BNS	27.50% (0.80%)	25.10% (0.09%)	0.013 hr	20.4	0.30
S200105ae	NA (97%)	7373 deg ²	283 ± 74 Mpc	NSBH	52.39% (56.40%)	43.99% (47.96%)	9.96 hr	20.2	0.05
S200115j	1 per 1513 yr (1%)	765 deg ²	340 ± 79 Mpc	NSBH	22.21% (34.92%)	15.76% (18.17%)	0.24 hr	20.8	0.13
S200213t	1 per 1.8 yr (37%)	2326 deg ²	201 ± 80 Mpc	BNS	72.17% (79.29%)	70.48% (76.08%)	0.40 hr	21.2	0.19

Note. We list the GW FAR and, in parantheses, the probability that the event is terrestrial (P_t). We list the total size of the GW localization region, the GW median distance, and the most probable GW classification. We report the integrated probability within the 90% contour of the LALInference sky map, covered by triggered and serendipitous ZTF searches during the first 3 days after merger observed at least once (P_1) and probability observed at least twice (P_2). In parentheses, we include the coverage based on the BAYESTAR sky map. For some alerts, only BAYESTAR sky maps were made available. All estimates correct for chip gaps and processing failures. We also report the time lag between merger time and the start of ZTF observations (hours), the median depth (AB mag), and the median line-of-sight extinction.

followed up within 4 hr of the merger. Throughout the paper, we only use enclosed probability based on the LALInference sky map, as it is deemed more accurate (Veitch et al. 2015), when available. The LALInference sky maps were mostly released only after our observations were completed. Hence, the enclosed probability estimates were systematically lower than those estimated by the observation plan based on the initial BAYESTAR sky maps (see Table 1).

The process for triggering ToO observations for a survey system like the ZTF differs from traditional telescopes, as it involves halting the ongoing survey observations and scheduling observations of only certain fields as selected by an observation plan. Observation plans are generated by `gwemopt`,⁶⁰ a code base for optimizing galaxy-targeted and synoptic searches within GW sky maps (Coughlin et al. 2018, 2019a). Over the course of O3, we implemented several improvements to the existing code framework, including additional features that allow us to strategically handle sky maps spanning thousands of square degrees, slice sky maps by R.A. and schedule slices separately, and balance coverage in multiple filters. These improvements, among others, are described in Almualla et al. (2020). All of our triggered follow-up of GW events, gamma-ray bursts (GRBs; T. Ahumada et al. 2020, in preparation), and high-energy neutrino events (Stein et al. 2020) occurs through a user interface called the GROWTH ToO Marshal,⁶¹ a database designed to ingest GCN circulars, display event properties and sky maps, design plans, trigger observations, query for candidates within the observed region, and retrieve summary statistics for completed observations, including probability covered and median depth (Coughlin et al. 2019a; Kasliwal et al. 2019a).

3. Investigating Candidate Counterparts

Our candidate vetting methodology has continued to improve over the past few years, starting with Fermi afterglow searches

(Singer et al. 2015), to BBH searches in O1 (Kasliwal et al. 2016), to BNS and NSBH searches in O3 (Coughlin et al. 2019a; Anand et al. 2020). We graphically summarize the candidate vetting process in Figure 5. Here we first discuss the prompt vetting procedure that quickly led to a GCN circular announcing candidate counterparts (Section 3.1). Next, we discuss follow-up of the candidates to discern their nature (Section 3.2). Finally, we discuss a deeper offline search to look for any missed candidates (Section 3.3).

3.1. Initial Transient Vetting

For each of the 13 GW triggers followed up by ZTF, we systematically identified transient candidates within the localization region and ruled them out using various metrics. Below, we summarize the transient filtering process and results from our candidate vetting.

The GROWTH team has three independent database systems to retrieve interesting objects in real time: the GROWTH Marshal (Kasliwal et al. 2019a), the Kowalski⁶² system (Duvet et al. 2019), and the Alert Management, Photometry and Evaluation of Lightcurves (AMPEL) system (Soumagnac & Ofek 2018; Nordin et al. 2019). Each platform retrieves a stream of AVRO packet alerts (Patterson et al. 2019) containing significant object detections identified by the ZTF image subtraction pipeline, defined as a $>5\sigma$ change in brightness relative to a reference image (Masci et al. 2018). Each of these objects undergoes a series of filtering steps in order to identify candidates that could be interesting to pursue for follow-up. The following criteria were common for all three queries.

1. Positive subtraction. The object must have brightened relative to the reference image.
2. Astrophysical. The object must have a real bogus (rb) score >0.25 or a deep learning (drb) score >0.8 (Duvet et al. 2019; Mahabal et al. 2019) for it to be considered astrophysical.

⁶⁰ <https://github.com/mcoughlin/gwemopt>

⁶¹ <https://github.com/growth-astro/growth-too-marshall>

⁶² <https://github.com/dmitryduvet/kowalski>

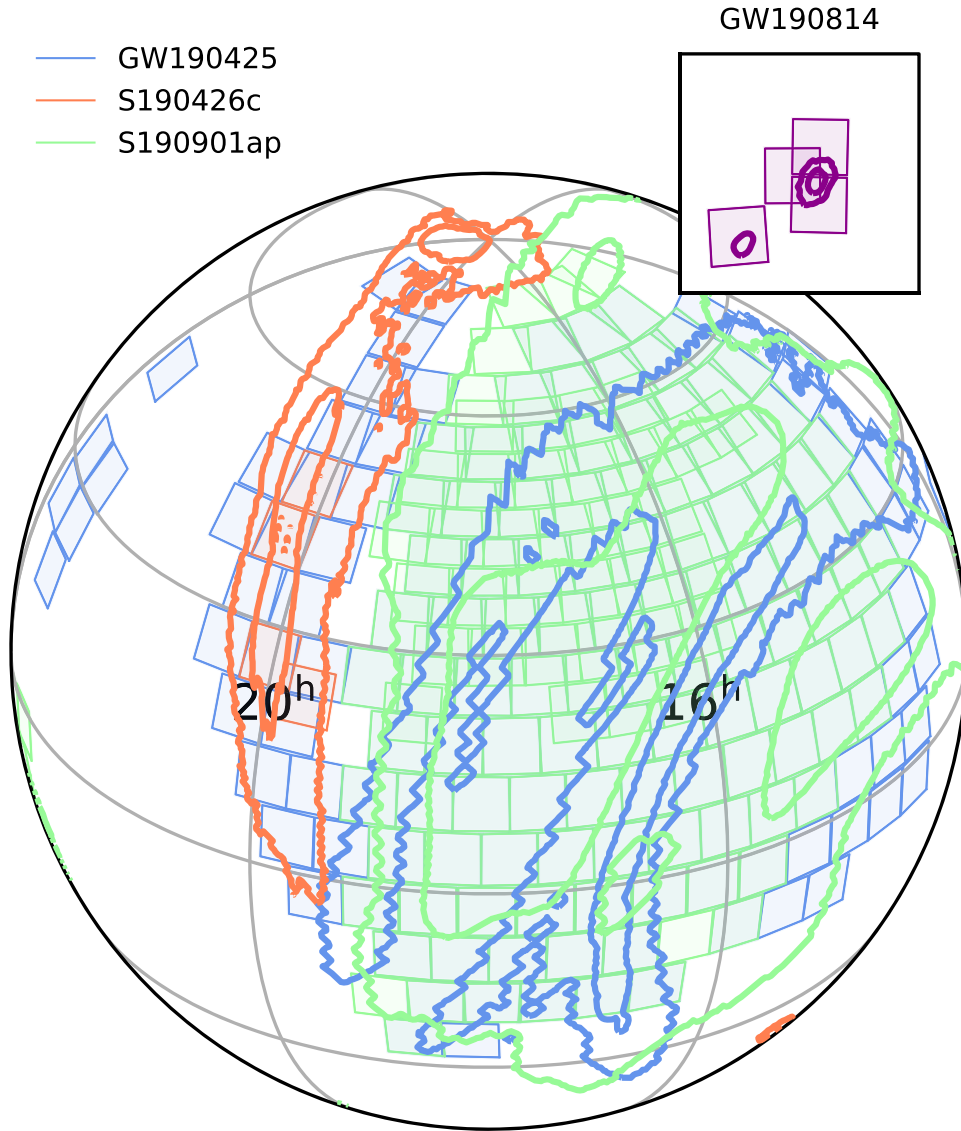


Figure 1. The ZTF coverage maps of two BNS triggers (S190901ap and GW190425) and two NSBH triggers (S190426c and GW190814) during O3 of LIGO/Virgo. Each square represents a ZTF pointing, and the solid line denotes the latest available GW 90% localization contour. Despite both BNS triggers being localized to a π of the sky, the ZTF was able to map the accessible localization area in a few hours.

3. Not stellar. The object must be $>2''$ away from a cataloged point source in the PanSTARRS Point Source Catalog (Tachibana & Miller 2018).
4. Far from a bright source. The object must be at least $20''$ away from a bright ($m_{AB} < 15$ mag) star to avoid blooming artifacts.
5. Not moving. The object must have at least two detections separated by at least 15 minutes to reject asteroids (moves $<4'' \text{ hr}^{-1}$).
6. No previous history. The object must not have any historical detections in the ZTF alert stream prior to the GW merger time.

While the GROWTH Marshal queried all fields triggered as part of the ToO search, the Kowalski and AMPEL queries searched for candidates in both serendipitous and triggered data within the 95% contour of the latest sky map that was available. The AMPEL query⁶³ had further image quality cuts performed

to reject poor subtractions based on morphology, an additional cut based on proximity to known solar system objects, and another cut based on cross-matching to the Gaia Data Release 2 (DR2) catalog and PS1 to identify likely stellar sources.

All candidates that passed the filtering criteria were saved to the GROWTH Marshal for further vetting in real time by a dedicated team of scanners. If a transient was consistent with the nucleus of a galaxy and the mid-infrared colors (based on the Wide-field Infrared Survey Explorer (WISE) catalog; Wright et al. 2010) of the host galaxy were consistent with active galactic nuclei (AGNs), the candidate was deemed unrelated.

All viable candidates were promptly announced to the worldwide community via GCN circulars, and many teams (not only GROWTH) triggered follow-up observations for many of our candidates.⁶⁴ Using the GROWTH Marshal system, we prioritized and triggered follow-up of candidates that exhibited

⁶³ https://github.com/robertdstein/ampel_followup_pipeline

⁶⁴ The GROWTH collaboration posted 82 GCNs during O3. An additional 151 GCNs refer to follow-up of ZTF objects by other teams.

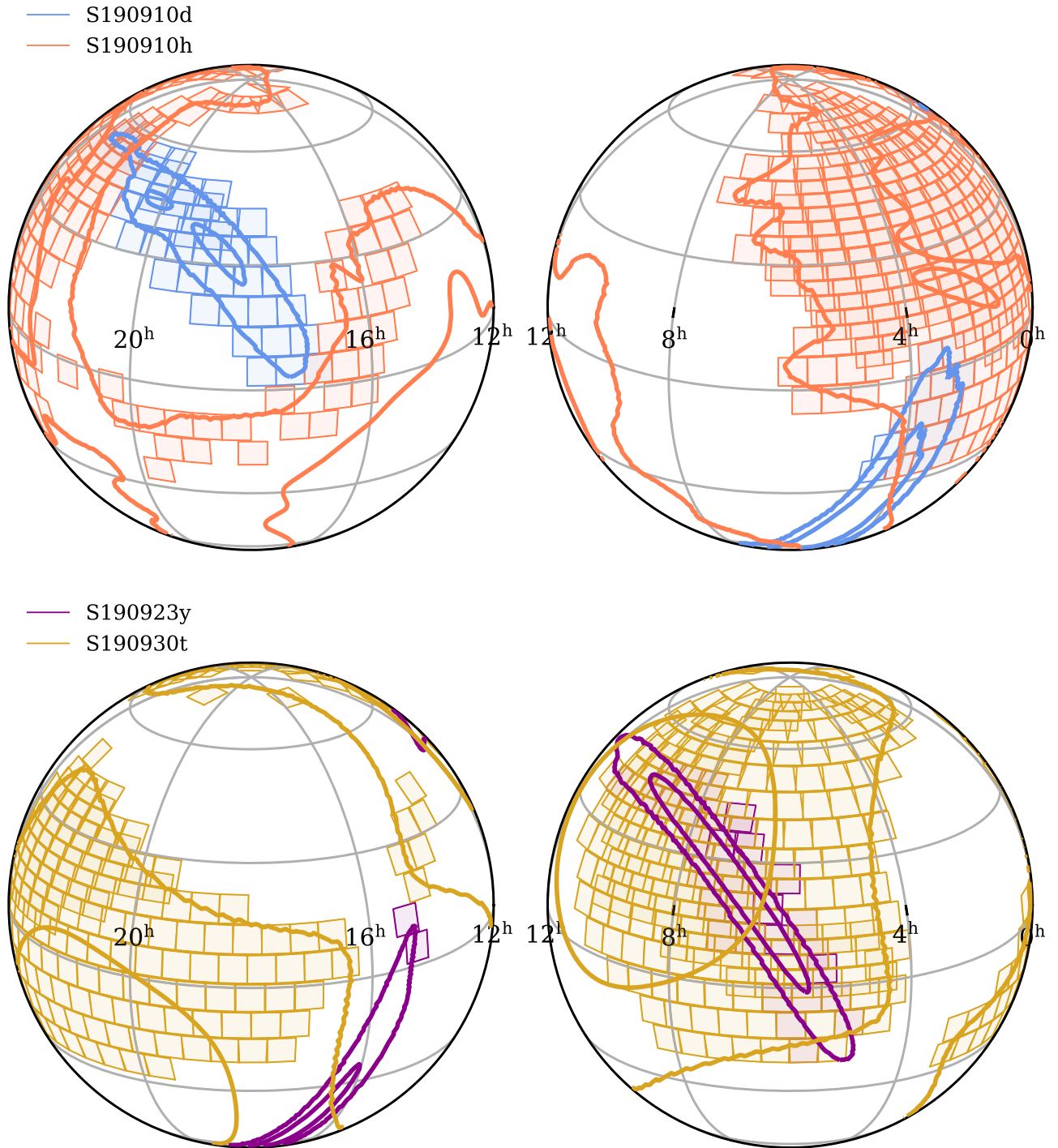


Figure 2. Top: ZTF coverage maps of the two same-day triggers occurring on September 10 (S190910d and S190910h) during O3 of LIGO/Virgo. Given the spatial and temporal overlap of these two GW triggers, some field observations contributed to coverage of both. Bottom: ZTF coverage maps of two NSBH triggers (S190923y and S190930t) during O3. Each square represents a ZTF pointing, and the solid line denotes the latest available GW 90% localization contour.

rapid photometric evolution (faster than 0.3 mag day^{-1}), showed red colors, or were close to a host galaxy with a redshift consistent with the GW distance constraint.

3.2. Examining Promising Candidate Counterparts with Additional Follow-up

We now briefly describe how we ruled out the association between vetted counterpart candidates and the GW event. A detailed account of every candidate announced via GCN is in Appendix B.

The GROWTH team obtained follow-up with the following facilities to characterize the photometric and/or spectroscopic evolution: the Liverpool Telescope (LT; Steele et al. 2004), Lowell Discovery Telescope (LDT,⁶⁵ formerly known as the Discovery Channel Telescope), Las Cumbres Observatory (LCO; Brown et al. 2013), Apache Point Observatory (APO; Huehnerhoff et al. 2016), Kitt Peak EMCCD Demonstrator (KPED; Coughlin et al. 2019b), Lulin One-meter Telescope

⁶⁵ <https://lowell.edu/research/research-facilities/4-3-meter-ldt/>

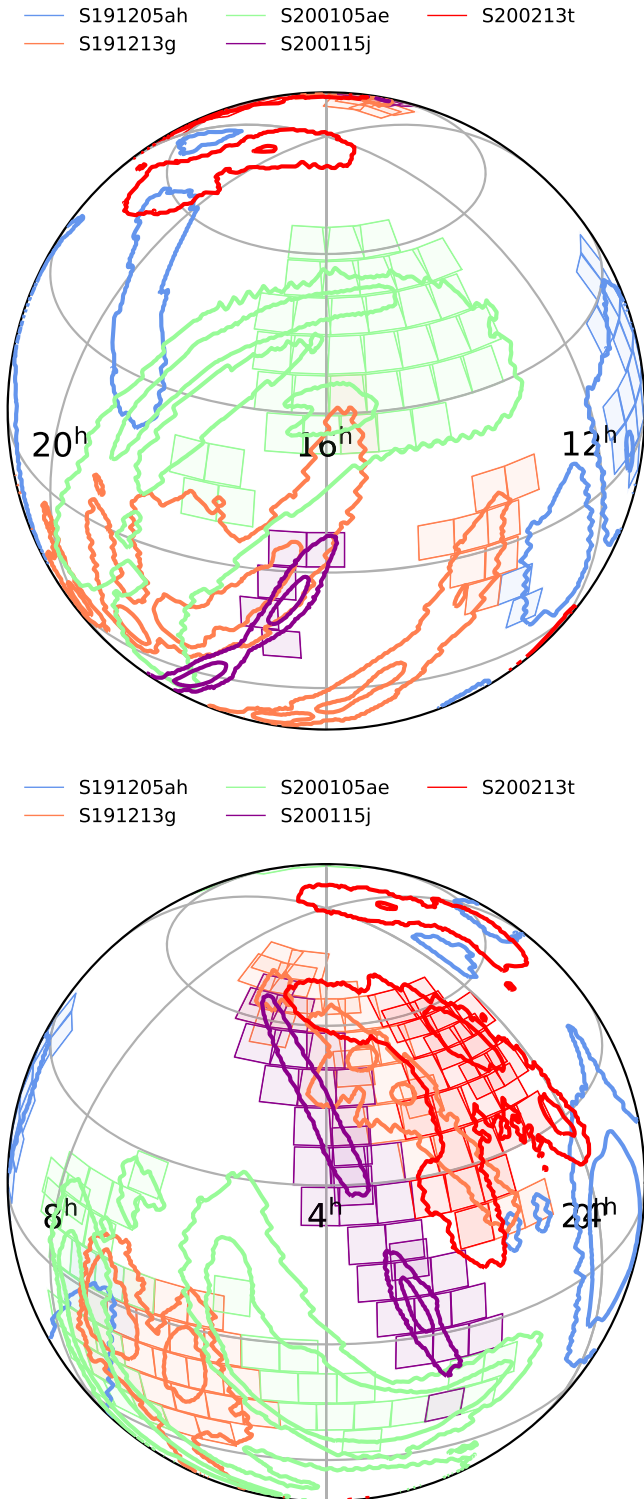


Figure 3. The ZTF coverage maps of the triggers during the second half of O3 of LIGO/Virgo: S191205ah, S191213g, S200105ae, S200115j, and S200213t. The top and bottom panels show opposite sides of the globe. Each square represents a ZTF pointing, and the solid line denotes the latest available GW 90% localization contour.

(LOT; Huang et al. 2005), GROWTH-India telescope (GIT;⁶⁶ V. Bhalerao et al. 2020, in preparation), Palomar 60 inch

⁶⁶ <https://sites.google.com/view/growthindia/>

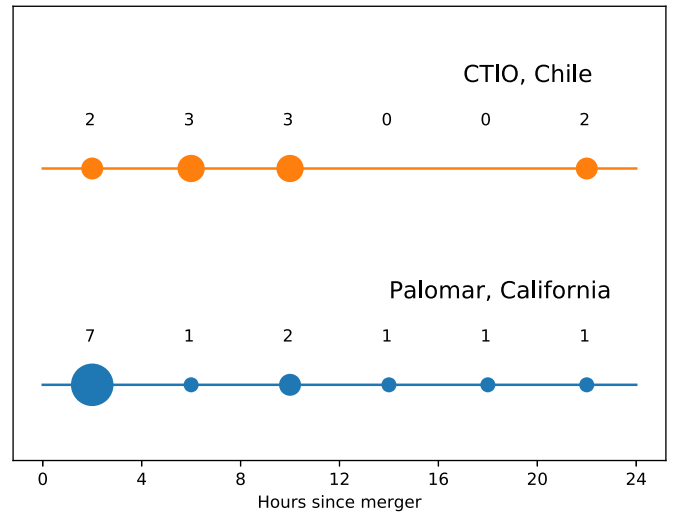


Figure 4. Distribution of response time, defined as the time lag between merger time and earliest possible observation time at a given site, for all 15 BNS/NSBH triggers in O3. We define that observations can begin when at least 30% of the enclosed probability of a GW localization contour is above airmass 2.0 and the Sun is 12° below the horizon at a given site. The size of the filled circles scales with the number of triggers in each time bin. Note that the location of Palomar Observatory enables a response to more triggers than CTIO overall (13 vs. 10 triggers) and a larger number (seven vs. two triggers) within 4 hr after merger.

telescope (P60; Cenko et al. 2006), Palomar 200 inch Hale Telescope⁶⁷ (P200), Keck Observatory,⁶⁸ Gemini Observatory,⁶⁹ Southern African Large Telescope⁷⁰ (SALT), Himalayan Chandra Telescope⁷¹ (HCT), and Gran Telescopio Canarias⁷² (GTC). Figures 6 and 7 illustrate examples of follow-up by the GROWTH team on some ZTF candidates. The specific instrument configurations and data reduction methods are described in Appendix A.

The follow-up observations include both photometric and spectroscopic data. Moreover, the association of a candidate with a GW trigger was rejected if its properties fell into one or more of the categories described as follows.

1. Inconsistent spectroscopic classification. We ruled out candidates that could be spectroscopically classified as SNe, AGNs, cataclysmic variables (CVs), and other flare stars. We used SNID (Blondin & Tonry 2007) and dash (Muthukrishna et al. 2019) to classify the SNe and AGNs found in our searches. The CVs and variable stars often showed hydrogen features at zero redshift.
2. Inconsistent distance. We ruled out candidates whose spectroscopic redshift was not consistent with the GW distance within 2σ . We cross-matched the transient positions with the Census of the Local Universe (CLU; Cook et al. 2019) galaxy catalog and the NASA Extragalactic Database (NED) to look up host redshifts where available. We also cross-matched the candidates against the Photometric Redshifts Legacy Survey (PRLS; Zhou et al. 2020) catalog and reported the photometric redshifts when the spectroscopic redshift was unavailable.

⁶⁷ <https://www.astro.caltech.edu/palomar/about/telescopes/hale.html>

⁶⁸ <http://www.keckobservatory.org/>

⁶⁹ <http://www.gemini.edu/>

⁷⁰ <https://www.salt.ac.za/>

⁷¹ https://www.iiap.res.in/?q=telescope_iao

⁷² <http://www.gtc.iac.es/gtc/gtc.php>

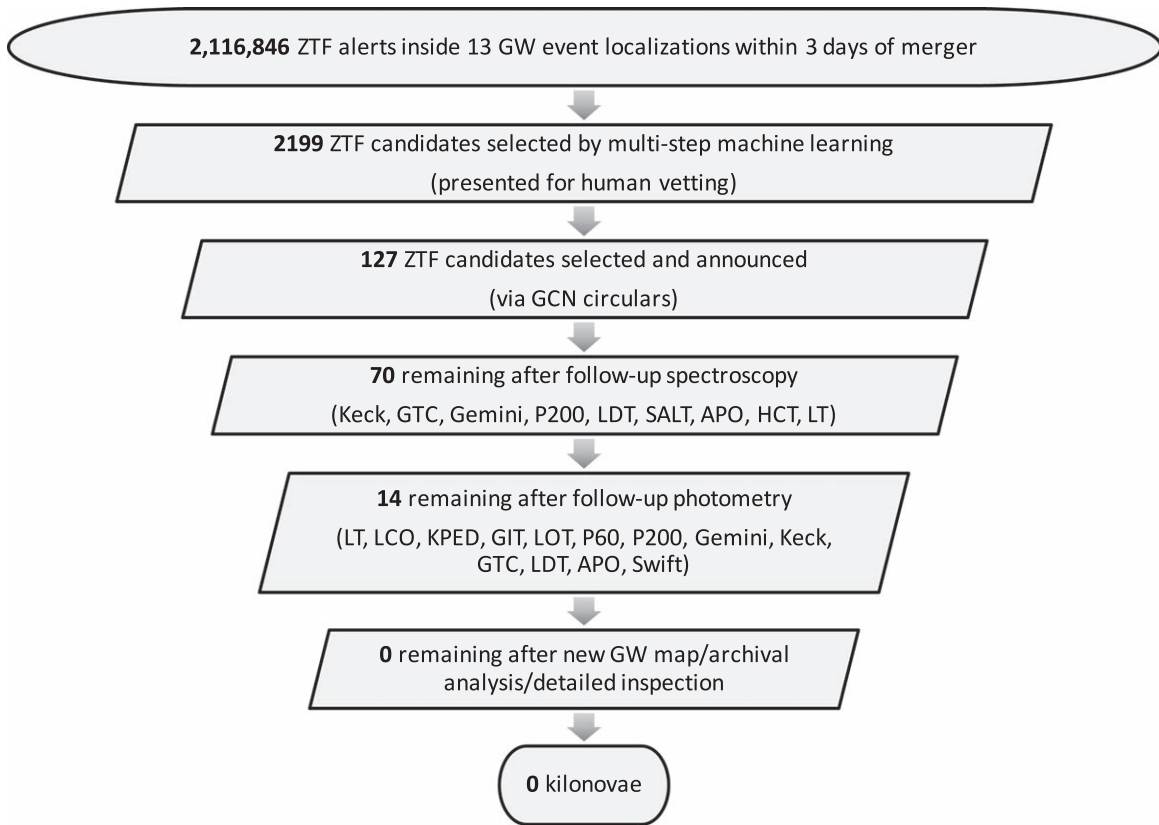


Figure 5. Flowchart to show how our candidate vetting funneled from a large number of spatially and temporally consistent alerts, to a smaller number of candidates that deem human vetting, to an even smaller number of candidates that warrant detailed follow-up characterization over the course of O3.

3. Slow photometric evolution. As kilonovae are expected to evolve faster than SNe, we ruled out candidates that evolved slower than 0.3 mag day^{-1} . We used `ForcePhot`⁷³ (Yao et al. 2019), a forced photometry package, to examine the transient light curves. To quantify the evolution of a given transient, we define the parameter $\alpha_f = \Delta m / \Delta t$ [mag day^{-1}], where f corresponds to the filter used to determine the variation in magnitude (Δm) over time (Δt). A positive α indicates a fading source, while a negative α describes a rising source. The baseline (Δt) is defined to be the number of days it takes an object to rise from its discovery to its peak magnitude ($\alpha < 0$) or the number of days it takes the transient to fade from peak to undetectable by ZTF ($\alpha > 0$). We used a minimum time baseline of 3 days to compute slopes.
4. Outside of the latest LALInference map. The majority of the candidates were selected and announced via GCN based on the promptly available BAYESTAR map (Singer & Price 2016). When the LALInference map was made available, if a candidate was outside the 90% probability contour, we rejected it.
5. Artifacts. Most of the ZTF ghosts and artifacts are well known (Bellm et al. 2018; Masci et al. 2018)⁷⁴ and masked automatically. Additionally, we take further precautions by ignoring transients close to bright stars in our initial vetting. However, for example, our extensive analysis revealed a subtle gain mismatch in the reference images that posed as a faint and fast

transient (see discussion related to ZTF19aassfws in Appendix B). All references for ToOs were rebuilt after this artifact was identified.

6. Asteroids. Sometimes slow-moving asteroids, especially near stationary points, can mimic a fast-fading transient (Jedicke et al. 2016). For these objects, either a more careful inspection of the centroids or movement in follow-up imaging served as the reason for rejection.
7. Previous activity. Candidates were rejected if they showed previous detections prior to the GW merger time in other surveys, e.g., the Catalina Real Time Survey (CRTS; Djorgovski et al. 2011), Palomar Transient Factory (PTF; Law et al. 2009), intermediate Palomar Transient Factory (iPTF; Cao et al. 2016; Masci et al. 2017), and PS1 (Tachibana & Miller 2018).

Some candidates prompted panchromatic follow-up. We followed up five candidates in the ultraviolet and X-ray with the Neil Gehrels Swift Observatory (see the Appendix for details). We followed up two candidates in the radio with the Arcminute Microkelvin Imager (AMI) and one with the Karl G. Jansky Very Large Array (VLA; see the Appendix for details). All candidates, grouped by GW trigger, are listed in Tables 2–10, along with their respective rejection criteria.

3.3. Candidates from Deeper Offline Searches

We complemented our real-time analysis described above with a deeper offline search by relaxing the selection criteria (e.g., requiring only one detection instead of two). The following steps describe our offline search.

⁷³ <https://github.com/yaoyuhan/ForcePhotZTF>

⁷⁴ <http://nessi.cacr.caltech.edu/ZTF/Web/Ghosts.html>

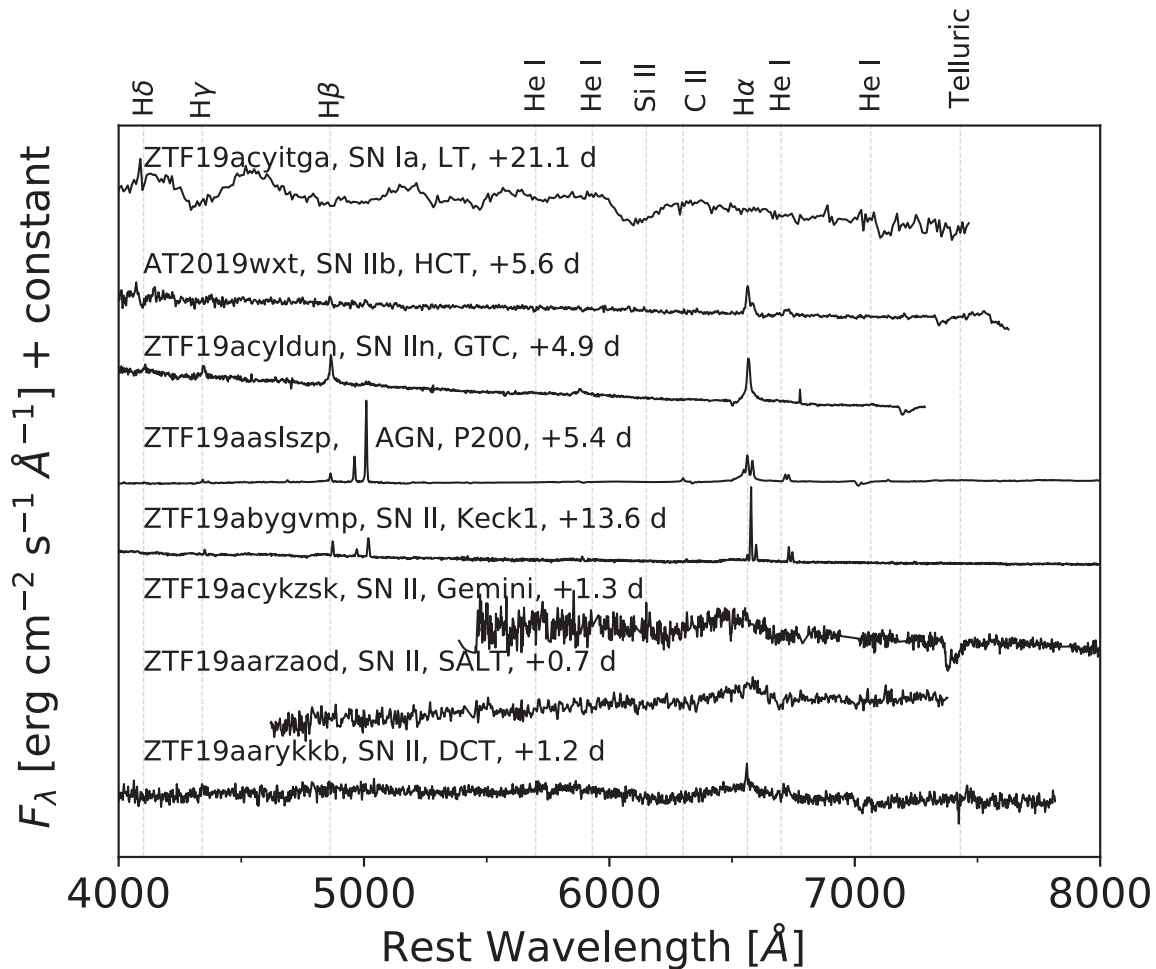


Figure 6. Collage of spectra taken during our GW follow-up in O3, one from each spectroscopic facility. The spectra displayed include six Type II SNe, one AGN, and one Type Ia SN and were taken with LT+SPRAT and GTC+OSIRIS in Roque de los Muchachos, Spain; P200+DBSP on Palomar Mountain, USA; Keck1+LRIS and Gemini+GMOS-N on Maunakea, USA; SALT+RSS in Sutherland, South Africa; HCT+HFOSC in Hanle, India; and LDT+Deveny in Happy Jack, USA.

1. We used *Kowalski* to query the ZTF database looking for any source (i) located within 95% of the most updated sky map, (ii) never detected before the merger time, (iii) with at least one detection within 72 hr of merger, (iv) with the last detection occurring within 10 days of the first detection, and (v) passing real/bogus thresholds of $rb > 0.5$ and $drb > 0.8$ (or $brai > 0.8$; Duev et al. 2019). Further details on the selection criteria will be described in I. Andreoni et al. (2020, in preparation).
2. Forced point-spread function (PSF) photometry was performed at the location of each transient candidate using *ForcePhot*, setting a detection threshold of signal-to-noise ratio (S/N) > 3 , where the images were available.
3. The flux measured using forced photometry was stacked nightly in each band, allowing us to become sensitive to fainter sources when multiple images were available on the same night.
4. The rising and fading rates were computed in each band with a linear fit before and after the brightest data point of each light curve. A time baseline of > 3 hr was required for the fit to be performed.
5. Candidates were selected with a fading rate more rapid than 0.3 mag day^{-1} or rising rate faster than 1 mag day^{-1} .

We rejected candidates still detected after 6, 12, and 14 days after the merger time in the g , r , and i bands, respectively. More details are given in I. Andreoni et al. (2020, in preparation).

The *Kowalski* query initially returned 8026 sources for the 13 GW triggers. Applying all of the selection criteria described above, 453 candidates survived the automatic cuts. Of these, 21 had at least two ZTF alerts, and 432 had only one ZTF alert (additional detections were recovered by forced photometry and stacking).

Of the 21 sources with at least two detections in the ZTF alert stream, only five candidates passed visual inspection of the images and light curves: ZTF19acbxacj was an AGN candidate (Assef et al. 2018; Bailer-Jones et al. 2019); ZTF19abwsfsl was a cataloged CV (Gaia Collaboration 2018); ZTF19acbqtue was followed up with the Gemini Multi-Object Spectrograph (GMOS-N), and a quiescent source was found at $g = 24.69 \pm 0.07 \text{ mag}$ with a color $g - i = 1.89 \text{ mag}$, consistent with an M dwarf (West et al. 2011); ZTF19abyndjf was a fast-evolving transient without an obvious host galaxy; and ZTF19acbwmt was hostless and had a previous detection in the PS1-DR2 catalog from 2012 (see Figure 8). For the last two candidates, upper limits between the GW merger time and the

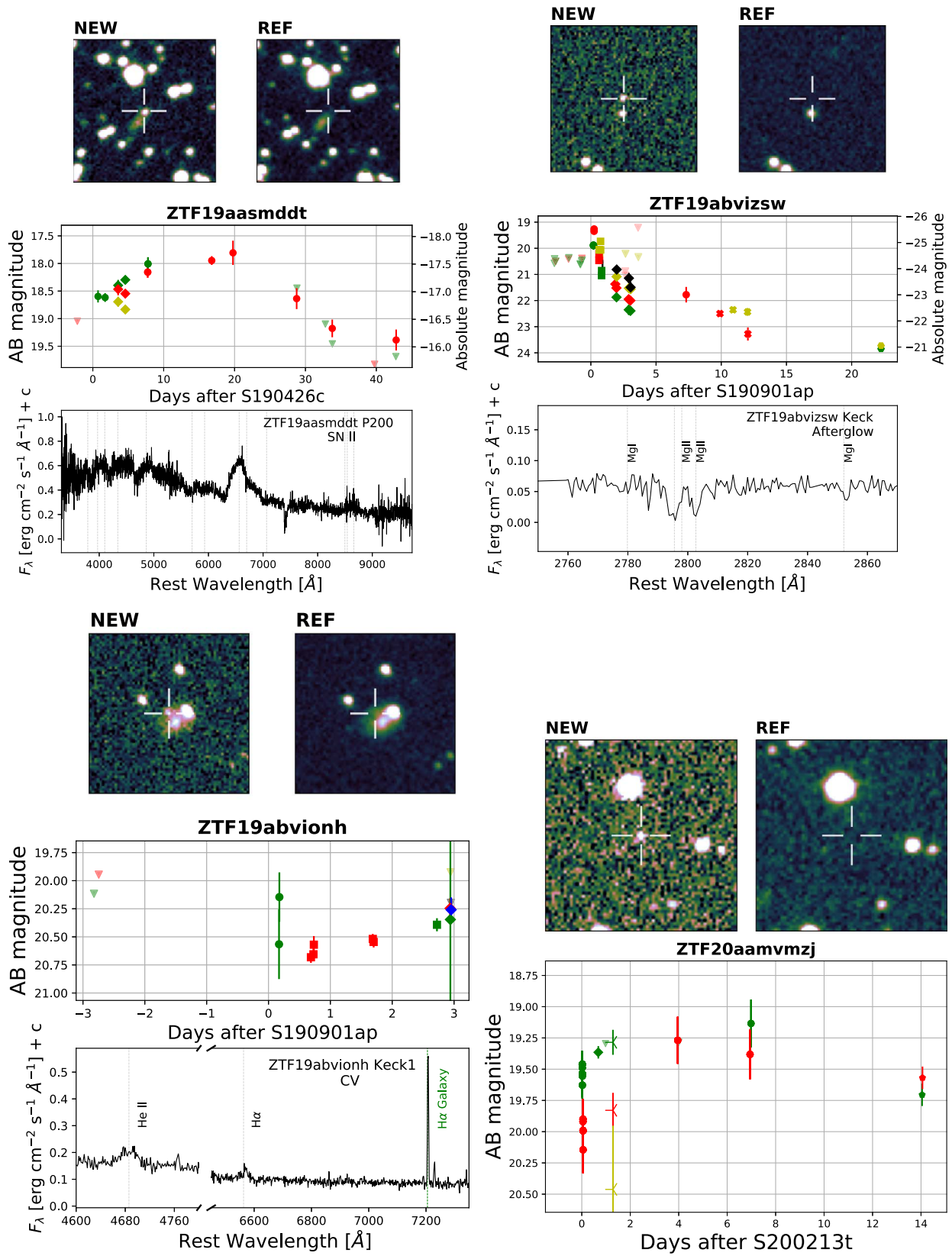


Figure 7. Collage of candidate counterparts found during real-time searches. We show a $7'' \times 7''$ region with north up and east left for the discovery (NEW) and reference (REF) images. We also show the light curve of the candidate, where the u -, g -, r -, i -, and z -band data are shown in blue, green, red, yellow, and black respectively. The ZTF data are presented with filled circles, while data from the LT, GIT, Keck, WHT, and LCO are presented as filled diamonds, squares, elongated diamonds, crosses, and pentagons, respectively. Absolute magnitude is shown for the candidates with a known redshift, and upper limits are shown as inverted triangles. We also display the spectra of the transient where available and mark the hydrogen and helium lines for ZTF19aasmddt (SN II), the H and He II features of ZTF19abvionh (CV), and the Mg I and Mg II lines for ZTF19abvizsw (long GRB afterglow).

Table 2
List of Candidate Counterparts to S190426c

Name	TNS	R.A.	Decl.	Host/Redshift	Discov. Mag	Rejection Crit.
ZTF19aasmftm	AT2019sne	325.9004479	77.8315634	0.156 [s]	$g = 18.78 \pm 0.19$	SN Ia
ZTF19aaszjf	AT2019snh	320.6262982	65.8134516	0.028 [s]	$g = 19.45 \pm 0.14$	SN Ia
ZTF19aasmddt	SN2019fht	299.25055	9.7016748	0.028 [s]	$g = 18.6 \pm 0.11$	SN II
ZTF19aasmekb	AT2019snl	300.6013987	14.2873159	...	$g = 17.33 \pm 0.04$	$\alpha_g = 0.24$
ZTF19aassfws	AT2019fuc	298.6678611	61.2400121	...	$r = 21.35 \pm 0.21$	Artifact
ZTF19aaslszp	AT2019snj	301.3434628	53.3990477	0.084 [s]	$g = 20.12 \pm 0.15$	$\alpha_r = 0.01$, AGN
ZTF19aaslof	AT2019snn	288.7838539	79.4357187	...	$r = 21.12 \pm 0.18$	$\alpha_r < 0.01$, AGN, PS1
ZTF19aaslozu	AT2019snr	306.3144981	65.1093759	...	$r = 20.59 \pm 0.21$	$\alpha_g = 0.06$, AGN, PS1
ZTF19aasshpf	AT2019snt	315.4768651	70.2055771	...	$r = 19.99 \pm 0.23$	$\alpha_r < 0.01$
ZTF19aaslphi	AT2019sno	297.3809977	61.9605925	...	$r = 21.26 \pm 0.20$	$\alpha_r = -0.08$
ZTF19aaslpds	AT2019snq	306.2625186	61.521461	...	$r = 19.9 \pm 0.14$	$\alpha_r = 0.03$
ZTF19aasmzqf	AT2019aaco	353.5204911	78.9577781	...	$r = 19.86 \pm 0.09$	$\alpha_r = 0.01$
ZTF19aaslzfk	AT2019snd	308.968271	72.3536353	...	$g = 20.0 \pm 0.26$	$\alpha_g = -0.02$
ZTF19aaslvwn	AT2019snf	299.059846	46.463559	...	$g = 20.68 \pm 0.17$	$\alpha_r < 0.01$
ZTF19aasmdir	AT2019sng	300.2360007	9.504002	...	$g = 20.07 \pm 0.11$	$\alpha_r < 0.01$

Table 3
List of Candidate Counterparts to S190901ap

Name	TNS	R.A.	Decl.	Host/Redshift	Discov. Mag	Rejection Crit.
ZTF19abvizsw	AT2019pim	279.47282	61.497984	1.26 [s]	$r = 19.89 \pm 0.16$	Long GRB afterglow
ZTF19abwvals	AT2019pni	73.250555	12.69303	0.091 [s]	$r = 18.96 \pm 0.30$	SN Ia
ZTF19abvixoy	AT2019pin	279.552972	27.420935	...	$r = 18.93 \pm 0.10$	$\alpha_r = 0.23$, CV
ZTF19abvionh	AT2019pip	253.750924	14.05133	0.0985 [s]	$g = 20.57 \pm 0.31$	$\alpha_g = 0.10$, CV
ZTF19abwsmmd	AT2019pnc	22.666409	-19.712405	0.0972 [s]	$g = 19.78 \pm 0.18$	$\alpha_g = 0.03$
ZTF19abvislp	AT2019pnx	220.349708	54.151153	0.10 [s]	$r = 19.98 \pm 0.20$	$\alpha_r = 0.05$
ZTF19abxdvcs	AT2019qev	252.010477	41.920087	...	$g = 20.64 \pm 0.28$	$\alpha_g = 0.03$

Table 4
List of Candidate Counterparts to S190910d

Name	TNS	R.A.	Decl.	Host/Redshift	Discov. Mag	Rejection Crit.
ZTF19abyfhov	AT2019pvu	260.693429	11.424436	0.13 [s]	$g = 19.92 \pm 0.22$	SN Ia
ZTF19abyfbii	AT2019pvz	255.44162	11.602254	0.118 [s]	$r = 19.60 \pm 0.16$	SN Ia 91T
ZTF19abyfazm	AT2019pwa	290.535876	48.069162	0.38 [s]	$g = 17.53 \pm 0.03$	CV, $\alpha_r = 0.09$
ZTF19abyfhaq	AT2019pvv	303.148593	49.392607	0 [s]	$g = 18.01 \pm 0.31$	$\alpha_r = 0.15$, Galactic

Table 5
List of Candidate Counterparts to S190910h

Name	TNS	R.A.	Decl.	Host/Redshift	Discov. Mag	Rejection Crit.
ZTF19abyheza	AT2019pxi	332.913391	60.395816	0 [s]	$r = 16.14 \pm 0.13$	CV, $\alpha_r = 0.08$
ZTF19abyhhml	AT2019pxj	339.691635	55.936649	0 [s]	$r = 17.36 \pm 0.12$	CV, $\alpha_r = 0.13$
ZTF19abyirjl	AT2019pxe	30.471176	30.73355	0.1 [s]	$r = 19.45 \pm 0.13$	SN Ia
ZTF19abyjcom	AT2019pxk	32.936353	12.033344	...	$r = 19.63 \pm 0.24$	Artifact
ZTF19abyjcon	AT2019pxl	33.252469	12.472604	...	$r = 19.87 \pm 0.19$	Artifact
ZTF19abyjcoo	AT2019pxm	33.089712	12.297698	<0.03 [p]	$r = 19.95 \pm 0.24$	$\alpha_r = 0.06$
ZTF19abyjfiw	AT2019pxn	39.186807	34.647299	...	$g = 20.13 \pm 0.21$	$\alpha_r < 0.01$
ZTF19abygvmp	AT2019pzz	28.976258	41.090979	0.049 [s]	$r = 20.13 \pm 0.25$	SN II
ZTF19abymiwiw	AT2019pzi	340.521441	55.220244	...	$r = 18.58 \pm 0.30$	$\alpha_g = 0.20$
ZTF19abylleu	AT2019pyu	355.338225	-23.450706	...	$r = 19.19 \pm 0.24$	$\alpha_g = 0.03$
ZTF19abymhyi	AT2019pzh	340.85572	34.186344	<0.03 [p]	$g = 20.36 \pm 0.23$	$\alpha_g = -0.13$

Table 6
List of Candidate Counterparts to S190923y

Name	TNS	R.A.	Decl.	Host/Redshift	Discov. Mag	Rejection Crit.
ZTF19acbmopl	AT2019rob	114.040207	28.487381	<0.03 [p]	$g = 19.64 \pm 0.27$	$\alpha_g = 0.01$

Table 7
List of Candidate Counterparts to S190930t

Name	TNS	R.A.	Decl.	Host/Redshift	Discov. Mag	Rejection Crit.
ZTF19acbpqlh	AT2019rpn	319.9216636	37.5220721	0.026 [s]	$g = 19.47 \pm 0.18$	SN II
ZTF19acbwaah	AT2019rpp	162.3277489	22.9827302	0.031 [s]	$r = 17.61 \pm 0.08$	SN Ia
ATLAS19wyn	AT2019rpj	339.8367397	31.4916262	0.0297 [s]	$g = 19.32 \pm 0.11$	SN II

Table 8
List of Candidate Counterparts to S191205ah

Name	TNS	R.A.	Decl.	Host/Redshift	Discov. Mag	Rejection Crit.
ZTF19acxpnd	AT2019wkv	175.361851	8.241201	<0.03 [p]	$i = 19.58 \pm 0.20$	$\alpha_g = 0.06$
ZTF19acxoywk	AT2019wix	149.896148	13.915051	0.05 [s]	$r = 19.69 \pm 0.21$	$\alpha_g = -0.15$
ZTF19acxoyra	AT2019wid	153.093775	8.609330	0.09 [s]	$r = 19.14 \pm 0.19$	$\alpha_g = 0.05$
ZTF19acxpwlh	AT2019wiy	155.712970	23.603273	<0.24 [p]	$g = 19.77 \pm 0.19$	$\alpha_r = 0.07$
ZTF19acyiflj	AT2019wmy	152.899874	23.943843	0.081 [s]	$r = 20.05 \pm 19.63$	SN Ia
ZTF19acxowrr	AT2019wib	154.871458	27.883738	0.05 [s]	$r = 19.00 \pm 0.13$	SN II
ZTF19acyitga	AT2019wmn	159.796830	5.161942	0.071 [s]	$r = 19.20 \pm 0.16$	SN Ia

Table 9
List of Candidate Counterparts to S191213g Reported in GCN 26424 and 26437

Name	TNS	R.A.	Decl.	Host/Redshift	Discov. Mag	Rejection Crit.
ZTF19acykzsk	SN2019wqj	32.904547	34.041346	0.021 [s]	$g = 19.0 \pm 0.06$	SN II
ZTF19acymaru	AT2019wnh	80.461954	-19.266401	0.167 [s]	$r = 19.92 \pm 0.16$	SN Ia
ZTF19acykzsp	AT2019wne	28.359144	31.801012	0.16 [s]	$r = 20.08 \pm 0.31$	SN Ia
ZTF19acyfoha	AT2019wkl	85.104365	-18.097630	0.04 [s]	$g = 17.31 \pm 0.08$	SN Ia
ZTF19acymcww	AT2019wni	36.248920	47.497844	0.09 [s]	$r = 19.76 \pm 0.24$	SN Ia
ZTF19acykwsd	AT2019wnl	33.088072	41.388708	...	$r = 19.3 \pm 0.25$	Artifact
ZTF19acylvus	AT2019wnk	83.631136	-19.420244	0.104 [s]	$r = 19.45 \pm 0.24$	SN Ia
ZTF19acymcna	AT2019wnn	33.207899	40.999726	0.138 [s]	$r = 20.48 \pm 0.22$	$\alpha_r = -0.01$, AGN
ZTF19acykyqu	AT2019wre	38.819646	38.319851	...	$g = 20.94 \pm 0.21$	Stellar—PS1-DR2
ZTF19acykyrz	AT2019wrf	36.064972	38.080388	...	$g = 20.83 \pm 0.17$	Stellar—PS1-DR2
ZTF19acykyzj	AT2019wrg	36.056624	51.367126	...	$g = 19.75 \pm 0.20$	$\alpha_r = -0.03$
ZTF19acykzfy	AT2019wrh	43.115194	41.660303	...	$g = 20.34 \pm 0.20$	Stellar—PS1-DR2
ZTF19acyldum	AT2019wrn	79.681883	-7.185279	...	$g = 19.41 \pm 0.13$	PS1-DR2 detection
ZTF19acyldun	AT2019wrt	79.199993	-7.478682	0.057 [s]	$g = 19.42 \pm 0.17$	$\alpha_r = 0.09$, LBV
ZTF19acymapa	AT2019wro	78.207321	-5.948936	...	$g = 18.54 \pm 0.22$	$\alpha_r^* = -0.06$
ZTF19acymaxu	AT2019wrp	82.952485	-26.694523	<0.13 [p]	$r = 18.65 \pm 0.06$	$\alpha_r = 0.03$
ZTF19acymixu	AT2019wrr	90.913936	60.728245	0.14 [s]	$r = 19.66 \pm 0.32$	SN Ia
ZTF19acymlhi	AT2019wrs	91.592426	-18.804727	...	$r = 17.99 \pm 0.26$	$\alpha_r^* = -0.17$

Note. The candidates for which photometric evolution has been calculated with a baseline (Δt) between 2 and 3 days are marked with ‡.

first transient detection disfavor their multimessenger association with S190930t or S190910d, respectively (see Figure 8).

Of the 432 sources with only one detection in the ZTF alert stream, only nine candidates passed the visual inspection of the images and light curves. Most other candidates were ruled out as stellar flares, image subtraction artifacts, asteroids, or sporadic nuclear variability. Of these nine candidates, six had photometric or spectroscopic redshifts of the host galaxy too far to be consistent with the GW distance. All three remaining candidates were found during follow-up of S190901ap: ZTF19abvpeir, ZTF19abvozxv, and ZTF19abvphxm. All three are likely SNe or AGNs, given that their absolute magnitudes at the distance of their putative hosts are between -18.0 and -18.8 mag and their locations are consistent with the Galaxy nuclei. We show some light curves and host galaxies in Figure 8.

In summary, all candidates were ruled out as possible kilonovae in both the real-time and offline analyses.

4. Discussion

We start by treating all triggers as bona fide astrophysical events regardless of FAR, assuming that kilonovae accompanying BNS and NSBH mergers are drawn from a common population, and analyzing the implications of zero kilonova detections. Later, we relax these assumptions. Since kilonova models have a wide range of estimates depending on several intrinsic and extrinsic parameters (e.g., ejecta mass, ejecta velocity, lanthanide fraction, viewing angle, remnant lifetime), we took a model-independent approach toward constraining the luminosity function.

Serving as our benchmark is GW170817. The ZTF observations were taken as g - and r -band pairs, and GW170817 was discovered at an i -band magnitude of 17.3 mag about 10.8 hr after merger (Coulter et al. 2017). Compiling and fitting all published data in the g and r bands for GW170817 in the first 3 days after merger (Andreoni et al. 2017; Arcavi et al. 2017; Coulter et al. 2017; Cowperthwaite et al. 2017; Díaz et al. 2017;

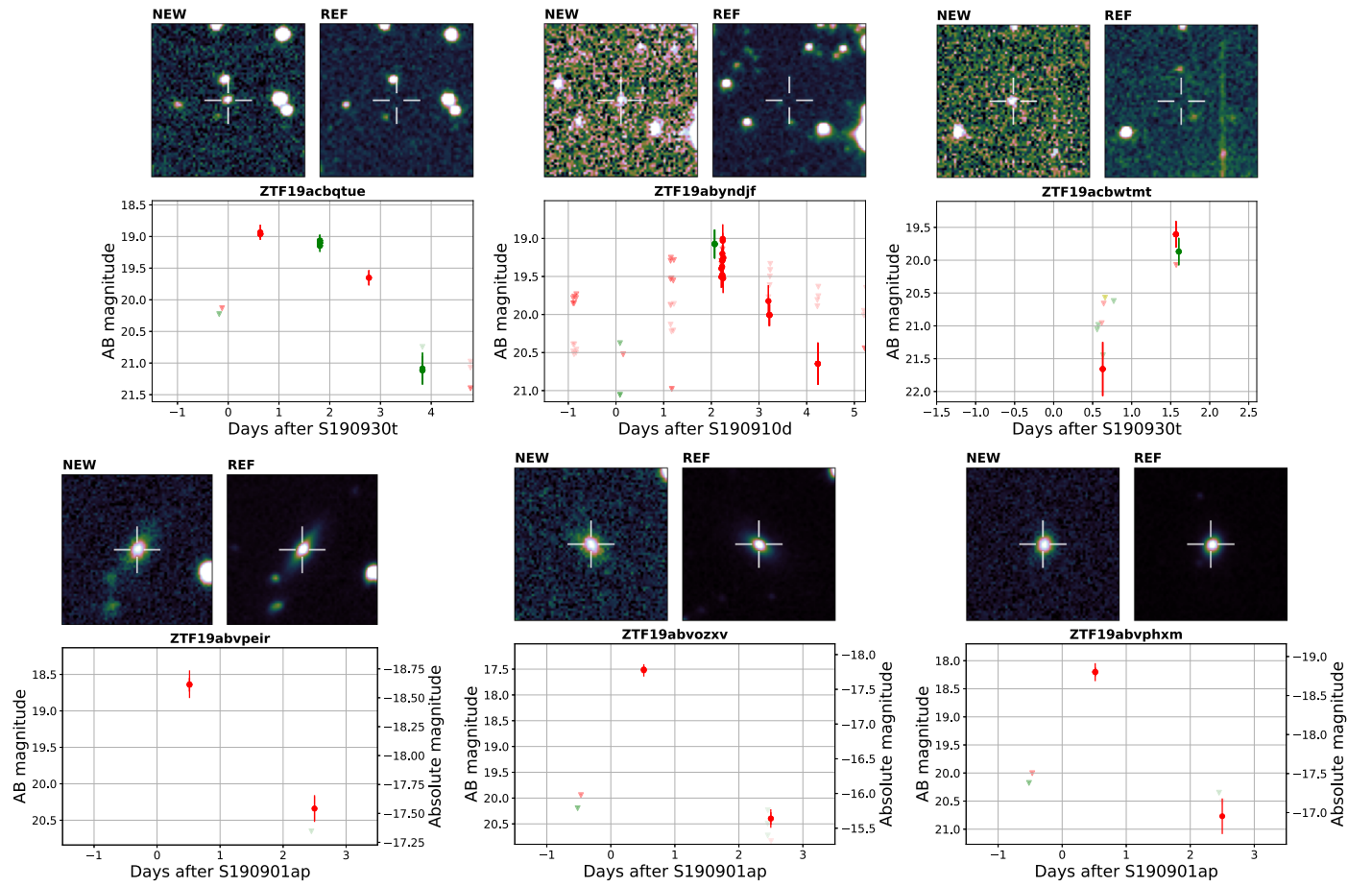


Figure 8. Collage of candidate counterparts found in deeper offline searches. Each candidate in the top row has two or more ZTF alerts: ZTF19acbqtue was ruled out, as we found a quiescent stellar source with GMOS-N; ZTF19abyndjf does not have a galaxy in its vicinity; and ZTF19acbwmt had archival activity in PS1-DR2. Each candidate in the bottom row had only one ZTF alert but was flagged as interesting after performing forced photometry. These three candidates are nuclear transients that are ruled out, as their absolute magnitudes are brighter than what is expected for kilonovae.

Table 10
List of Candidate Counterparts to S200213t

Name	TNS	R.A.	Decl.	Host/Redshift	Discov. Mag	Rejection Crit.
ZTF20aamvqxl	AT2020ciy	29.237921	53.668882	0.102 [s]	$g = 19.44 \pm 0.17$	SN Ia
ZTF20aamvnth	AT2020cjb	18.337721	49.645539	0.061 [s]	$g = 19.95 \pm 0.17$	SN II
ZTF20aamvoxx	AT2020cjc	39.399095	26.920616	0.097 [s]	$g = 19.47 \pm 0.12$	SN Ia
ZTF20aamvtip	AT2020cje	38.082538	27.810094	0.151 [s]	$g = 20.3 \pm 0.16$	SN Ia
ZTF20aamvnat	AT2020ciz	27.239552	56.354579	0.0 [s]	$g = 17.42 \pm 0.05$	CV
ZTF20aamvmzj	AT2020cja	27.189195	51.430481	...	$g = 19.46 \pm 0.11$	$\alpha_r = 0.04$
ZTF20aamvoeh	AT2020cjc	33.502011	38.936317	0.14 [s]	$g = 20.25 \pm 0.12$	SN Ia
ZTF20aamvodd	AT2020cjf	37.482387	50.319427	0.0 [s]	$g = 18.92 \pm 0.11$	Stellar flare
ZTF20aanakwb	AT2020cls	6.5215391	42.7737224	...	$g = 20.75 \pm 0.27$	Stellar
ZTF20aanaltd	AT2020clt	9.7406716	43.4410695	0.2 [s]	$g = 20.57 \pm 0.23$	SN Ia
ZTF20aanaksk	AT2020clu	19.4356399	31.1744954	$<0.03 [p]$	$g = 20.27 \pm 0.10$	PS1
ZTF20aanallx	AT2020clv	6.3666608	51.2233877	...	$g = 20.58 \pm 0.28$	Outside the LALInfernce map
ZTF20aanaoyz	AT2020clw	24.5940995	23.3822569	0.276 [s]	$g = 21.28 \pm 0.27$	SN Ia
ZTF20aamvpvx	AT2020clx	31.9402981	20.0306147	0.074 [s]	$g = 19.95 \pm 0.14$	SN II
ZTF20aanamcs	AT2020cerc	13.7433345	43.4980245	0.093 [s]	$g = 20.98 \pm 0.28$	SN II
ZTF20aanakge	AT2020crd	12.6306233	41.484178	0.1272 [s]	$g = 20.38 \pm 0.33$	SN Ia
ZTF20aanaqhe	AT2020cre	17.0425796	45.5256583	...	$g = 20.63 \pm 0.27$	$\alpha_g = -0.08$
ZTF20aanakes	AT2020cly	2.0985443	38.0441264	...	$g = 20.79 \pm 0.21$	PS1
ZTF20aanakcd	AT2020cmr	8.1571223	41.3156371	0.077 [s]	$g = 20.48 \pm 0.17$	SN IIn

Drout et al. 2017; Evans et al. 2017; Pian et al. 2017; Smartt et al. 2017; Utsumi et al. 2017; Valenti et al. 2017; Pozanenko et al. 2018), we find that GW170817 had a decline rate of

0.9 mag day^{-1} in the r band and 1.3 mag day^{-1} in the g band. Extrapolating this decline rate to merger time and correcting for line-of-sight extinction, GW170817 may have peaked at

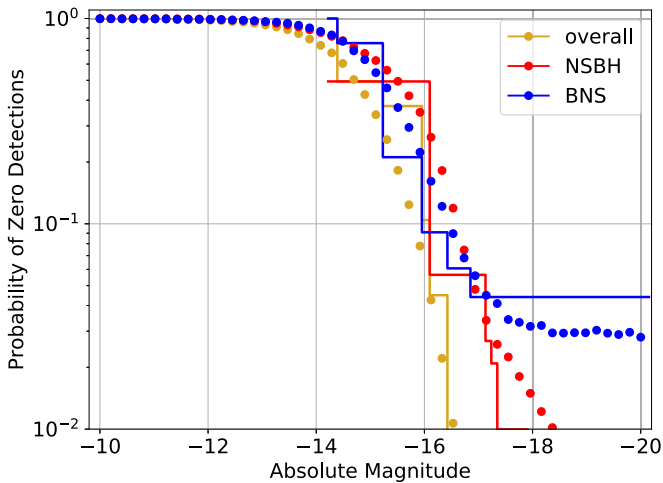


Figure 9. Joint probability of zero detections as a function of absolute magnitude of the kilonova after correcting for line-of-sight extinction. Solid lines represent rough estimates from median estimates. Filled circles represent estimates that take into account the spatial variation in depth, GW distance, and GW probability.

−16.54 mag in the r band and −16.69 mag in the g band (we caution that some kilonova models predict a finite rise time). Here we choose to compare the ZTF limits to an average of these two filters, i.e., −16.6 mag at peak and a decline rate of 1 mag day^{−1}.

4.1. Joint Probability of Zero Detections

We estimate the joint probability of zero kilonova detections as a product of $(1 - q_i)$ terms, where q_i is the enclosed probability for each event as listed in Table 1 (see the sixth column; we used LALInference probability where available). If we were sufficiently sensitive to finding kilonovae in all 13 GW events, the joint probability of zero detections would be only 0.017%. However, each merger had a different observed depth, observed cadence, and GW distance estimate and thus a different sensitivity to detecting kilonovae.

First, we use the median image depth for each trigger and the median GW distance to each trigger to compute a median absolute magnitude sensitivity limit. We correct the median absolute magnitude for the median extinction along the line of sight. In Figure 9, in each luminosity bin, we compute the joint nondetection probability only for the subset of events for which the ZTF observations were sufficiently sensitive. We find that ZTF follow-up of four (six) GW events had a sensitivity deeper than −16.0 mag (−16.6 mag), and the joint nondetection probability is only 4.5% (0.34%). Moreover, three of the four (four of the six) had a preliminary BNS classification, and for all three, the ZTF follow-up began within 4 hr of merger (see Table 1).

Second, we use injection and recovery of fake sources to better quantify both the degree of variation in the depths of individual exposures and the spatial variation in the GW distance estimates. We use an open-source tool called `simsurvey`⁷⁵ (Feindt et al. 2019). As input, the tool takes a list of ZTF pointings (observation time, R.A., decl., limiting magnitude, filters, processing success of each CCD quadrant). We inject 10,000 sources distributed according to the 3D GW sky map probability distribution in each luminosity bin (50 bins between −10 and −20 mag). Initially, we assume that each

kilonova stays at a constant luminosity between the merger time and 3 days after merger. We require a single observation at the necessary depth for recovery. In addition to losing sources in unobserved fields, we lose sources that land in ZTF chip gaps, chips that failed processing, or chips that were less sensitive due to higher line-of-sight Galactic extinction. This tool does not take into account any detections that would be lost to inefficiency in the software pipeline.

The recovery fraction for each event is shown in Figure 10. We convert this to a joint nondetection probability estimate by multiplying $(1 - p_i)$ in each luminosity bin and overlay this as discrete points on the median estimates above in Figure 9. We find consistent results; the joint probability of zero detections at −16.1 mag (−16.6 mag) is only 4.2% (0.8%). If we separate the NSBH and BNS populations, the joint nondetection probability at −16.6 mag is 9.7% for NSBH and 7.9% for BNS. This is not surprising, as the BNS triggers were, on average, closer than the NSBH triggers. We note that this application of `simsurvey` is different compared to previous applications for SN rates, which were uniform in volume. Taking into account the exact 3D GW sky map is more accurately representative of our success in searching for the counterpart to a GW source on an event-by-event basis.

Third, in addition to spatial variations in depth and distance, we take into account the possible time variations in the light curves of kilonovae (Figure 11). The time window for our observations is limited to within 3 days of merger. We relax the constant luminosity assumption above and inject kilonovae into `simsurvey` that fade linearly between zero and 1 mag day^{−1}. In Figure 11, we color-code the recovery efficiency for a given peak luminosity and photometric decay rate in any filter (g or r band). Any slice of this plot can be converted to a joint probability of zero detections as a function of absolute magnitude. We compare to the GW170817 benchmark of an extrapolated peak of −16.6 mag day^{−1} and a fade rate of 1 mag day^{−1}. We find a joint probability of zero detections of 7%.

Fourth, in addition to spatial and time variations, we inject kilonova models into `simsurvey` and calculate the recovery fraction. We use the best fit to GW170817 from the kilonova model grid in Dietrich et al. (2020) computed using the radiative transfer code `POSSIS` (Bulla 2019). This model fit assumes a rise time, color evolution, and viewing angle of GW170817. The joint nondetection probability is 30%. Even if all kilonova ejecta parameters were similar to GW170817, the viewing angle would be different for different events. Assuming random viewing angles drawn from a distribution uniform in $\cos(\theta)$, we inject a model grid and find that the joint nondetection probability is 49%. We caution that the model used here underestimates the early g -band flux of GW170817 by 0.3 mag; thus, the recovery fraction estimated here could also be underestimated.

4.2. Constraining the Kilonova Luminosity Function

Next, we consider the implications of the zero-detection probability function on the underlying luminosity function. Let us say the luminosity function dictates that a fraction f_b of kilonovae are brighter than a given absolute magnitude. Then,

$$(1 - \text{CL}) = \prod_{i=1}^N (1 - f_b^* p_i),$$

where CL is the confidence level and p_i is the event-by-event probability of detection. At a given absolute magnitude, we

⁷⁵ <https://github.com/ZwickyTransientFacility/simsurvey>

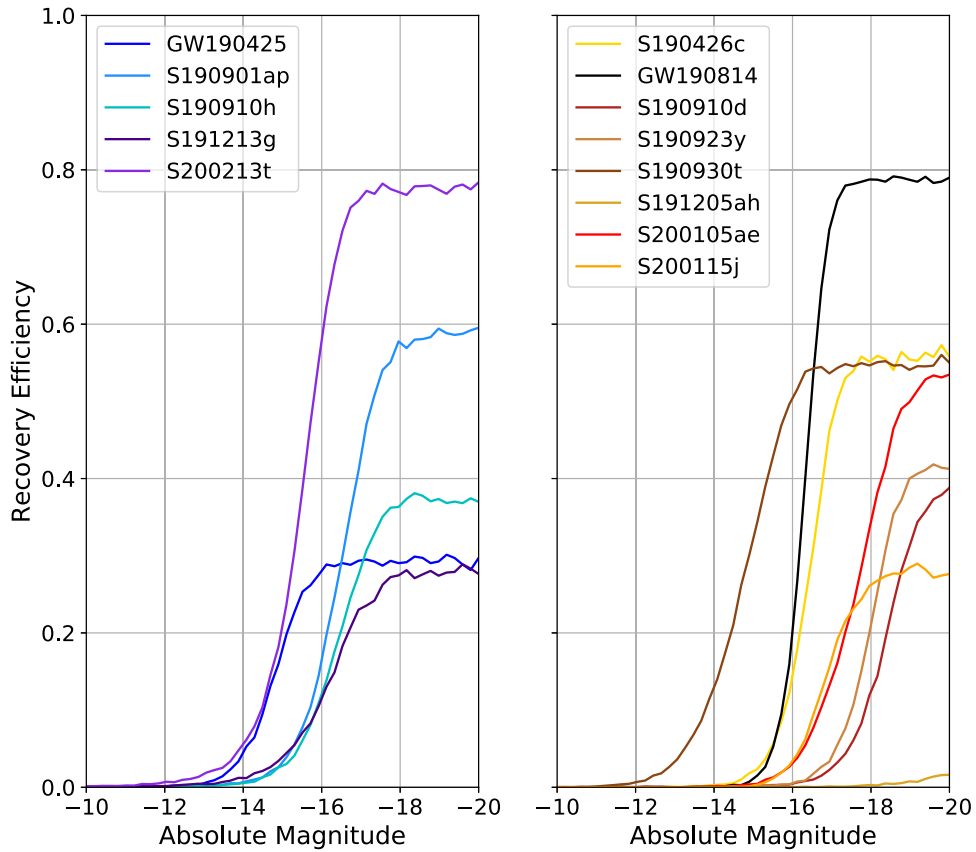


Figure 10. Event-by-event recovery efficiency using `simsurvey` as a function of absolute magnitude for BNS (left panel) and NSBH (right panel) mergers. The recovery efficiency corresponds to the number of kilonovae detected divided by the total number of kilonovae injected. Kilonovae were injected according to the 3D probability distribution of the sky map.

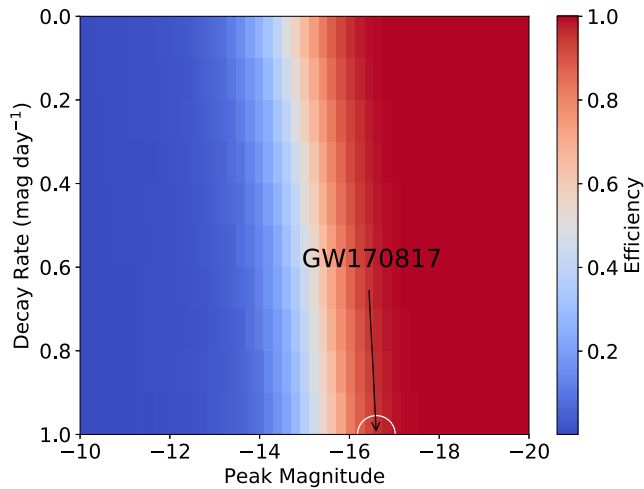


Figure 11. Composite efficiency map using `simsurvey` assuming a linear model for the kilonova with a peak absolute magnitude and fixed decay rate. The color-coding shows the recovery efficiency, or the number of recovered kilonovae within observed regions divided by the total number of kilonovae injected in the sky map. Based on an analysis of a compilation of data from GW170817 (Andreoni et al. 2017; Coulter et al. 2017; Cowperthwaite et al. 2017; Díaz et al. 2017; Drout et al. 2017; Evans et al. 2017; Pian et al. 2017; Smartt et al. 2017; Utsumi et al. 2017; Valenti et al. 2017; Arcavi 2018; Pozanenko et al. 2018), we compute an average extrapolated peak magnitude of ~ -16.6 and a decay rate of $\sim 1 \text{ mag day}^{-1}$. If all kilonovae are like GW170817, the joint probability of zero detections is 7%.

compute p_i as the recovery fraction from the `simsurvey` injections for the fading and flat light-curve evolution estimates discussed above that take into account the spatial

variation in distance, depth, and enclosed probability. Solving for f_b at a 90% confidence level, we plot our results in Figure 12. At the bright end, we find that no more than $\approx 40\%$ of kilonovae can be brighter than -18 mag. At the faint end, our observations place no constraints on the luminosity function fainter than -15.5 mag. The luminosity of GW170817 at the merger time is unknown, and various models predict diverse rates of evolution in that first day after merger. As discussed above, we use an extrapolated peak of -16.6 mag and a fade rate of 1 mag day^{-1} for GW170817 as a benchmark. We find that no more than $<57\%$ ($<89\%$) of kilonovae could be brighter than -16.6 mag for the flat (fading) light-curve assumptions.

The GW triggers had a very wide range of FARs. Weighting by the available low-latency values for the terrestrial probability (t_i), we fold this into our luminosity function constraint as

$$(1 - \text{CL}) = \prod_{i=1}^N (1 - f_b^* p_i^* (1 - t_i)).$$

In Figure 12, we show that the resulting constraints on f_b (red line) are worse only by a difference of $\approx 10\%$.

Next, we investigate the implications of this constraint on the kilonova parameter space. There are no theoretical luminosity functions available in the literature that we can directly compare to. A model grid is available (Kasen et al. 2017) as a function of three parameters: ejecta mass M_{ej} , ejecta velocity v_{ej} , and

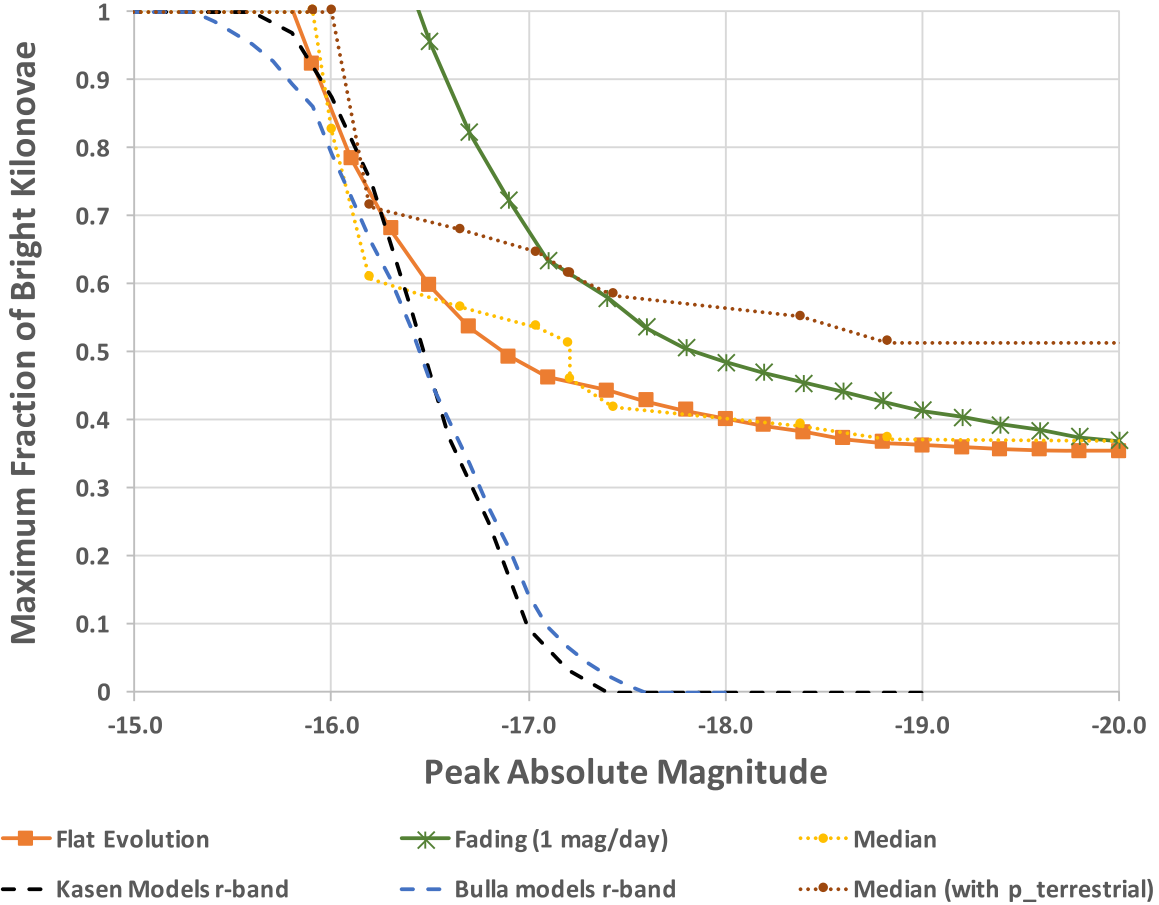


Figure 12. Constraints on the underlying luminosity function of kilonovae represented as the maximum allowed fraction of kilonovae brighter than a given peak absolute magnitude. Constraints are derived at a 90% confidence level. We show constraints assuming flat photometric evolution (orange squares) and fading by 1 mag day^{-1} (green asterisks). We also show the event-by-event constraint based on a median estimate (yellow circles, dotted line). We correct this median estimate by the probability that the GW alert was terrestrial (red circles, dotted line). We compare to a model grid published in Kasen et al. (2017; dashed black line) and find that the limiting line suggests that some kilonovae must either have $M_{\text{ej}} < 0.03 M_{\odot}$ or $X_{\text{lan}} > 10^{-4}$. The limiting line (blue dashed line) for another model grid (Bulla 2019; Dietrich et al. 2020) suggests that some kilonovae must be fainter than GW170817 with $M_{\text{ej,dyn}} < 0.005 M_{\odot}$, $M_{\text{ej,pm}} < 0.05 M_{\odot}$, or $\phi > 30^{\circ}$.

lanthanide fraction X_{lan} . The best-fit model to GW170817 from Kasen et al. (2017) suggested two components: a blue kilonova ($0.025 M_{\odot}$, $0.3 c$, $10^{-4.5}$) and a red kilonova ($0.04 M_{\odot}$, $0.1 c$, 10^{-2}). The blue component dominates at an early time and is more relevant to the ZTF searches described in this paper. Comparing to our luminosity function constraints, we find that our limits suggest that a wide range of parameters are allowed, e.g., $M_{\text{ej}} = [0.03, 0.1] M_{\odot}$, $v_{\text{ej}} = [0.05, 0.3] c$, and $X_{\text{lan}} = [10^{-5}, 10^{-4}]$; stricter distributions that yield a brighter kilonova population (e.g., higher ejecta mass or lower lanthanide fraction) are not allowed. Thus, some kilonovae must have $M_{\text{ej}} \leq 0.03 M_{\odot}$ or $X_{\text{lan}} > 10^{-4}$ to be consistent with the ZTF constraints.

Similarly, we compare our luminosity function constraints to the kilonova grid from Dietrich et al. (2020) computed using the radiative transfer code POSSIS (Bulla 2019). In addition to the observer viewing angle, this grid depends on three parameters: the dynamical ejecta mass ($M_{\text{ej,dyn}}$), the postmerger wind ejecta mass ($M_{\text{ej,pm}}$), and the half-opening angle of the lanthanide-rich ejecta component (ϕ). A model with $M_{\text{ej,dyn}} = 0.005 M_{\odot}$, $M_{\text{ej,pm}} = 0.05 M_{\odot}$, and $\phi = 30^{\circ}$ provides a good fit to GW170817 (see Figure 8 of Dietrich et al. 2020). As shown in Figure 12, our constraints suggest that some kilonovae must be fainter than GW170817, i.e., must have either $M_{\text{ej,dyn}} < 0.005 M_{\odot}$, $M_{\text{ej,pm}} < 0.05 M_{\odot}$, or $\phi > 30^{\circ}$.

5. Conclusions and Way Forward

In summary, the ZTF coverage (excluding weather-impacted S191205ah) spanned enclosed probabilities from 22% to 89%, median depths from 20.1 to 21.5 mag, and time lags between merger and the start of observations from 11 s to 13.7 hr. The follow-up by the GROWTH team comprised 340 UltraViolet/Optical/InfraRed (UVOIR) photometric points, 64 OIR spectra, and three radio images. Additionally, many other teams also followed up ZTF candidates. Thanks to the extensive follow-up, all candidate counterparts were ruled out.

The GW triggers had localization areas ranging from 23 to 24,264 deg^2 , distances from 108 to 632 Mpc, and FARs from 1.5 to 10^{-25} yr^{-1} . Assuming that all GW alerts were astrophysical, we conclude that the joint probability of zero detections is only 4.2% if all kilonovae are at least as bright as GW170817 at discovery. Furthermore, assuming kilonovae from BNS and NSBH mergers are drawn from a common population, we find that no more than <57% (<89%) of kilonovae could be brighter than -16.6 mag for the flat (fading by 1 mag day^{-1}) assumptions respectively at 90% confidence.

The median time lag of the ZTF observations in O3 was only 1.5 hr after merger. This further constrains the unknown, early-time emission of kilonovae in the g and r bands. Some models predict that the early emission could be very hot and bright in

the UV; this can only be addressed once wide-field UV imagers (e.g., Dorado, ULTRASAT, and DUET) are launched.

Given the expected differences in sensitivity between the LIGO and Virgo interferometers, events in O4 are likely to be similarly coarsely localized (until KAGRA or LIGO India come online with high sensitivity). Moreover, given the increased GW sensitivity, we expect more events that are further away. Thus, we plan to implement stricter selection criteria. Specifically, for O4, we plan to only trigger on events with FARs lower than 1 yr^{-1} (i.e., four out of 15 events in O3 would fail this criterion). We plan to only trigger on NSBH events with a nonzero HasRemnant probability (i.e., six out of eight NSBH triggers in O3 would fail this criterion, including GW190814). As we did in O3, we plan to only trigger on MassGap events with a nonzero HasNS probability. In summary, only five out of the 13 events followed up in O3 would pass our new plan for trigger criteria in O4.

The first phase of the ZTF survey ran from 2018 March to 2020 September. The second phase of the ZTF is expected to run from 2020 October to 2023 September. Searches with ZTF Phase II are planned to be up to 2 mag deeper than nominal survey operations, even with 1000 deg^2 localizations, thanks to the availability of deeper stacks as reference images. We plan to require a minimum median image depth of -16.0 mag and minimum enclosed probability of 50% in the first 4 hr of observations. The ZTF mapping speed allows 3600 deg^2 to be mapped in 4 hr to achieve the necessary depth for a median GW distance of 300 Mpc. If the event is more distant, we will increase our exposure time from 180 to 600 s to go deeper. For events that are either too distant or too coarsely localized, we will not undertake triggered searches and will rely only on serendipitous searches of the all-sky public survey at 2 days' cadence to 20.4 mag.

Moreover, redder searches will better constrain the kilonova phase space and probe higher lanthanide fractions. The ZTF II would push to the red, since broader reference coverage is now available in the *i*-band filter (see Sagués Carracedo et al. 2020 for detailed simulations on gain in depth and red sensitivity). New wide-field infrared surveyors are also coming online (e.g., WINTER at Palomar Observatory, USA, and DREAMS at Siding Springs Observatory, Australia)

We look forward to searches in the fourth observing run, as detections will be more likely. For zero detections, about 17 neutron star mergers with only 50% enclosed probability to a depth of -16 mag would constrain the luminosity function fraction brighter than GW170817 to $<25\%$ (only 11 events with 75% enclosed probability would place a similarly stringent limit). Thus, as the sample size grows, even with partial coverage of sky maps, the luminosity function of kilonovae will be strongly constrained.

We conclude with some thoughts on what would strengthen the partnership between the GW physics community and the EM astronomy community. First, we encourage efforts that would speed up the release of the more accurate LALInference map (Veitch et al. 2015). Since the LALInference map was often only available after our observations were completed, our net expectation value dropped by 10%, and our net joint nondetection probability dropped by a factor of 2 between the BAYESTAR (Singer & Price 2016) map and the LALInference map. Moreover, three triggers never had an LALInference map released (S190923y, S190930t, and S191205ah).

Second, it is critical that a reliable FAR and terrestrial probability are released as soon as possible. If an event is going to be retracted (or the FAR increases significantly) based on offline analysis, it is essential that the EM community be notified immediately via GCN, so that all pending follow-up can be halted. Third, if the classification of an event changes in offline analysis, the EM community should be promptly notified via GCN. Fourth, since HasNS and HasRemnant are somewhat model-dependent (e.g., Foucart et al. 2018; Chatterjee et al. 2020) but will drive the decision of whether or not some EM teams trigger follow-up, we request the release of rough estimates/ranges for more directly determined parameters (e.g., mass ratio, inclination, and chirp mass) that can help with the EM decision. We strongly encourage any algorithmic or technological development that will enable more accurate 3D skymaps, FARs, HasNS, and HasRemnant at lower latency to better inform the EM community's follow-up decisions.

In summary, the lessons learned from both the single detection in O2 and the dozen nondetections in O3 bode well for an exciting future for multimessenger astrophysics in the coming decade.

This work was supported by the Global Relay of Observatories Watching Transients Happen (GROWTH) project, funded by the National Science Foundation under PIRE grant No. 1545949. GROWTH is a collaborative project among the California Institute of Technology (USA), University of Maryland College Park (USA), University of Wisconsin Milwaukee (USA), Texas Tech University (USA), San Diego State University (USA), University of Washington (USA), Los Alamos National Laboratory (USA), Tokyo Institute of Technology (Japan), National Central University (Taiwan), Indian Institute of Astrophysics (India), Indian Institute of Technology Bombay (India), Weizmann Institute of Science (Israel), The Oskar Klein Centre at Stockholm University (Sweden), Humboldt University (Germany), Liverpool John Moores University (UK), and University of Sydney (Australia). Based on observations obtained with the Samuel Oschin Telescope 48 inch and the 60 inch telescope at the Palomar Observatory as part of the Zwicky Transient Facility project. The ZTF is supported by the National Science Foundation under grant No. AST-1440341 and a collaboration including Caltech, IPAC, the Weizmann Institute for Science, the Oskar Klein Center at Stockholm University, the University of Maryland, the University of Washington, Deutsches Elektronen-Synchrotron and Humboldt University, Los Alamos National Laboratories, the TANGO Consortium of Taiwan, the University of Wisconsin at Milwaukee, and Lawrence Berkeley National Laboratories. Operations are conducted by COO, IPAC, and UW. The ZTF forced photometry service was funded under Heising-Simons Foundation grant No. 12540303 (PI: Graham). The SED Machine is based upon work supported by the National Science Foundation under grant No. 1106171.

The GROWTH-India telescope is a 70 cm telescope with a 0.7° field of view, set up by the Indian Institute of Astrophysics and the Indian Institute of Technology Bombay with support from the Indo-US Science and Technology Forum (IUSSTF) and the Science and Engineering Research Board (SERB) of the Department of Science and Technology (DST), Government of India (<https://sites.google.com/view/growthindia/>).

It is located at the Indian Astronomical Observatory (Hanle), operated by the Indian Institute of Astrophysics (IIA). The GROWTH-India project is supported by SERB and administered by IUSSTF under grant No. IUSSTF/PIRE Program/GROWTH/2015-16. This research has made use of the VizieR catalog access tool, CDS, Strasbourg, France (doi: [10.26093/cds/vizier](https://cds.u-strasbg.fr/vizier/)). The original description of the VizieR service was published in A&AS 143, 23. These results made use of the Lowell Discovery Telescope (LDT) at Lowell Observatory. Lowell is a private, nonprofit institution dedicated to astrophysical research and public appreciation of astronomy and operates the LDT in partnership with Boston University, the University of Maryland, the University of Toledo, Northern Arizona University, and Yale University. The Large Monolithic Imager was built by Lowell Observatory using funds provided by the National Science Foundation (AST-1005313). The upgrade of the DeVeney optical spectrograph has been funded by a generous grant from John and Ginger Giovale and a grant from the Mt. Cuba Astronomical Foundation. The KPED team thanks the National Science Foundation and the National Optical Astronomical Observatory for making the Kitt Peak 2.1 m telescope available. We thank the observatory staff at Kitt Peak for their efforts to assist Robo-AO KP operations. The KPED team thanks the National Science Foundation, the National Optical Astronomical Observatory, the Caltech Space Innovation Council, and the Murty family for support in the building and operation of KPED. In addition, they thank the CHIMERA project for use of the Electron Multiplying CCD (EMCCD). The Liverpool Telescope is operated on the island of La Palma by Liverpool John Moores University in the Spanish Observatorio del Roque de los Muchachos of the Instituto de Astrofísica de Canarias with financial support from the UK Science and Technology Facilities Council. Some spectroscopic observations were obtained with the Southern African Large Telescope (SALT). The Photometric Redshifts for the Legacy Surveys (PRLS) catalog used in this paper was produced thanks to funding from the U.S. Department of Energy Office of Science, Office of High Energy Physics, via grant DE-SC0007914. This publication has made use of data collected at Lulin Observatory, partly supported by MoST grant 108-2112-M-008-001. Based on observations made with the Gran Telescopio Canarias (GTC), installed at the Spanish Observatorio del Roque de los Muchachos of the Instituto de Astrofísica de Canarias on the island of La Palma.

M.M.K. acknowledges generous support from the David and Lucille Packard Foundation. M.W.C. acknowledges support from the National Science Foundation with grant No. PHY-2010970. A.G. and J.S. acknowledge support from the Knut and Alice Wallenberg Foundation and GREAT research environment grant 2016-06012, funded by the Swedish Research Council. Some of the work by D.A.P. was performed at the Aspen Center for Physics, which is supported by National Science Foundation grant PHY-1607611. D.A.P. was partially supported by a grant from the Simons Foundation. H.K. thanks the LSSTC Data Science Fellowship Program, which is funded by LSSTC, NSF Cybertraining Grant 1829740, the Brinson Foundation, and the Moore Foundation; his participation in the program has benefited this work. This work has been supported by the Spanish Science Ministry Centro de Excelencia Severo Ochoa Program under grant SEV-2017-0709. A.J.C.T. acknowledges support from the Junta de Andalucía (Project P07-TIC-03094) and Spanish Ministry Projects AYA2012-39727-C03-01, AYA2015-71718R,

and PID2019-109974RB-I00. V.A.F. was supported by grant RFBR 19-02-00432. I.A. acknowledges support by a Ramón y Cajal grant (RYC-2013-14511) of the Ministerio de Ciencia, Innovación, y Universidades (MICIU) of Spain. He also acknowledges financial support from MICIU through grant AYA2016-80889-P. A.A.M. is funded by the Large Synoptic Survey Telescope Corporation, the Brinson Foundation, and the Moore Foundation in support of the LSSTC Data Science Fellowship Program; he also receives support as a CIERA Fellow by the CIERA Postdoctoral Fellowship Program (Center for Interdisciplinary Exploration and Research in Astrophysics, Northwestern University). A.C. acknowledges support from the National Science Foundation with grant No. 1907975. W.-H.L., A. K., K.-L.L., C.-C.N., A.P., H.T., and P.-C.Y. acknowledge support from Ministry of Science and Technology (MoST) Taiwan grants 104-2923-M-008-004-MY5, 107-2119-M-008-012, 108-2628-M-007-005-RSP, and 108-2112-M-007-025-MY3. D.D. is supported by an Australian Government Research Training Program Scholarship. S.A. is supported by the GROWTH project, funded by the National Science Foundation under PIRE grant No. 1545949. A.S.C. is supported by GREAT research environment grant 2016-06012, funded by the Swedish Research Council. E.C.K. acknowledges support from the G.R.E. A.T. research environment and the Wenner-Gren Foundations. A. J.C.T. is thankful for fruitful discussions with J. Cepa, E. Fernández-García, J. A. Font, S. Jeong, A. Martín-Carrillo, A. M. Sintes, and S. Sokolov. D.A.H.B. acknowledges research support from the National Research Foundation of South Africa. S.B.P. and V.B. acknowledge BRICS grant No. “DST/IMRCD/BRICS/PilotCall1/ProfCheap/2017(G)” for part of the present work. J.S.B. was partially supported by a Gordon and Betty Moore Foundation Data-Driven Discovery grant and a grant from the National Science Foundation, “Conceptualization of a Scalable Cyberinfrastructure Center for Multimessenger Astrophysics.”

Appendix A Observing and Data Reduction Details for Follow-up Observations

A.1. Photometric Follow-up

We used the 1 and 2 m telescopes available at the LCO global network to follow up sources discovered with the ZTF. The images were taken with the Sinistro and Spectral cameras (Brown et al. 2013) at the 1 and 2 m, respectively, and scheduled through the LCO Observation Portal.⁷⁶ The exposure time varied depending on the brightness of the object, yet our requests would normally involve three sets of 300 s in the *g* and *r* bands. After stacking the reduced images, we extracted sources using the SExtractor package (Bertin & Arnouts 2010), and we calibrated magnitudes against PS1 (Chambers et al. 2016) objects in the vicinity. For nuclear transients located $<8''$ from their potential host, we use the High Order Transform of Psf AND Template Subtraction code (HOTPANTS; Becker 2015) to subtract a PSF-scaled PS1 template previously aligned using SCAMP (Bertin 2006). The photometry for the nuclear candidates follows the same procedure described before but in the residual image. The images obtained with the LT were acquired using the IO:O camera with the Sloan *griz* filter set. They were reduced using the automated pipeline, which performs bias subtraction,

⁷⁶ <https://observe.lco.global/>

trimming of the overscan regions, and flat-fielding. The image subtraction takes place once a PS1 template is aligned, and the final data come from the analysis of the subtracted image.

We used the Electronic Multiplier CCD camera at KPED to take hour-long exposures in the r band to follow up candidates. After stacking the images and following standard reduction techniques, we calibrate the extracted sources using PS1 sources in the field. When the candidate has a host galaxy, we perform image subtraction as described for the LCO.

We obtained data with the GMOS-N (Allington-Smith et al. 2002; Hook et al. 2004; Gimeno et al. 2016), mounted on the Gemini-North 8 m telescope on Maunakea. Data were analyzed after stacking four 200 s exposures in the g and i bands. The reductions were performed using the python package DRAGON⁷⁷ provided by the Gemini Observatory. We used PS1 sources in the field to calibrate the data.

We used the LOT at the Lulin Observatory in Taiwan to follow up candidates discovered with the ZTF. The standard observations involved 240 s in the g' , r' , and i' bands. The reduction followed standard methods, and the sources were calibrated against the PS1 catalog. No further image subtraction was applied to the images acquired with the LOT.

We used the 0.7 m robotic GIT equipped with a 4096×4108 pixel back-illuminated Andor camera for LVC event follow-up during O3. The GIT is situated at the IAO (Hanle, Ladakh). We used both tiled and targeted modes for the follow-up for different GW triggers. Tiled observations typically comprise a series of 600 s exposures in the Sloan Digital Sky Survey (SDSS) r' filter. Targeted observations were conducted with varying exposure times in the SDSS u' , g' , r' , and i' filters. All data were downloaded in real time and processed with the automated GIT pipeline. Zero-points for photometry were calculated using the PanSTARRS catalog (Flewelling 2018), downloaded from Vizier. The PSF photometry was performed with PSFEX (Bertin 2011). For sources with significant host background, we performed image subtraction with `pyzogy` (Guevel & Hosseinzadeh 2017), based on the ZOGY algorithm (Zackay et al. 2016).

Additionally, we obtained photometric data with the Spectral Energy Distribution Machine (SEDm; Blagorodnova et al. 2018; Rigault et al. 2019) on the P60 telescope. The processing is automated and can be triggered from the GROWTH Marshal. Standard requests involved g -, r -, and i -band imaging with the Rainbow Camera on the SEDm in 300 s exposures. The data are later reduced using a python-based pipeline that applies standard reduction techniques and a customized version of the Fremling Automated Pipeline (FPipe; Fremling et al. 2016) for image subtraction.

We used the imaging capabilities of the OSIRIS (Cepa et al. 2005) camera at the GTC to obtain 60 s exposures in the r band. Standard reduction techniques were applied to the data, and we used PS1 sources to calibrate the flux.

We obtained follow-up imaging of candidates with the Wafer Scale Imager for Prime (WASP) and the Wide-field Infrared Camera (WIRC; Wilson et al. 2003), both on the P200 telescope. For WASP data, a python-based pipeline applied standard optical reduction techniques (as described in De et al. 2020a), and the photometric calibration was obtained against PS1 sources in the field. The WIRC data were treated similarly using the same pipeline, but they were additionally stacked

using Swarp (Bertin et al. 2002), while the calibration was done using the Two Micron All Sky Survey point-source catalog (Skrutskie et al. 2006).

We obtained imaging of one candidate using the Low Resolution Imaging Spectrometer (LRIS; Oke et al. 1995), mounted at the Keck I telescope. Our data were taken in the g and i bands reaching $m_{AB} \approx 24$. The data were reduced following standard methods.

We used the Large Monolithic Imager (LMI; Massey et al. 2013) on the 4.3 m LDT at Happy Jack, Arizona, to follow up the ZTF discoveries. Observations were conducted with the SDSS r filter for 90 s each, and the data were reduced using the photpipe⁷⁸ pipeline. The magnitudes were calibrated against the SDSS or Gaia catalogs (Ahumada et al. 2020) using the conversion scheme provided in Gaia documentation.⁷⁹

We used the Ultraviolet/Optical Telescope (UVOT; Roming et al. 2005) mounted on the Neil Gehrels Swift Observatory (hereafter referred to as Swift; Gehrels et al. 2004) to follow up interesting sources and track down their UV evolution. The ToO observations were scheduled in the v , b , u , $w1$, $m2$, and $w2$ bands for an average of 320 s exposure⁻¹. We used the products of the Swift pipeline to determine the magnitudes.⁸⁰

We observed candidate counterparts of S200213t using the Astrophysical Research Consortium Telescope Imaging Camera (ARCTIC; Huehnerhoff et al. 2016) at the APO 3.5 m. We obtained dithered 120 s exposures binned 2×2 in the u , g , r , i , and z bands. Images were bias-corrected, flat-fielded, and combined using standard IRAF packages (`noao`, `imred`, and `ccdred`). SExtractor (Bertin & Arnouts 2010) was used to find and photometer point sources in the images using PSF photometry, and a photometric calibration to PanSTARRS field stars was performed (without filter corrections).

All photometry presented in the light curves and tables in this paper is corrected for galactic extinction using dust maps from Schlafly & Finkbeiner (2011).

We observed the field of ZTF19aassfws with the VLA in its B configuration on 2019 May 10 starting at 07:19:15 UT and 2019 June 4 starting at 08:20:32 UT. Our observations were carried out at a nominal central frequency of 3 GHz. We used 3C 286 as our bandpass and absolute flux calibrator and J1927+6117 as our complex gain calibrator. Data were calibrated using the standard VLA automated calibration pipeline available in the Common Astronomy Software Applications (CASA) package. We then inspected the data for further flagging and imaged interactively using the CLEAN algorithm. The image rms was $\approx 5.2 \mu\text{Jy}$ for the first epoch and $\approx 4.6 \mu\text{Jy}$ for the second epoch. Within a circular region centered on the optical position of ZTF19aassfws and of radius $\approx 2''$ (comparable to the nominal half-power beamwidth of the VLA at 3 GHz and for the B configuration), we find no significant radio emission. Thus, we set upper limits on the corresponding 3 GHz flux density of $\lesssim 16$ and $\lesssim 14 \mu\text{Jy}$, respectively, for the first and second epochs.

A.2. Spectroscopic Follow-up

Using the GROWTH Marshal, we regularly triggered the Liverpool Telescope Spectrograph for the Rapid Acquisition of

⁷⁷ <https://dragons.readthedocs.io/en/stable/>

⁷⁸ <https://github.com/maxperry/photometrypipeline>

⁷⁹ https://gea.esac.esa.int/archive/documentation/GDR2/Data_processing/chap_cu5pho/sec_cu5pho_calibr/ssec_cu5pho_PhotTransf.html

⁸⁰ <https://swift.gsfc.nasa.gov/quicklook/>

Transients (SPRAT; Piascik et al. 2014). SPRAT uses a $1''.8$ slit, which provides a resolution of $R = 350$ at the center of the spectrum. The data were reduced using the automated pipeline, which removes low-level instrumental signatures and then performs source extraction, sky subtraction, and wavelength and flux calibration.

We observed a number of transient candidates during classical observing runs with the P200 Double Spectrograph (DBSP) during O3. For the setup configuration, we used $1''.0$, $1''.5$, and $2''.0$ slit masks; a D55 dichroic; a blue grating of 600/4000; and a red grating of 316/7500. Using a custom PyRAF DBSP reduction pipeline (Bellm & Sesar 2016),⁸¹ we reduced our data.

We obtained several optical spectra with the 10.4 m GTC telescope (equipped with OSIRIS). We used the R1000B and R500R gratings for our observations, typically using a slit of width of $1''.2$. We used standard routines from the Image Reduction and Analysis Facility (IRAF) to perform our data reduction.

We observed ZTF19aarykbb using the DeVeny spectrograph mounted on the 4.3 m LDT. We obtained 22.5 minute exposures at an average airmass of 1.5. We used the DV2 grating (300 g mm^{-1} , 4000 Å blaze) for this observation. Our spectra cover a wavelength range of approximately 3600–8000 Å.

In addition, we obtained a spectrum of ZTF20aarzaod with SALT (Buckley et al. 2003), using the Robert Stobie Spectrograph (RSS; Burgh et al. 2003), covering a wavelength range of 470–760 nm with a spectral resolution of $R = 400$. We triggered special GW follow-up program 2018-2-GWE-002 and reduced the data with a custom pipeline based on PyRAF routines and the PySALT package (Crawford et al. 2010).

Low-resolution spectra using the 2 m HCT were obtained using the HFOSC instrument; ZTF19aarykbb was observed using gratings Gr7 (3500–7800 Å) and Gr8 (5200–9000 Å), while AT2019wxt was observed using Gr7. The spectra were bias-subtracted, cosmic rays were removed, and the 1D spectra were extracted using the optimal extraction method. Wavelength calibration was effected using the arc lamp spectra FeAr (Gr7) and FeNe (Gr8). Instrumental response curves generated using spectrophotometric standards observed during the same night were used to calibrate the spectra onto a relative flux scale. The flux-calibrated spectra of ZTF19aarykbb from the two gratings were combined to a single spectrum covering the wavelength range 4000–9000 Å.

We obtained spectroscopy with the GMOS-N, mounted on the Gemini-North 8 m telescope on Maunakea, by combining six 450 s exposures on the R400 and B600 gratings. We used the GMOS long-slit capability and reduced the data following standard PyRAF techniques.

We obtained near-infrared spectroscopy of candidates using NIRES on the Keck II telescope. The data were acquired using standard ABBA dither patterns on the target source, followed by observations of an A0 telluric standard star close to the science target. The spectral traces were extracted using the `spextool` package (Cushing et al. 2004) for both the science target and standard star. The final spectra presented here were stacked from all individual dithers, followed by flux calibration and telluric correction using the `xtellcor` package (Vacca et al. 2003).

We obtained spectra using the LRIS on the Keck I telescope. The 600/4000 grism was used on the blue side and the 600/7500 grating on the red side, providing wavelength coverage between 3139–5642 Å (blue) and 6236–9516 Å (red). The exposure time was 600 s on both sides. The spectrum was reduced using LPipe (Perley 2019) with BD+28 as a flux calibrator. The red and blue relative fluxes are scaled by matching synthetic photometry to colors inferred from photometry of the transient.

Appendix B Detailed Candidate Descriptions

Here we provide descriptions of each candidate identified within the sky map of each event followed up with the ZTF. We discuss each object announced via GCN. For candidates with a redshift, we note whether it is spectroscopic [*s*] or photometric [*p*]. Some candidates were classified as a part of coordinated spectroscopic follow-up with the Bright Transient Survey (BTS; Fremling et al. 2020) and the ZTF CLU experiment (De et al. 2020b).

B.1. GW190425

For candidates identified within the sky map of GW190425, see Coughlin et al. (2019a). Two candidate counterparts of GW190425z, ZTF19aarykbb and ZTF19aarzaod, were observed with the AMI Large Array at 15 GHz on 2019 April 26 (Rhodes et al. 2019). No radio emission was found to be associated with any of these candidates.

B.2. S190426c

We summarize the candidate counterparts to S190426c in Table 2 and the follow-up photometry in Table 11. Next, we discuss why we conclude that each one is unrelated.

B.2.1. Spectroscopically Classified

ZTF19aasmftm/AT2019sne—The rising light curve of ZTF19aasmftm suggested that it could be a young and faint object with a galaxy host of $m_{\text{AB}} = 21.2$ mag in PS1, so we highlighted it in Perley et al. (2019a). A few days later, GTC spectroscopy of this event (Hu et al. 2019b) classified it as a premaximum SN Ia in the outskirts of its host galaxy at $z[s] = 0.156$.

ZTF19aaslzjff/AT2019snh—Another candidate discovered during our second night of observations, ZTF19aaslzjf, was at low galactic latitude and seemed to be located in a nearby host galaxy. A spectrum from GTC (Hu et al. 2019b) confirmed both that this source was nearby (at $z[s] = 0.086$) and that it was an SN Ia located in the outskirts of the Galaxy host.

ZTF19aasmddt/SN2019fht—We highlighted this transient because its photometric redshift was consistent with the LVC distance estimate, and the light curve exhibited a rapid rise (Perley et al. 2019a). However, the GTC spectrum taken shortly afterward revealed that this transient was a young SN II prepeak in the outskirts of its galaxy at $z[s] = 0.028$.

ZTF19aaslszp/AT2019anj—Another candidate whose photo-*z* was consistent with the LVC distance estimate, ZTF19aaslszp, appeared to be relatively bright and red with a color of $g - r = 0.89$ mag. Subsequent ZTF and LT photometry revealed that the source appeared to have flaring behavior in the light

⁸¹ <https://github.com/ebellm/pyraf-dbsp>

Table 11
Follow-up Photometry for S190426c Candidates

Name	IAU Name	Date	Telescope	Filter	m (AB)	σ_m	m_{lim}
ZTF19aasmftm	AT2019sne	2,458,602.6514	LT	g	21.33	0.15	21.71
ZTF19aasmftm	AT2019sne	2,458,602.6528	LT	r	21.06	0.10	21.51
ZTF19aasmftm	AT2019sne	2,458,602.6542	LT	i	20.90	0.17	21.03
ZTF19aassfws	AT2019fuc	2,458,603.6605	LT	g	99.0	99.0	22.32
ZTF19aassfws	AT2019fuc	2,458,603.6619	LT	r	99.0	99.0	22.04
ZTF19aassfws	AT2019fuc	2,458,603.6633	LT	i	99.0	99.0	21.50
ZTF19aaslszp	AT2019snj	2,458,603.6654	LT	g	20.80	0.07	22.25
ZTF19aaslszp	AT2019snj	2,458,603.6668	LT	r	20.51	0.07	22.12
ZTF19aaslszp	AT2019snj	2,458,603.6682	LT	i	19.19	0.06	22.00
ZTF19aaslzjf	AT2019snh	2,458,603.6703	LT	g	20.94	0.18	21.75
ZTF19aaslzjf	AT2019snh	2,458,603.6717	LT	r	20.40	0.10	22.00
ZTF19aaslzjf	AT2019snh	2,458,603.6731	LT	i	20.30	0.10	22.00
ZTF19aasmddt	SN2019fht	2,458,603.7113	LT	g	19.79	0.10	22.77
ZTF19aasmddt	SN2019fht	2,458,603.7127	LT	r	19.43	0.11	21.54
ZTF19aasmddt	SN2019fht	2,458,603.7141	LT	i	19.41	0.09	21.10
ZTF19aasmddt	SN2019fht	2,458,604.7237	LT	g	19.69	0.06	21.61
ZTF19aasmddt	SN2019fht	2,458,604.7251	LT	r	19.51	0.03	22.29
ZTF19aasmddt	SN2019fht	2,458,604.7265	LT	i	19.55	0.07	20.63

curve. Our P200+DBSP spectrum classified the source as an AGN at $z[s] = 0.084$, as it shows broad hydrogen lines.

B.2.2. Slow Photometric Evolution

ZTF19aaslszfk/AT2019snd—We identified this candidate during our initial search of the imaged region within the BAYESTAR localization of S190426c (Coughlin et al. 2019c). Though the candidate had WISE detections in all four filters, its WISE colors did not definitively place this transient in the AGN class. Continued photometric monitoring of this candidate revealed its slow evolution ($\alpha_g = -0.02$), ruling out its association with S190426c.

ZTF19aaslwn/AT2019snf—We reported ZTF19aaslwn in Perley et al. (2019a) as a lower-priority transient, with initially slow photometric evolution at low galactic latitude ($b < 15^\circ$). After monitoring the transient over a period of ~ 12 days, the photometry had only risen by 0.4 mag, indicating that it could not be a kilonova and was likely a CV.

ZTF19aasmddt/AT2019sng—Also reported in Perley et al. (2019a), ZTF19aasmddt was a nuclear transient at a low galactic latitude, with WISE colors consistent with an AGN within $1''$ of the transient. Several days of monitoring yielded a light curve that was far more consistent with a flaring AGN than a kilonova, with a rate of evolution $\alpha_r < 0.01$.

ZTF19aaslof/AT2019snn—This nuclear candidate was a low priority in our follow-up list due to its high photometric redshift ($z[p] = 0.42$) and because its WISE colors placed it within the AGN locus. Though we could not spectroscopically confirm this, the slowly evolving “flaring” light curve ($\alpha_r < 0.01$) and archival PS1 detections point to the AGN nature of this candidate.

ZTF19aaslphi/AT2019sno—The candidate ZTF19aaslphi had a photometric redshift that was also nominally inconsistent with the LVC distance. However, we identified it as a candidate of interest due to its relatively quick rise of ~ 0.75 mag over the course of 4 days in the g band. Its later-time light curve exhibited a plateau; thus, we consider its evolution too slow to be associated with a GW event.

ZTF19aaslpds/AT2019snq—This candidate, at low galactic latitudes, had multiple detections in the r and g filters; but, as it only evolved by 0.04 mag over a day of monitoring and subsequently was not detected, we ruled it out as a potential counterpart to S190426c.

ZTF19aaslozu/AT2019snr—We included this candidate initially due to its rapid rise and $g - r$ color of 0.3 mag (Perley et al. 2019a). Though ZTF19aaslozu did not clearly fall into the AGN locus, its detections in all four WISE filters, archival detections with PS1, and slow evolution point to it being a strong AGN candidate.

ZTF19aasshpf/AT2019snt—This is a lower-priority candidate on our list discovered at $r = 21.59$ mag in the outskirts of a faint red galaxy. It exhibited a flat evolution (0.06 mag) over a period of 27 days, thus ruling out its association with S190426c.

ZTF19aasmzqf—We could likewise rule out the possibility of ZTF19aasmzqf being a kilonova due to its slow evolution of 0.3 mag over 28 days, despite its initial red color $g - r = 0.22$ mag.

B.2.3. Stellar

ZTF19aasmekb/AT2019sni—Located at low galactic latitude ($b = -8^\circ.64$), ZTF19aasmekb appeared to be hostless and initially exhibited a rapid fade; its later-time light curve is photometrically consistent with a CV, and its slow evolution ($\alpha_g = 0.24$) is inconsistent with a kilonova origin.

B.2.4. Artifacts

ZTF19aassfws/AT2019fuc—We highlighted ZTF19aassfws as a candidate of potential interest because its photometric redshift fell within the LIGO distance uncertainty (Perley et al. 2019a). We also obtained radio follow-up using the VLA and AMI under the Jansky VLA mapping of Gravitational Waves as Afterglows in Radio (JAGWAR; Mooley et al. 2018), and we did not detect any radio emission. However, upon careful inspection of the reference image, we identified a very subtle gain mismatch across the image. Comparing the initial

photometry of the transient with the level of the gain mismatch provided a clear indication that our candidate was not astrophysical but rather an artifact. This gain mismatch problem has since been fixed by rebuilding the references.

B.3. GW190814

No candidates were identified in the ZTF follow-up of the small localization of GW190814.

B.4. S190901ap

We summarize the candidate counterparts to S190901ap in Table 3 and the follow-up photometry in Table 12. Next, we discuss why we conclude that each one is unrelated.

B.4.1. Spectroscopically Classified

ZTF19abvizsw/AT2019pim—We discovered a red transient ($g - r \approx 0.5$) that appeared to be hostless and fast-evolving. We had observed the location of this transient every night for the month leading up to 2019 September 1 with no previous detections, therefore indicating strongly that this object was a new transient. Gravitational Wave Inaf Team Collaboration (GRAWITA) spectroscopic observations about 10 hr later seemed to suggest that the object was a galactic K or M dwarf (Salsamo et al. 2019a), but our subsequent LRIS spectroscopic follow-up yielded a featureless continuum with Mg II, Mg I, and Fe II lines at $z[s] = 1.26$ (Burdge et al. 2019). Thus, we posited that the object could be a flaring AGN or a GRB afterglow. Observations with SVOM-GWAC-F60A (Wei et al. 2019) and the LT (Perley et al. 2019b) indicated that the light curve was rapidly decaying, suggesting that the transient was likely an orphan GRB afterglow. More than 10 other GCNs contained reported follow-ups of this transient; the collated evidence posed the coherent picture that we had, remarkably, detected an untriggered long GRB afterglow in temporal and spatial coincidence with the sky map of S190901ap. This candidate will be discussed in more detail in D. A. Perley et al. (2020, in preparation).

ZTF19abvixoy/AT2019pin—We detected this transient with an upper limit from the day before the merger, though it appeared to have a faint counterpart in PS1. GRAWITA spectroscopic observations classified this transient as a CV due to its blue continuum and weak $H\alpha$ emission surrounded by broad absorption troughs (Salsamo et al. 2019b).

ZTF19abvionh/AT2019pip—The photometric redshift of the putative host of this transient initially made it an interesting candidate for association with S190901ap, even though its first two detections were separated by a short baseline of 7 minutes. About 15 hr later, spectroscopic observations with the Hobby-Eberly observatory suggested that the host galaxy GALEXASC J165500.03+140301.3 was located at a distance of ~ 450 Mpc (Rosell et al. 2019); our LRIS spectrum, showing a hot blue continuum and host galaxy lines at $z[s] = 0.0985$, confirmed this conclusion, placing the transient outside of the GW distance error bar by 2.5σ . Upon close inspection of the spectra, we find $H\alpha$ and He II at zero redshift, suggesting that the transient is a foreground CV and the background host galaxy is unrelated.

ZTF19abwvals/AT2019pni—Another transient detected via the AMPEL alert archive, ZTF19abwvals, appeared to be red ($g - r \sim 0.5$) and had a photometric redshift of 0.13, slightly higher than the GW distance, also with upper limits in the g

band the previous day (Stein et al. 2019c). The SNID template matching to the spectra taken with the ALFOSC spectrograph on the Nordic Optical Telescope revealed that ZTF19abwvals was a normal SN Ia, about 4–6 days postpeak (Izzo et al. 2019).

B.4.2. Slow Photometric Evolution

ZTF19abwsmmd/AT2019pnc—Further searches of the data with the AMPEL pipeline yielded two additional candidates, including ZTF19abwsmmd (Stein et al. 2019c). This candidate exhibited a blue color ($g - r \sim 0.25$) and had nondetections in the g band to 20.64 mag a day before the merger. The ZTF survey operations monitored it over a period of about 35 days. The light curve exhibited a change of only 0.2 mag decline over that baseline; therefore, we deemed it too slow to be associated with the GW event.

ZTF19abvislp/AT2019pnx—We performed a second search of the AMPEL alert archive in which we identified this transient, detected on the first night of observations. It was interesting due to its rising light curve and host SDSS galaxy being at a redshift of 0.1, on the upper end of the LIGO distance range. Instead of using our spectroscopic resources, we chose to monitor the transient photometrically, and its evolution over nearly 30 days proved to be too slow ($\alpha_r = 0.05$) to be a kilonova.

ZTF19abxdvcs/AT2019qev—We also discovered ZTF19abxdvcs during a second AMPEL archive search and highlighted it due to its photometric redshift ($z \sim 0.118$) and the fact that it had risen by more than 0.65 mag over the course of 3 days, with its first detection on the first night. Though we did not report this candidate via GCN, our continued photometric monitoring with the ZTF demonstrated that the transient was evolving with $\alpha_g = 0.03$, and its light curve resembled that of an SN, so we could confidently reject it.

B.5. S190910d

We summarize the candidate counterparts to S190910d in Table 4 and the follow-up photometry in Table 13. Next, we discuss why we conclude that each one is unrelated.

B.5.1. Spectroscopically Classified

ZTF19abyfhov/AT2019pvu—We identified this candidate during our follow-up campaign for S190910d with no available photometric redshifts due to cross-matches at its sky position (Anand et al. 2019). Castro-Tirado et al. (2019b) observed it with the 10.4 m GTC telescope equipped with OSIRIS in La Palma, Spain, about 16 hr after initial detection and derived an r -band magnitude of 20.33 mag for the transient. The best match to their spectrum indicated that the candidate was an SN Ia at $z[s] = 0.133 \pm 0.001$. Another spectrum taken with the ACAM instrument on the William Herschel Telescope at the Roque de los Muchachos Observatory in La Palma confirmed the classification (Cannizzaro et al. 2019).

ZTF19abyfhaq/AT2019pvv—Similarly, we detected ZTF19abyfhaq with little other information than the r -band magnitude of its initial detection at 20.3 mag (Anand et al. 2019). The GTC spectrum taken (Castro-Tirado et al. 2019b) about 18 hr after the initial detection had a too-low S/N to merit a classification, but an $H\alpha$ emission line at $z[s] = 0$ revealed that the transient was galactic and therefore unrelated.

Table 12
Follow-up Photometry for S190901ap Candidates

Name	IAU Name	Date	Telescope	Filter	m (AB)	σ_m	m_{lim}
ZTF19abvizsw	AT2019pim	2,458,729.229	GIT	<i>i</i>	20.14	0.1	20.41
ZTF19abvizsw	AT2019pim	2,458,729.126	GIT	<i>i</i>	20.13	0.09	20.41
ZTF19abvizsw	AT2019pim	2,458,729.303	GIT	<i>g</i>	21.19	0.06	21.43
ZTF19abvizsw	AT2019pim	2,458,729.103	GIT	<i>r</i>	20.57	0.11	20.65
ZTF19abvizsw	AT2019pim	2,458,730.4481	LT	<i>g</i>	22.02	0.10	22.00
ZTF19abvizsw	AT2019pim	2,458,730.4420	LT	<i>r</i>	21.62	0.09	22.0
ZTF19abvizsw	AT2019pim	2,458,730.4541	LT	<i>i</i>	21.16	0.07	22.00
ZTF19abvizsw	AT2019pim	2,458,730.4621	LT	<i>z</i>	20.87	0.12	22.00
ZTF19abvizsw	AT2019pim	2,458,731.14	GIT	<i>i</i>	99.0	99.0	20.29
ZTF19abvizsw	AT2019pim	2,458,731.134	GIT	<i>i</i>	99.0	99.0	20.29
ZTF19abvizsw	AT2019pim	2,458,731.118	GIT	<i>r</i>	99.0	99.0	20.98
ZTF19abvizsw	AT2019pim	2,458,731.125	GIT	<i>r</i>	99.0	99.0	21.14
ZTF19abvizsw	AT2019pim	2,458,731.3862	LT	<i>g</i>	22.50	0.20	22.50
ZTF19abvizsw	AT2019pim	2,458,731.3802	LT	<i>r</i>	22.05	0.10	22.50
ZTF19abvizsw	AT2019pim	2,458,731.3923	LT	<i>i</i>	21.60	0.10	22.50
ZTF19abvizsw	AT2019pim	2,458,731.3983	LT	<i>z</i>	21.20	0.20	22.50
ZTF19abvizsw	AT2019pim	2,458,731.5172	LT	<i>g</i>	22.54	0.16	23.00
ZTF19abvizsw	AT2019pim	2,458,731.5112	LT	<i>r</i>	22.10	0.12	23.00
ZTF19abvizsw	AT2019pim	2,458,731.5232	LT	<i>i</i>	21.64	0.11	23.00
ZTF19abvizsw	AT2019pim	2,458,731.5293	LT	<i>z</i>	21.55	0.22	23.00
ZTF19abvizsw	AT2019pim	2,458,732.102	GIT	<i>r</i>	99.0	99.0	19.32
ZTF19abvizsw	AT2019pim	2,458,732.119	GIT	<i>i</i>	99.0	99.0	20.4
ZTF19abvizsw	AT2019pim	2,458,732.125	GIT	<i>i</i>	99.0	99.0	20.43
ZTF19abvizsw	AT2019pim	2,458,738.3819	WHT	<i>r</i>	22.60	0.12	24.00
ZTF19abvizsw	AT2019pim	2,458,739.3839	WHT	<i>i</i>	22.43	0.12	24.10
ZTF19abvizsw	AT2019pim	2,458,740.4939	WHT	<i>i</i>	22.51	0.15	23.50
ZTF19abvizsw	AT2019pim	2,458,740.5219	WHT	<i>r</i>	23.38	0.25	23.70
ZTF19abvizsw	AT2019pim	2,458,750.7337	Keck1	<i>g</i>	23.99	0.10	26.00
ZTF19abvizsw	AT2019pim	2,458,750.7342	Keck1	<i>i</i>	23.80	0.09	25.00
ZTF19abvionh	AT2019pip	2,458,729.166	GIT	<i>r</i>	20.8	0.05	21.27
ZTF19abvionh	AT2019pip	2,458,729.206	GIT	<i>r</i>	20.77	0.06	21.17
ZTF19abvionh	AT2019pip	2,458,729.213	GIT	<i>r</i>	20.68	0.08	21.15
ZTF19abvionh	AT2019pip	2,458,730.166	GIT	<i>r</i>	20.63	0.04	21.22
ZTF19abvionh	AT2019pip	2,458,730.18	GIT	<i>r</i>	20.66	0.05	21.23
ZTF19abvionh	AT2019pip	2,458,731.204	GIT	<i>g</i>	20.56	0.06	21.16
ZTF19abvionh	AT2019pip	2,458,731.4331	LT	<i>u</i>	20.47	0.11	21.86
ZTF19abvionh	AT2019pip	2,458,731.4208	LT	<i>g</i>	20.51	0.29	22.55
ZTF19abvionh	AT2019pip	2,458,731.4168	LT	<i>r</i>	20.36	0.09	22.35
ZTF19abwsmmd	AT2019pnc	2,458,731.5587	LT	<i>g</i>	19.86	0.16	20.41
ZTF19abwsmmd	AT2019pnc	2,458,731.5641	LT	<i>r</i>	20.02	0.07	22.02
ZTF19abwsmmd	AT2019pnc	2,458,731.5614	LT	<i>i</i>	20.26	0.06	22.47
ZTF19abwvals	AT2019pni	2,458,731.7095	LT	<i>g</i>	20.42	0.07	22.63
ZTF19abwvals	AT2019pni	2,458,731.7149	LT	<i>r</i>	20.04	0.08	22.96
ZTF19abwvals	AT2019pni	2,458,731.7122	LT	<i>i</i>	20.23	0.24	22.30
ZTF19abvixoy	AT2019pin	2,458,729.144	GIT	<i>r</i>	18.97	0.03	21.16
ZTF19abvixoy	AT2019pin	2,458,729.182	GIT	<i>r</i>	18.73	0.02	21.17
ZTF19abvixoy	AT2019pin	2,458,729.238	GIT	<i>i</i>	18.97	0.05	20.35
ZTF19abvixoy	AT2019pin	2,458,729.245	GIT	<i>i</i>	19.06	0.05	20.38
ZTF19abvixoy	AT2019pin	2,458,729.285	GIT	<i>i</i>	19.02	0.1	20.27
ZTF19abvixoy	AT2019pin	2,458,729.292	GIT	<i>i</i>	18.94	0.1	20.23
ZTF19abvislp	AT2019pnx	2,458,734.171	GIT	<i>g</i>	99.0	99.0	20.42
ZTF19abvislp	AT2019pnx	2,458,734.178	GIT	<i>g</i>	99.0	99.0	20.29
ZTF19abvislp	AT2019pnx	2,458,735.113	GIT	<i>g</i>	99.0	99.0	20.34
ZTF19abvislp	AT2019pnx	2,458,735.181	GIT	<i>r</i>	99.0	99.0	19.91
ZTF19abvislp	AT2019pnx	2,458,733.111	GIT	<i>g</i>	99.0	99.0	20.45
ZTF19abvislp	AT2019pnx	2,458,733.118	GIT	<i>g</i>	99.0	99.0	20.36
ZTF19abvislp	AT2019pnx	2,458,735.174	GIT	<i>r</i>	99.0	99.0	19.89
ZTF19abxdvcs	AT2019qev	2,458,733.133	GIT	<i>g</i>	19.93	0.03	20.7
ZTF19abxdvcs	AT2019qev	2,458,733.173	GIT	<i>r</i>	20.18	0.05	20.72
ZTF19abxdvcs	AT2019qev	2,458,733.179	GIT	<i>r</i>	20.28	0.03	20.82

Table 12
(Continued)

Name	IAU Name	Date	Telescope	Filter	m (AB)	σ_m	m_{lim}
ZTF19abxdvcs	AT2019qev	2,458,734.242	GIT	g	19.83	0.03	20.55
ZTF19abxdvcs	AT2019qev	2,458,734.249	GIT	g	19.9	0.05	20.38
ZTF19abxdvcs	AT2019qev	2,458,734.258	GIT	r	20.03	0.05	20.31
ZTF19abxdvcs	AT2019qev	2,458,734.264	GIT	r	20.11	0.05	20.32
ZTF19abxdvcs	AT2019qev	2,458,735.206	GIT	r	19.8	0.05	19.94
ZTF19abxdvcs	AT2019qev	2,458,735.213	GIT	r	19.84	0.05	19.89

Table 13
Follow-up Photometry for S190910d Candidates

Name	IAU Name	Date	Telescope	Filter	m (AB)	σ_m	m_{lim}
ZTF19abyfazm	AT2019pwa	2,458,736.8848	P60	r	18.17	0.04	20.48
ZTF19abyfazm	AT2019pwa	2,458,737.3704	LT	g	17.95	0.03	21.00
ZTF19abyfazm	AT2019pwa	2,458,737.3704	LT	g	17.96	0.01	21.81
ZTF19abyfazm	AT2019pwa	2,458,737.3715	LT	r	18.30	0.03	21.00
ZTF19abyfazm	AT2019pwa	2,458,737.3715	LT	r	18.30	0.01	22.36
ZTF19abyfazm	AT2019pwa	2,458,737.3725	LT	i	18.65	0.05	21.00
ZTF19abyfazm	AT2019pwa	2,458,737.3725	LT	i	18.62	0.01	22.16

ZTF19abyfazm/AT2019pvz—Among the other candidates identified in Anand et al. (2019), we highlighted this one as being blue ($g - r \sim 0.4$), with its last nondetection 1 day before the merger, and a faint source in PS1 about $2''5$ from the transient position. Our imaging and spectroscopy with the LT showed that the transient remained bright and blue, with no obvious emission or absorption lines in the spectrum, suggesting that this was likely a CV (Perley & Copperwheat 2019a); this conclusion was further supported by a GTC spectrum (Castro-Tirado et al. 2019b).

ZTF19abyfbii/AT2019pwa—During the same initial search, we identified ZTF19abyfbii, whose proximity to an SDSS galaxy with a photometric redshift of $z[p] = 0.124$ placed it within the distance uncertainty for S190910d (Anand et al. 2019). Our candidate was classified as an SN Ia at $z[s] = 0.1286 \pm 0.0005$ less than 20 hr later by GTC using the $H\alpha$, $H\beta$, and $O\text{ II}$ lines in its spectrum (Castro-Tirado et al. 2019b). Further spectroscopy with the William Herschel Telescope provided a detailed classification that this transient was SN Ia 91T-like, 5 days before the peak, at $z[s] = 0.118$ (Cannizzaro et al. 2019).

B.6. S190910h

We summarize the candidate counterparts to S190910h in Table 5 and the follow-up photometry in Table 14. Next, we discuss why we conclude that each one is unrelated.

B.6.1. Spectroscopically Classified

ZTF19abyheza/AT2019pxi—We initially detected ZTF19abyheza at $g = 19.14 \pm 0.13$ with the ZTF with heavy galactic extinction of ~ 0.8 in the direction of the transient. One day later, Valeev et al. (2019) imaged the transient, reporting that it had brightened to $r = 18.74 \pm 0.05$. The GTC spectroscopy revealed $H\alpha$ in emission and $H\beta$ in absorption at $z[s] = 0$. Synthesizing this information along with the light-curve shape suggested that this was likely a CV.

ZTF19abyhhml/AT2019pxj—According to our machine-learning algorithms derived from the PS1-DR2 catalog, we could not clearly determine whether this source was of stellar

origin. Similar to the previous transient, GTC imaging demonstrated that the light curve had risen to $r = 19.26 \pm 0.04$, and spectra exhibited the He II and He I lines and a double-peaked $H\alpha$ line, confirming that it was also a galactic CV.

ZTF19abyirjl/AT2019pxe—We highlighted ZTF19abyirjl as being of interest due to its photometric redshift, 0.1 ± 0.017 . Having no other information about the transient, we monitored the light curve for several days and determined it was too slow to be associated with the GW event, with an average flat evolution. One month later, we obtained a spectrum using P200 +DBSP, which clearly demonstrated through Si II lines that it was an SN Ia.

ZTF19abygvmp/AT2019pzg—This candidate was among those candidates reported in our second set of transients (Stein et al. 2019a). We highlighted ZTF19abygvmp, a transient detected 1 hr after the merger time, in a slightly offset position from the galaxy, as it had appeared to have risen by 0.5 mag since the last nondetection. Cannizzaro et al. acquired a WHT spectrum of the source about 2 days later, but the spectrum, dominated by host galaxy light, yielded only a redshift of $z[s] = 0.049$, exactly consistent with the LVC distance estimate. Two weeks later, we obtained an LRIS spectrum of the source, classifying it as an SN II (also consistent with its slow photometric evolution).

B.6.2. Slow Photometric Evolution

ZTF19abylleu/AT2019pyu—23 hr after the merger, we detected this bright ($r = 19.25$ mag) transient with an upper limit of $r = 20.4$ mag from the day before. Though we could not obtain any spectra, we continued tracking the evolution of the transient over a period of ~ 25 days; the r -band light curve remained relatively flat, while the g -band light curve exhibited a gradual decline. We concluded that the evolution was too slow ($\alpha_g = 0.03$) to be associated with the GW event.

ZTF19abyjfiw—Valeev et al. (2019) obtained a spectrum with GTC about 2 days later that appeared to be a featureless blue continuum from which they could not derive a conclusive

Table 14
Follow-up Photometry for S190910h Candidates

Name	IAU Name	Date	Telescope	Filter	m (AB)	σ_m	m_{lim}
ZTF19abjcom	AT2019pxk	2,458,737.5558	LT	g	99.0	99.0	20.75
ZTF19abjcom	AT2019pxk	2,458,737.5569	LT	r	99.0	99.0	20.71
ZTF19abjcom	AT2019pxk	2,458,737.5579	LT	i	99.0	99.0	20.21
ZTF19abjcon	AT2019pxl	2,458,737.6142	LT	g	99.0	99.0	21.29
ZTF19abjcon	AT2019pxl	2,458,737.6152	LT	r	99.0	99.0	21.44
ZTF19abjcon	AT2019pxl	2,458,737.6163	LT	i	99.0	99.0	21.33
ZTF19abjcoo	AT2019pxm	2,458,737.6234	LT	g	99.0	99.0	20.84
ZTF19abjcoo	AT2019pxm	2,458,737.6245	LT	r	99.0	99.0	20.89
ZTF19abjcoo	AT2019pxm	2,458,737.6255	LT	i	99.0	99.0	21.30

Table 15
Follow-up Photometry for S190930t Candidates

Name	IAU Name	Date	Telescope	Filter	m (AB)	σ_m	m_{lim}
ATLAS19wyn	AT2019rpj	2,458,758.0974	LOT	g	19.65	0.08	99.0
ATLAS19wyn	AT2019rpj	2,458,758.0974	LOT	r	19.58	0.09	99.0
ATLAS19wyn	AT2019rpj	2,458,758.0974	LOT	i	19.55	0.12	99.0
ATLAS19wyn	AT2019rpj	2,458,758.8562	LDT	r	19.6	0.1	22.8
ZTF19acbqqlh	AT2019rpn	2,458,758.0937	LOT	g	20.80	0.25	99.0
ZTF19acbqqlh	AT2019rpn	2,458,758.0937	LOT	r	20.67	0.33	99.0
ZTF19acbqqlh	AT2019rpn	2,458,758.0937	LOT	i	20.80	0.39	99.0
ZTF19acbqqlh	AT2019rpn	2,458,758.8548	LDT	r	19.80	0.10	22.8

classification. However, the transient presents a flat evolution, with a coefficient $\alpha < 0.1$. Another detection by the ZTF (4 months after merger) suggests that it could be a CV.

ZTF19abjiwiw/AT2019pzi—We identified this transient in spatial and temporal coincidence with both S190910d and S190910h at $3^\circ.1$ galactic latitude and 2.3 mag of extinction in the direction of the transient. It was first discovered at $r = 20.16$ mag, but photometric follow-up determined that its evolution was too slow to be relevant, with $\alpha_g = 0.20$.

ZTF19abymhyi/AT2019pzh—The object ZTF19abymhyi was faint and hostless, with detections in the g band 2 hr after the merger (Stein et al. 2019a) and upper limits of $g = 20.65$ mag from the day before. The transient rose by ~ 0.3 mag 1 day later. However, it was ruled out because its photometric evolution did not pass our threshold, as it faded slower than expected with $\alpha_g = 0.03$.

ZTF19abjcoo/AT2019pxm—This orphan transient was discovered at $r = 20.28$ mag, and we rule it out due to its slow evolution ($\alpha_r = 0.06$).

B.6.3. Artifacts

ZTF19abjcom/AT2019pxk, *ZTF19abjcon/AT2019pxl*—On the first night of observations following this GW event, we detected two hostless transients within the same exposure, detected within the same sky region. Imaging with the LT about 1 day later resulted in nondetections of both transients, despite the fact that other transients of a similar magnitude, discovered within the same exposure, were detected. Furthermore, despite clear detections initially in the r and g bands, we could not detect these transients in future serendipitous observations of the sky region with the ZTF. We posit that these three transients are likely cross-talk artifacts that occurred within the same exposure and therefore are unrelated.

B.7. S190923y

We summarize one candidate counterpart to S190923y in Table 6. Despite the small sky localization, the position of S190923y on the sky made it particularly challenging to access. For that reason, we chose to conduct a fully serendipitous search in ZTF data.

ZTF19acbmopl/AT2019rob—We found this transient with a photometric redshift of $\lesssim 0.03$, consistent with the LVC distance reported, slightly off the nucleus of its host galaxy. It showed a slow evolution in both the r and g bands: $\alpha_r = 0.03$ and $\alpha_g = 0.03$.

B.8. S190930t

We summarize the candidate counterparts to S190930t in Table 7 and the follow-up photometry in Table 15. Next, we discuss why we conclude that each one is unrelated.

B.8.1. Spectroscopically Classified

ZTF19acbqqlh/AT2019rpn—We first detected this candidate 13.4 hr after the merger using our AMPEL pipeline with a magnitude of $g = 20.36$ mag and upper limits of $g = 20.77$ mag from 3 days before the merger. The transient was at a galactic latitude of $b = -8^\circ.49$. Using its spectroscopic host galaxy redshift, $z[s] = 0.026$, we derived an absolute magnitude of -14.91 mag (Stein et al. 2019b). The same night, we obtained a spectrum with P200+DBSP revealing a mostly featureless blue continuum with a weak broad feature around $H\alpha$ suggesting that the transient could be a young core-collapse SN. Using the ZTSh 2.6 m telescope at the CrAO observatory, Mazaeva et al. (2019) imaged the SN and found that its $B - R$ color of 0.5 mag was unlike what was expected of any optical transient associated with a GW event.

Table 16
Follow-up Photometry for S191205ah Candidates

Name	IAU Name	Date	Telescope	Filter	m (AB)	σ_m	m_{lim}
ZTF19acxowrr	AT2019wib	2,458,850.0554	P60	r	18.91	0.16	99.0
ZTF19acxowrr	AT2019wib	2,458,852.7504	P60	i	99.0	99.0	20.00
ZTF19acyitga	AT2019wmn	2,458,837.8427	P60	r	18.21	0.07	99.0

We followed up by taking a second spectrum with the DBSP on 2019 October 5 and confirmed that the candidate was indeed an SN II.

ZTF19acbwaah/AT2019rpp—22 hr after the merger, we detected this transient, whose slight offset from a potential galaxy host at $z[s] = 0.032$ lends it an absolute magnitude of -18.069 (Stein et al. 2019b). The next night, we conducted observations of this candidate with the DBSP; the spectrum was consistent with an SN Ia a few weeks after maximum light located at $z[s] = 0.03$ (Karambelkar et al. 2019b).

ATLAS19wyn/AT2019rpj—With the ZTF, we independently detected a candidate first reported by ATLAS (Smartt et al. 2019; ZTF19acbpsuf) 13.8 hr after the merger; ATLAS detected it 4 hr later. The transient had a deep upper limit of 20.92 from about 6 days before the merger, and its association with a host at $z[s] = 0.0297$ translated to an absolute magnitude of -15.987 . The strong Balmer P Cygni features in our DBSP spectrum, taken the same night as the initial detection, clearly indicated that the transient was an SN (Karambelkar et al. 2019a).

B.9. S191205ah

We summarize the candidate counterparts to S191205ah in Table 8 and follow-up photometry in Table 16. Next, we discuss why we conclude that each one is unrelated.

B.9.1. Spectroscopically Classified

ZTF19acyifj/AT2019wmy—This transient was discovered at $r = 20.09$ mag and observed by GTC at a magnitude of $r = 19.79$ mag hours after the trigger. A faint host is visible in the PS1 images of the field. However, the GTC spectrum showed an SN Ia at a redshift of $z[s] = 0.081$ (Hu et al. 2019a).

ZTF19acxowrr/AT2019wib—The first detection of this transient was ~ 4 days after the GW event at $r = 19.054 \pm 0.13$ mag. It rose over the first ~ 15 days, during which several spectra were taken. The first classification came from GTC (Hu et al. 2019c): an SN II at a redshift of $z[s] = 0.05$.

ZTF19acyitga/AT2019wmn—This transient was located in a galaxy at a redshift of $z[s] = 0.071$ and first detected at $r = 19.26$ mag. We obtained an LT spectrum of ZTF19acyitga 14 days after the discovery that showed it was an SN Ia.

B.9.2. Slow Photometric Evolution

ZTF19acxpnd/AT2019wkv—This transient was reported in Andreoni et al. (2019b) after its discovery at $r = 19.4$ mag. The transient was located in the outskirts of a galaxy located at a photometric SDSS redshift of $z[p] \lesssim 0.03$, and it was ruled out due to the slow evolution shown after peaking, with $\alpha_g = 0.06$.

ZTF19acxoywk/AT2019wix—Similarly, this transient was reported in Andreoni et al. (2019b) with a discovery magnitude of $r = 19.75$ mag. It was located in the outer regions of a

galaxy with a spectroscopic redshift of $z[s] = 0.05$; however, the evolution of this transient was only $\alpha_g = -0.15$.

ZTF19acxoyra/AT2019wid—This slow-evolving transient was highlighted in Andreoni et al. (2019b) after being discovered at $r = 19.20$ mag in the nucleus of a galaxy at $z[s] = 0.09$. However, it had an almost flat evolution after reaching its peak ($\alpha_g = 0.05$).

ZTF19acxpwlh/AT2019wiy—This transient was located in a galaxy at an SDSS photometric redshift of $z[p] = 0.12$. Discovered at $g = 19.84$, it showed an almost flat evolution over the days after reaching its peak ($\alpha_r = 0.07$).

B.10. S191213g

We summarize the candidate counterparts to S191213g in Table 9 and the follow-up photometry in Table 17. Next, we discuss why we conclude that each one is unrelated.

B.10.1. Spectroscopically Classified

ZTF19acykzsk/SN2019wqj—This transient was discovered at $g = 19.25$ mag in a galaxy at $z[s] = 0.021$. It was not detected in the ultraviolet by the Swift telescope (Oates et al. 2019). The spectrum taken with the SPRAT on the LT (Perley & Copperwheat 2019b) and the GMOS-N mounted on the Gemini-North 8 m telescope (Fremling et al. 2019) showed prominent hydrogen lines and was classified as an SN II. This was later confirmed by a GTC spectrum that showed similar features (Elias-Rosa et al. 2019). Furthermore, this transient had PS1 detections ~ 1 day after the event (Smith et al. 2019). Part of the evolution of this transient was followed up by the LOT (Tan et al. 2019).

ZTF19acymaru/AT2019wnh—This transient was discovered at $r = 20.03$ mag and highlighted in Andreoni et al. (2019a). The ZTF reference image did not show a visible host. Finally, the GTC spectrum revealed an SN Ia at redshift $z[s] = 0.167$ (Castro-Tirado et al. 2019a).

ZTF19acykzsp/AT2019wne—This candidate was first highlighted in Andreoni et al. (2019a), as it was discovered at $r = 20.18$ mag. The LT/SPRAT spectrum showed an SN Ia at maximum light at $z[s] = 0.16$ (Perley & Copperwheat 2019b).

ZTF19acyfoha/AT2019wkl—Similarly, ZTF19acyfoha was reported in Andreoni et al. (2019a) at $g = 17.49$ mag. It was located in one of the arms of a spiral galaxy with a CLU redshift of $z[p] = 0.04$. The candidate was observed with the SEDM at the P60, and its spectra showed clear features of an SN Ia at $z[s] = 0.044$.

ZTF19acymcww/AT2019wni—This transient was discovered at $r = 20.24$ mag and reported in Andreoni et al. (2019a). The candidate is in the outskirts of an elliptical galaxy, and a spectrum taken with WHT revealed an SN Ia at $z[s] = 0.09$ (Brennan et al. 2019).

ZTF19acymixu/AT2019wrr—This candidate was first reported in Stein et al. (2019d), as it was discovered at $r = 19.87$ mag on top of a faint diffuse source. After

Table 17
Follow-up Photometry for S191213g Candidates

Name	IAU Name	Date	Telescope	Filter	m (AB)	σ_m	m_{lim}
ZTF19acykzsk	SN2019wqj	2,458,831.8323	P60	r	19.06	0.08	20.34
ZTF19acykzsk	SN2019wqj	2,458,831.928	LOT	g	19.37	0.10	99.0
ZTF19acykzsk	SN2019wqj	2,458,831.931	LOT	r	19.11	0.16	99.0
ZTF19acykzsk	SN2019wqj	2,458,831.935	LOT	i	19.10	0.11	99.0
ZTF19acykzsk	SN2019wqj	2,458,832.223	LOT	g	19.51	0.11	99.0
ZTF19acykzsk	SN2019wqj	2,458,832.231	LOT	r	19.10	0.14	99.0
ZTF19acykzsk	SN2019wqj	2,458,832.233	LOT	i	19.06	0.24	99.0
ZTF19acykzsk	SN2019wqj	2,458,832.2910	UVOT	v	99.0	99.0	17.2
ZTF19acykzsk	SN2019wqj	2,458,832.2910	UVOT	b	99.0	99.0	17.8
ZTF19acykzsk	SN2019wqj	2,458,832.2910	UVOT	u	99.0	99.0	17.5
ZTF19acykzsk	SN2019wqj	2,458,832.2910	UVOT	$w1$	99.0	99.0	17.5
ZTF19acykzsk	SN2019wqj	2,458,832.2910	UVOT	$m2$	99.0	99.0	18.0
ZTF19acykzsk	SN2019wqj	2,458,832.2910	UVOT	$w2$	99.0	99.0	18.1
ZTF19acymixu	AT2019wrr	2,458,832.2910	UVOT	v	99.0	99.0	19.5
ZTF19acymixu	AT2019wrr	2,458,832.2910	UVOT	b	20.10	0.4	99.0
ZTF19acymixu	AT2019wrr	2,458,832.2910	UVOT	u	99.0	99.0	19.7
ZTF19acymixu	AT2019wrr	2,458,832.2910	UVOT	$w1$	99.0	99.0	19.7
ZTF19acymixu	AT2019wrr	2,458,832.2910	UVOT	$m2$	99.0	99.0	19.7
ZTF19acymixu	AT2019wrr	2,458,832.2910	UVOT	$w2$	99.0	99.0	20.3
ZTF19acymaru	AT2019wnh	2,458,831.9682	LCOGT1m	g	19.83	0.04	21.00
ZTF19acymaru	AT2019wnh	2,458,831.9706	LCOGT1m	i	20.23	0.15	21.00
ZTF19acymaru	AT2019wnh	2,458,831.9755	LCOGT1m	r	20.11	0.05	21.00
ZTF19acyfoha	AT2019wkl	2,458,831.7544	P60	r	17.29	0.05	19.19
ZTF19acyldun	AT2019wrt	2,458,853.7823	P60	i	18.99	0.10	19.87
ZTF19acyldun	AT2019wrt	2,458,832.2910	UVOT	v	99.0	99.0	17.9
ZTF19acyldun	AT2019wrt	2,458,832.2910	UVOT	b	18.83	0.13	99.0
ZTF19acyldun	AT2019wrt	2,458,832.2910	UVOT	u	18.18	0.12	99.0
ZTF19acyldun	AT2019wrt	2,458,832.2910	UVOT	$w1$	17.62	0.11	99.0
ZTF19acyldun	AT2019wrt	2,458,832.2910	UVOT	$m2$	17.71	0.13	99.0
ZTF19acyldun	AT2019wrt	2,458,832.2910	UVOT	$w2$	18.19	0.12	99.0

~ 1.6 days, observations with Swift showed a source at $b = 20.1$ mag. However, it was later classified as an SN Ia at $z[s] = 0.14$ with a spectrum taken with the DBSP at the P200.

ZTF19acylvus/AT2019wnk—This transient was discovered at $r = 19.60$ mag, sitting on top of a faint galaxy without a known redshift. It was classified by the GTC as an SN Ia at $z[s] = 0.1$ (Castro-Tirado et al. 2019a).

ZTF19acymcna/AT2019wnn—This transient was detected at $r = 20.74$ mag in the nucleus of an elliptical galaxy. The GTC spectrum showed broad hydrogen features at $z = 0.2$, consistent with an AGN.

ZTF19acyldun/AT2019wrt—This candidate was reported with an initial magnitude of $g = 19.8$. The follow-up with the Swift telescope shown an active source in the ultraviolet (Oates et al. 2019). The observations performed by GTC discovered a source at $z[s] = 0.057$ with narrow Balmer lines consistent with a luminous blue variable (LBV; Castro-Tirado et al. 2019a), as it was also detected in 2012 by PS1. However, the source brightened to a peak absolute magnitude of ≈ -18 mag, and we revise its classification to be an SN II. It additionally faded at a rate much slower than our $\alpha = 0.3$ mag evolution threshold, with a coefficient of $\alpha_r = 0.09$.

B.10.2. Slow Photometric Evolution

ZTF19acykyzj/AT2019wrg—This candidate was discovered at $g = 20.55$ and reported in Stein et al. (2019d). It was located in the outskirts of a spiral galaxy at unknown redshift; however,

its slow magnitude evolution ($\alpha_r = -0.03$) makes this transient not relevant.

ZTF19acymapa/AT2019wro—This source was detected at $g = 20.31$ and reported in Stein et al. (2019d). To calculate the evolution of this object, we have only used the first 2 nights of data, as there are no more data on this transient. Using this Δt , we obtain a slow-evolving transient with $\alpha_r = -0.06$. Additionally, we note that the first two data points make a color consistent with $g - r = 0$.

ZTF19acymaxu/AT2019wrp—This candidate was highlighted in Stein et al. (2019d) at $r = 18.70$ mag. It is on top of a faint PS1 source, and its slow magnitude evolution of $\alpha_r = 0.03$ allows us to rule it out.

ZTF19acymlhi/AT2019wrs—The first detection of this candidate was of $r = 19.54$ mag, and its initial color was consistent with $g - r = 0$ mag. Similar to *ZTF19acymapa*, the baseline used in this case was of $\Delta t = 2$ days, and the evolution showed a slow rise of $\alpha_r = -0.17$.

B.10.3. Artifacts

ZTF19acykwsd/AT2019wnl—This transient was highlighted as an orphan source with two detections in different bands: $r = 19.42$ and $g = 19.39$ mag. We proceeded to obtain an LT/SPRAT spectrum; however, the source was not present in the acquisition image. Further investigation showed more sources around *ZTF19acykwsd* consistent with cross-talk.

B.10.4. Stellar Sources

ZTF19acykyqu/AT2019wre—This transient was detected at $g = 21.13$ mag and has a second detection 3.5 hr later at $r = 20.86$ mag. There are no more ZTF data on this object; however, there is a faint point source underneath the transient and a PS1-DR2 detection ~ 1 month before the GW event. We then consider *ZTF19acykyqu* to be related to a stellar background source.

ZTF19acykyrz/AT2019wrf—Similar to *ZTF19acykyqu*, this source sits on a PS1 source that has a previous variability history. The first PS1-reported detection was in 2010, while the last PS1-reported detection was in 2014. As the ZTF only detected this source twice, at $g = 20.97$ and $r = 20.16$ mag, we posit that this candidate is related to the PS1 source underneath.

ZTF19acykzfy/AT2019wrh—This orphan transient was first discovered at $g = 20.56$ and detected ~ 3.5 hr later at $r = 20.96$ mag. The galactic latitude of *ZTF19acykzfy* ($b = -15^\circ.73$) and a nearby ($< 3''$) detection in the PS1-DR2 catalog back the stellar origin of this transient.

ZTF19acyldum/AT2019wrn—The candidate was first reported by Stein et al. (2019d) with a magnitude of $g = 19.78$ mag. It was later detected twice: 3 hr later at $r = 19.82$ mag and 5 hr later at $g = 19.84$ mag. However, there is a PS1-DR2 detection within $1''$ in 2010 and a faint source in the ZTF reference images. Therefore, we posit this candidate as a stellar variable and thus unrelated.

B.11. S200105ae and S200115j

For candidates identified within the sky map of S200105ae and S200115j, see Anand et al. (2020).

B.12. S200213t

We summarize the candidate counterparts to S200213t in Table 10 and the follow-up photometry in Table 18. Next, we discuss why we conclude that each one is unrelated. All of the transients described for this event (S200213t) were reported in Kasliwal et al. (2020).

B.12.1. Spectroscopically Classified

ZTF20aamvqxl/AT2020ciy—This transient was first reported in Kasliwal et al. (2020), as it was discovered at $g = 20.45$ mag, in the outskirts of a potential host. With the spectra taken with GTC, Valeev et al. (2020) classified the candidate as an SN Ia at $z[s] = 0.1$.

ZTF20aamvnth/AT2020cjb—Similarly, this candidate was first reported in Kasliwal et al. (2020); however, its potential host was a faint and diffuse galaxy visible in the PS1 image of the field. A spectrum from GTC classified this candidate as an SN II at $z[s] = 0.061$ (Castro-Tirado et al. 2020).

ZTF20aamvoxx/AT2020cjc—This transient was first observed at $g = 19.99$ mag, close to the nucleus of an elliptical galaxy. Data taken with GTC classified this candidate as an SN Ia at $z[s] = 0.097$ (Valeev et al. 2020).

ZTF20aamvtip/AT2020cje—The first detection of *ZTF20aamvtip* was at $g = 20.7$ mag and faded 0.2 mag in the r band after a day. The SDSS photometric redshift of the faint host was $z[p] = 0.225$. The GTC spectra classified it as an SN Ia at $z[s] = 0.15$ (Valeev et al. 2020).

ZTF20aamvnat/AT2020ciz—This transient was discovered at $g = 18.93$ mag, and, while originally thought orphan, a faint red counterpart in the PS1 and ZTF reference image suggested a stellar origin. Additionally, it is located at $b = -5^\circ.62$, backing up the stellar hypothesis. Finally, GTC spectra showed strong hydrogen lines at $z[s] = 0$, consistent with a galactic CV (Castro-Tirado et al. 2020).

ZTF20aamvodd/AT2020cij—Similarly, this transient sits at $b = -9^\circ.53$ and has a faint red PS1 counterpart. It was later classified as a stellar flare at $z[s] = 0.0$ (Castro-Tirado et al. 2020) due to its $H\alpha$ features.

ZTF20aamvoeh/AT2020cjc—This transient was discovered at $g = 20.56$ mag on top of an elliptical galaxy. We classified the candidate as an SN Ia at $z[s] = 0.14$ using the spectrum taken with the DBSP at the P200 telescope.

ZTF20aanaltd/AT2020clt—This transient was first reported in Andreoni et al. (2020c), as it was discovered at $g = 20.81$ mag in the outskirts of a faint red galaxy. The spectrum from the LRIS at the Keck observatory revealed an SN Ia at $z[s] = 0.2$ (De 2020).

ZTF20aanaoyz/AT2020clw—This transient was discovered at $g = 21.50$ mag on top of a faint PS1 elongated source. It was classified by GTC as an SN Ia at redshift $z[s] = 0.276$ (Hu et al. 2020).

ZTF20aamvpx/AT2020clx—The first observation of this transient was at $g = 20.30$ mag in the nucleus of an elliptical galaxy. The GTC spectrum showed an SN II at redshift $z[s] = 0.074$ with prominent hydrogen features (De 2020).

ZTF20aanakcd/AT2020cmr—This candidate was discovered in the outskirts of an elongated, bright elliptical galaxy at $g = 20.70$ mag. The spectrum taken with the DBSP at the P200 classified it as an SN IIn at $z[s] = 0.077$ (Andreoni et al. 2020a).

ZTF20aanamcs/AT2020crc—This object was discovered close to the nucleus of an edge-on galaxy at $g = 21.25$ mag and $z[s] = 0.093$ and subsequently classified as an SN II (De 2020).

ZTF20aanakge/AT2020crd—This candidate was detected as an orphan at $g = 20.64$ mag. The spectrum taken with OSIRIS at the GTC classified it as an SN Ia at $z[s] = 0.1272$ (Hu et al. 2020).

B.12.2. Stellar

ZTF20aanaksk/AT2020clu—This candidate was first reported at $g = 20.48$ mag as an orphan transient. We rule out *ZTF20aanaksk*, as it has two previous detections in 2010 in the PS1-DR2 catalog, and we posit that it is related to a faint star in the background.

ZTF20aanakes/AT2020cly—This candidate was first detected at $g = 21.11$ mag and with a color consistent with $g - r = 0$. Follow-up with ARCTIC and GTC left only upper limits for this fast transient (Bellm & Graham 2020; Hu et al. 2020). However, there is an archival detection in the PS1-DR2 catalog $1''.5$ from the ZTF source. Thus, we reject this candidate.

B.12.3. Slow Photometric Evolution

ZTF20aamvmzj/AT2020cja—This transient sits at $b = -10^\circ.43$; however, it does not seem to have a PS1 or ZTF counterpart, as with the previous stellar sources. The spectra taken with Keck I+LRIS and P200 only showed a

Table 18
Follow-up Photometry for S200213t Candidates

Name	IAU Name	Date	Telescope	Filter	m (AB)	σ_m	m_{lim}
ZTF20aamvqxl	AT2020ciy	2,458,893.3371	LT	<i>i</i>	20.17	0.15	21.61
ZTF20aamvqxl	AT2020ciy	2,458,893.3406	LT	<i>g</i>	99.0	99.0	19.54
ZTF20aamvoxx	AT2020cjj	2,458,893.3733	LT	<i>i</i>	20.29	0.21	21.30
ZTF20aamvoxx	AT2020cjj	2,458,893.3751	LT	<i>r</i>	21.47	0.19	22.49
ZTF20aamvoxx	AT2020cjj	2,458,893.3768	LT	<i>g</i>	20.26	0.03	23.36
ZTF20aamvtip	AT2020cje	2,458,893.3457	LT	<i>i</i>	20.68	0.07	22.73
ZTF20aamvtip	AT2020cje	2,458,893.3475	LT	<i>r</i>	20.73	0.11	22.52
ZTF20aamvtip	AT2020cje	2,458,893.3493	LT	<i>g</i>	20.80	0.06	23.14
ZTF20aamvmzj	AT2020cja	2,458,893.3559	LT	<i>g</i>	20.45	0.05	23.10
ZTF20aamvmzj	AT2020cja	2,458,906.7200	LCO2m	<i>g</i>	20.79	0.09	20.91
ZTF20aamvmzj	AT2020cja	2,458,906.7350	LCO2m	<i>r</i>	20.32	0.09	21.30
ZTF20aamvmzj	AT2020cja	2,458,893.9607	LOT	<i>g</i>	20.37	0.10	99.0
ZTF20aamvmzj	AT2020cja	2,458,893.9607	LOT	<i>r</i>	20.58	0.14	99.0
ZTF20aamvmzj	AT2020cja	2,458,893.9607	LOT	<i>i</i>	21.02	0.51	99.0
ZTF20aamvoeh	AT2020cjc	2,458,893.3559	LT	<i>g</i>	20.45	0.05	23.10
ZTF20aamvoeh	AT2020cjc	2,458,906.7200	LCO2m	<i>g</i>	20.79	0.09	20.91
ZTF20aamvoeh	AT2020cjc	2,458,906.7350	LCO2m	<i>r</i>	20.32	0.09	21.30
ZTF20aanakwb	AT2020cls	2,458,893.9607	LOT	<i>g</i>	99.0	99.0	18.9
ZTF20aanakwb	AT2020cls	2,458,893.9607	LOT	<i>r</i>	21.12	0.32	99.0
ZTF20aanakwb	AT2020cls	2,458,893.9607	LOT	<i>i</i>	20.97	0.37	99.0
ZTF20aanaltd	AT2020clt	2,458,893.9607	LOT	<i>g</i>	21.47	0.24	99.0
ZTF20aanaltd	AT2020clt	2,458,893.9607	LOT	<i>r</i>	19.34	0.04	99.0
ZTF20aanaltd	AT2020clt	2,458,893.9607	LOT	<i>i</i>	19.98	0.12	99.0
ZTF20aanaksk	AT2020clu	2,458,893.9607	LOT	<i>g</i>	20.80	0.14	99.0
ZTF20aanaksk	AT2020clu	2,458,893.9607	LOT	<i>r</i>	20.79	0.15	99.0
ZTF20aanaksk	AT2020clu	2,458,893.9607	LOT	<i>i</i>	21.19	0.47	99.0
ZTF20aanaoyz	AT2020clw	2,458,893.9607	LOT	<i>g</i>	21.46	0.42	99.0
ZTF20aanaoyz	AT2020clw	2,458,893.9607	LOT	<i>r</i>	21.09	0.22	99.0
ZTF20aanaoyz	AT2020clw	2,458,893.9607	LOT	<i>i</i>	20.75	0.37	99.0
ZTF20aanakes	AT2020cly	2,458,894.5992	APO	<i>g</i>	99.0	99.0	23.50
ZTF20aanakes	AT2020cly	2,458,894.6012	APO	<i>i</i>	99.0	99.0	21.50
ZTF20aanakes	AT2020cly	2,458,894.6031	APO	<i>r</i>	99.0	99.0	23.00

featureless blue continuum (De 2020). It was first observed (Oates et al. 2020b) by the UVOT (Roming et al. 2005) at Swift 6.7 days after the merger, and it was only detected in the u band at $u = 19.05$ mag. It was later followed up but not detected in any bandpass (Oates et al. 2020a). Nonetheless, the magnitude evolution of the transient was otherwise flat, and it slowly faded over time with $\alpha_r = 0.04$.

ZTF20aanaqhe/AT2020cre—This transient was detected at $g = 20.88$ mag on an elliptical galaxy at a photometric redshift of $z[p] = 0.16$. Its slow rise of $\alpha_g = -0.08$ was inconsistent with the rise of a fast transient.















ZTF20aanakwb/AT2020cls—This transient was first reported in Andreoni et al. (2020c) at $g = 21.03$ mag, offset from a bright Gaia point source ($g = 15.27$ mag). This transient was detected by the LOT 12 hr later at an r -band magnitude consistent with no evolution. The initial color $g - r$ is consistent with 0 mag. In the ZTF reference image, there is a faint point source, which indicates stellar activity.

B.12.4. Outside the GW Map

ZTF20aanallx/AT2020clv—This transient was first reported in Andreoni et al. (2020c) at $g = 21.11$ mag and discovered at

a galactic latitude of $b = -11^\circ.43$. It is offset from an elliptical galaxy; however, it falls in a fairly crowded region. The rejection criterion we used for this transient is the fact that it is not within the 95% credible level of the latest LALInference map for S200213t.

ORCID iDs

Mansi M. Kasliwal  <https://orcid.org/0000-0002-5619-4938>
 Shreya Anand  <https://orcid.org/0000-0003-3768-7515>
 Tomás Ahumada  <https://orcid.org/0000-0002-2184-6430>
 Robert Stein  <https://orcid.org/0000-0003-2434-0387>
 Igor Andreoni  <https://orcid.org/0000-0002-8977-1498>
 Michael W. Coughlin  <https://orcid.org/0000-0002-8262-2924>
 Leo P. Singer  <https://orcid.org/0000-0001-9898-5597>
 Erik C. Kool  <https://orcid.org/0000-0002-7252-3877>
 Yuhan Yao  <https://orcid.org/0000-0001-6747-8509>
 Mattia Bulla  <https://orcid.org/0000-0002-8255-5127>
 Dougal Dobie  <https://orcid.org/0000-0003-0699-7019>
 Daniel A. Perley  <https://orcid.org/0000-0001-8472-1996>
 S. Bradley Cenko  <https://orcid.org/0000-0003-1673-970X>
 Varun Bhalerao  <https://orcid.org/0000-0002-6112-7609>

David L. Kaplan  <https://orcid.org/0000-0001-6295-2881>
 Jesper Sollerman  <https://orcid.org/0000-0003-1546-6615>
 Ariel Goobar  <https://orcid.org/0000-0002-4163-4996>
 Christopher M. Copperwheat  <https://orcid.org/0000-0001-7983-8698>
 Eric C. Bellm  <https://orcid.org/0000-0001-8018-5348>
 G. C. Anupama  <https://orcid.org/0000-0003-3533-7183>
 Alessandra Corsi  <https://orcid.org/0000-0001-8104-3536>
 Samaya Nissanke  <https://orcid.org/0000-0001-6573-7773>
 Sudhanshu Barway  <https://orcid.org/0000-0002-3927-5402>
 Joshua S. Bloom  <https://orcid.org/0000-0002-7777-216X>
 Kevin B. Burdge  <https://orcid.org/0000-0002-7226-836X>
 David O. Cook  <https://orcid.org/0000-0002-6877-7655>
 Jeff Cooke  <https://orcid.org/0000-0001-5703-2108>
 Virginia Cunningham  <https://orcid.org/0000-0003-2292-0441>
 Dmitry A. Duev  <https://orcid.org/0000-0001-5060-8733>
 Anna Franckowiak  <https://orcid.org/0000-0002-5605-2219>
 Sara Frederick  <https://orcid.org/0000-0001-9676-730X>
 Christoffer Fremling  <https://orcid.org/0000-0002-4223-103X>
 Avishay Gal-Yam  <https://orcid.org/0000-0002-3653-5598>
 Pradip Gatkine  <https://orcid.org/0000-0002-1955-2230>
 Shaon Ghosh  <https://orcid.org/0000-0003-4259-8592>
 Daniel A. Goldstein  <https://orcid.org/0000-0003-3461-8661>
 V. Zach Golkhou  <https://orcid.org/0000-0001-8205-2506>
 Matthew J. Graham  <https://orcid.org/0000-0002-3168-0139>
 Melissa L. Graham  <https://orcid.org/0000-0002-9154-3136>
 Matthew J. Hankins  <https://orcid.org/0000-0001-9315-8437>
 George Helou  <https://orcid.org/0000-0003-3367-3415>
 Youdong Hu  <https://orcid.org/0000-0002-7400-4608>
 Amruta Jaodand  <https://orcid.org/0000-0002-3850-6651>
 Albert K. H. Kong  <https://orcid.org/0000-0002-5105-344X>
 S. R. Kulkarni  <https://orcid.org/0000-0001-5390-8563>
 Brajesh Kumar  <https://orcid.org/0000-0001-7225-2475>
 Russ R. Laher  <https://orcid.org/0000-0003-2451-5482>
 Ashish Mahabal  <https://orcid.org/0000-0003-2242-0244>
 Frank J. Masci  <https://orcid.org/0000-0002-8532-9395>
 Adam A. Miller  <https://orcid.org/0000-0001-9515-478X>
 Kunal Mooley  <https://orcid.org/0000-0002-2557-5180>
 Jeffrey A. Newman  <https://orcid.org/0000-0001-8684-2222>
 Chow-Choong Ngeow  <https://orcid.org/0000-0001-8771-7554>
 Elena Pian  <https://orcid.org/0000-0001-8646-4858>
 Reed Riddle  <https://orcid.org/0000-0002-0387-370X>
 Maayane T. Soumagnac  <https://orcid.org/0000-0001-6753-1488>
 Anastasios Tzanidakis  <https://orcid.org/0000-0003-0484-3331>
 Eleonora Troja  <https://orcid.org/0000-0002-1869-7817>
 Sara Webb  <https://orcid.org/0000-0003-2601-1472>
 Po-Chieh Yu  <https://orcid.org/0000-0001-8894-0854>
 Bin-Bin Zhang  <https://orcid.org/0000-0003-4111-5958>
 Rongpu Zhou  <https://orcid.org/0000-0001-5381-4372>

References

- Abbott, B. P., Abbott, R., Abbott, T. D., et al. 2017a, *ApJL*, **848**, L12
 Abbott, B. P., Abbott, R., Abbott, T. D., et al. 2018, *LRR*, **21**, 3
 Abbott, B. P., Abbott, R., Abbott, T. D., et al. 2020a, *ApJL*, **892**, L3
 Abbott, B. P., Abbott, R., Abbott, T. D., et al. 2016, *PhRvL*, **116**, 061102
 Abbott, B. P., Abbott, R., Abbott, T. D., et al. 2017b, *PhRvL*, **119**, 161101
 Abbott, B. P., Abbott, T. D., Abraham, S., et al. 2020b, *ApJL*, **896**, L44
 Ahumada, R., Allende Prieto, C., Almeida, A., et al. 2020, *ApJS*, **249**, 3
 Allington-Smith, J., Murray, G., Content, R., et al. 2002, *PASP*, **114**, 892
 Almualla, M., Coughlin, M. W., Anand, S., et al. 2020, *MNRAS*, **495**, 4366
 Anand, S., Andreoni, I., Khandagale, M., et al. 2019, GCN, 25706, 1
 Anand, S., Coughlin, M. W., Kasliwal, M. M., et al. 2020, *NatAs*, in press, doi:10.1038/s41550-020-1183-3
 Andreoni, I., Ackley, K., Cooke, J., et al. 2017, *PASA*, **34**, e069
 Andreoni, I., Anand, S., Bellm, E., et al. 2019a, GCN, 26424, 1
 Andreoni, I., Anand, S., Coughlin, M. W., et al. 2019b, GCN, 26416, 1
 Andreoni, I., De, K., Kasliwal, M., Huang, Y., & Liu, X. 2020a, GCN, 27075, 1
 Andreoni, I., Goldstein, D., Anand, S., et al. 2019c, *ApJL*, **881**, L16
 Andreoni, I., Goldstein, D. A., Kasliwal, M. M., et al. 2020b, *ApJ*, **890**, 131
 Andreoni, I., Kumar, H., Karambelkar, V., et al. 2020c, GCN, 27065, 1
 Antier, S., Agayeva, S., AlMualla, M., et al. 2020, arXiv:2004.04277
 Arcavi, I. 2018, *ApJL*, **855**, L23
 Arcavi, I., Hosseinzadeh, G., Howell, D. A., et al. 2017, *Natur*, **551**, 64
 Assef, R. J., Stern, D., Noiro, G., et al. 2018, *ApJS*, **234**, 23
 Bailer-Jones, C. A. L., Fouesneau, M., & Andrae, R. 2019, *MNRAS*, **490**, 5615
 Becker, A. 2015, HOTPANTS: High Order Transform of PSF ANd Template Subtraction, Astrophysics Source Code Library, ascl:1504.004
 Bellm, E. C., & Graham, M. 2020, GCN, 27118, 1
 Bellm, E. C., Kulkarni, S. R., Graham, M. J., et al. 2018, *PASP*, **131**, 018002
 Bellm, E. C., & Sesar, B. 2016, pyraf-dbsp: Reduction Pipeline for the Palomar Double Beam Spectrograph, Astrophysics Source Code Library, ascl:1602.002
 Bertin, E. 2006, in ASP Conf. Series 351, Astronomical Data Analysis Software and Systems XV, ed. C. Gabriel et al. (San Francisco, CA: ASP), 112
 Bertin, E. 2011, in ASP Conf. Ser. 442, Astronomical Data Analysis Software and Systems XX, ed. I. N. Evans et al. (San Francisco, CA: ASP), 435
 Bertin, E., & Arnouts, S. 2010, SExtractor: Source Extractor, Astrophysics Source Code Library, ascl:1010.064
 Bertin, E., Mellier, Y., Radovich, M., et al. 2002, in ASP Conf. Ser. 281, Astronomical Data Analysis Software and Systems XI, ed. D. A. Bohlender, D. Durand, & T. H. Handley (San Francisco, CA: ASP), 228
 Blagorodnova, N., Neill, J. D., Walters, R., et al. 2018, *PASP*, **130**, 035003
 Blondin, S., & Tonry, J. L. 2007, *ApJ*, **666**, 1024
 Brennan, S., Killestein, T., Fraser, M., et al. 2019, GCN, 26429, 1
 Broekgaarden, F. S., Justham, S., de Mink, S. E., et al. 2019, *MNRAS*, **490**, 5228
 Brown, T. M., Baliber, N., Bianco, F. B., et al. 2013, *PASP*, **125**, 1031
 Buckley, D. A. H., Hearnshaw, J. B., Nordsieck, K. H., & O'Donoghue, D. 2003, *Proc. SPIE*, **4834**, 264
 Bulla, M. 2019, *MNRAS*, **489**, 5037
 Burdge, K., Perley, D. A., & Kasliwal, M. 2019, GCN, 25639, 1
 Burgh, E. B., Nordsieck, K. H., Kobulnicky, H. A., et al. 2003, *Proc. SPIE*, **4841**, 1463
 Cannizzaro, G., Pastor-Marazuela, I., Jonker, P., Maguire, K., & Fraser, M. 2019, GCN, 25725, 1
 Cao, Y., Nugent, P. E., & Kasliwal, M. M. 2016, *PASP*, **128**, 114502
 Castro-Tirado, A., Hu, Y.-D., Valeev, A., et al. 2019a, GCN, 26492, 1
 Castro-Tirado, A., Hu, Y.-D., Valeev, A., et al. 2020, GCN, 27063, 1
 Castro-Tirado, A., Valeev, A., Sokolov, V., et al. 2019b, GCN, 25721, 1
 Cenko, S. B., Fox, D. B., Moon, D.-S., et al. 2006, *PASP*, **118**, 1396
 Cepa, J., Aguiar, M., Castañeda, H., et al. 2005, *RMxAA*, **24**, 1
 Chambers, K. C., Magnier, E. A., Metcalfe, N., et al. 2016, arXiv:1612.05560
 Chatterjee, D., Ghosh, S., Brady, P. R., et al. 2020, *ApJ*, **896**, 54
 Cook, D. O., Kasliwal, M. M., Van Sistine, A., et al. 2019, *ApJ*, **880**, 7
 Coughlin, M. W., Ahumada, T., Cenko, S. B., et al. 2019a, *PASP*, **131**, 048001
 Coughlin, M. W., Dekany, R. G., Duev, D. A., et al. 2019b, *MNRAS*, **485**, 1412
 Coughlin, M. W., Kasliwal, M. M., Perley, D. A., et al. 2019c, GCN, 24283, 1
 Coughlin, M. W., Ahumada, T., Anand, S., et al. 2019d, *ApJL*, **885**, L19
 Coughlin, M. W., Tao, D., Chan, M. L., et al. 2018, *MNRAS*, **478**, 692
 Coulter, D. A., Foley, R. J., Kilpatrick, C. D., et al. 2017, *Sci*, **358**, 1556
 Cowperthwaite, P. S., Berger, E., Villar, V. A., et al. 2017, *ApJL*, **848**, L17
 Crawford, S. M., Still, M., Schellart, P., et al. 2010, *Proc. SPIE*, **7737**, 25
 Cushing, M. C., Vacca, W. D., & Rayner, J. T. 2004, *PASP*, **116**, 362
 De, K. 2020, GCN, 27140, 1
 De, K., Hankins, M. J., Kasliwal, M. M., et al. 2020a, *PASP*, **132**, 025001
 De, K., Kasliwal, M. M., Ofek, E. O., et al. 2018, *Sci*, **362**, 201
 De, K., Kasliwal, M. M., Tzanidakis, A., et al. 2020b, arXiv:2004.09029
 Díaz, M. C., Macri, L. M., Garcia Lambas, D., et al. 2017, *ApJL*, **848**, L29

- Dietrich, T., Coughlin, M. W., Pang, P. T. H., et al. 2020, arXiv:2002.11355
- Djorgovski, S. G., Drake, A. J., Mahabal, A. A., et al. 2011, arXiv:1102.5004
- Dobie, D., Stewart, A., Murphy, T., et al. 2019, *ApJL*, **887**, L13
- Drout, M. R., Piro, A. L., Shappee, B. J., et al. 2017, *Sci*, **358**, 1570
- Duev, D. A., Mahabal, A., Masci, F. J., et al. 2019, *MNRAS*, **489**, 3582
- Elias-Rosa, N., Benetti, S., Piranomonte, S., et al. 2019, GCN, 26428, 1
- Evans, P. A., Cenko, S. B., Kennea, J. A., et al. 2017, *Sci*, **358**, 1565
- Feindt, U., Nordin, J., Rigault, M., et al. 2019, *JCAP*, **2019**, 005
- Fernández, R., Foucart, F., & Lippuner, J. 2020, *MNRAS*, **497**, 3221
- Flewelling, H. 2018, AAS Meeting, **231**, 436.01
- Foucart, F. 2012, *PhRvD*, **86**, 124007
- Foucart, F., Hinderer, T., & Nissanke, S. 2018, *PhRvD*, **98**, 081501
- Fremling, C., Ahumada, T., Singer, L., De, K., & Kasliwal, M. 2019, GCN, 26427, 1
- Fremling, C., Sollerman, J., Taddia, F., et al. 2016, *A&A*, **593**, A68
- Fremling, U. C., Miller, A. A., Sharma, Y., et al. 2020, *ApJ*, **895**, 32
- Gaia Collaboration 2018, *yCat*, I/345
- Gehrels, N., Chincarini, G., Giommi, P., et al. 2004, *ApJ*, **611**, 1005
- Jimeno, G., Roth, K., Chiboucas, K., et al. 2016, *Proc. SPIE*, **9908**, 99082S
- Goldstein, A., Veres, P., Burns, E., et al. 2017, *ApJL*, **848**, L14
- Goldstein, D. A., Andreoni, I., Nugent, P. E., et al. 2019, *ApJ*, **881**, L7
- Gompertz, B., Cutter, R., Steeghs, D., et al. 2020, *MNRAS*, **497**, 726
- Graham, M. J., Ford, K. E. S., McKernan, B., et al. 2020, *PhRvL*, **124**, 251102
- Graham, M. J., Kulkarni, S. R., Bellm, E. C., et al. 2019, *PASP*, **131**, 078001
- Guevel, D., & Hosseinzadeh, G. 2017, Dguevel/Pyzogy: Initial Release, v0.0.1, Zenodo, doi:10.5281/zenodo.1043973
- Haggard, D., Nynka, M., Ruan, J. J., et al. 2017, *ApJL*, **848**, L25
- Hallinan, G., Corsi, A., Mooley, K. P., et al. 2017, *Sci*, **358**, 1579
- Hook, I. M., Jørgensen, I., Allington-Smith, J. R., et al. 2004, *PASP*, **116**, 425
- Hotokozaka, K., Kyutoku, K., Tanaka, M., et al. 2013, *ApJL*, **778**, L16
- Hu, Y., Valeev, A., Castro-Tirado, A., et al. 2019a, GCN, 26502, 1
- Hu, Y.-D., Castro-Tirado, A., Valeev, A., et al. 2020, GCN, 27154, 1
- Hu, Y. D., Castro-Tirado, A. J., Valeev, A. F., et al. 2019b, GCN, 24359, 1
- Hu, Y.-D., Valeev, A., Castro-Tirado, A., et al. 2019c, GCN, 26422, 1
- Huang, K., Urata, Y., Ip, W., et al. 2005, *NCiMc*, **28**, 731
- Huehnerhoff, J., Ketzbeck, W., Bradley, A., et al. 2016, *Proc. SPIE*, **9908**, 99085H
- Izzo, L., Leloudas, G., Bruun, S., et al. 2019, GCN, 25675, 1
- Jedicke, R., Bolin, B., Granvik, M., & Beshore, E. 2016, *Icar*, **266**, 173
- Karambelkar, V., De, K., Van Roestel, J., & Kasliwal, M. 2019a, GCN, 25921, 1
- Karambelkar, V., De, K., van Roestel, J., & Kasliwal, M. M. 2019b, GCN, 25931, 1
- Kasen, D., Metzger, B., Barnes, J., Quataert, E., & Ramirez-Ruiz, E. 2017, *Natur*, **551**, 80
- Kasliwal, M. M., Cannella, C., Bagdasaryan, A., et al. 2019a, *PASP*, **131**, 038003
- Kasliwal, M. M., Cenko, S. B., Singer, L. P., et al. 2016, *ApJL*, **824**, L24
- Kasliwal, M. M., Kasen, D., Lau, R. M., et al. 2019b, *MNRAS*, in press, doi:10.1093/mnras/stz007
- Kasliwal, M. M., Nakar, E., Singer, L. P., et al. 2017, *Sci*, **358**, 1559
- Kasliwal, M. M., & Nissanke, S. 2014, *ApJL*, **789**, L5
- Kasliwal, M. M., Perley, D., Kumar, H., et al. 2020, GCN, 27051, 1
- Kawaguchi, K., Kyutoku, K., Shibata, M., & Tanaka, M. 2016, *ApJ*, **825**, 52
- Kiuchi, K., Sekiguchi, Y., Kyutoku, K., et al. 2015, *PhRvD*, **92**, 064034
- Kruckow, M. U., Tauris, T. M., Langer, N., Kramer, M., & Izzard, R. G. 2018, *MNRAS*, **481**, 1908
- Law, N. M., Kulkarni, S. R., Dekany, R. G., et al. 2009, *PASP*, **121**, 1395
- Levan, A. 2020, PoS, Asterics2019, 044
- Ligo Scientific Collaboration, & VIRGO Collaboration 2019a, GCN, 24237, 1
- Ligo Scientific Collaboration, & VIRGO Collaboration 2019b, GCN, 24411, 1
- Lipunov, V. M., Gorbvskoy, E., Kornilov, V. G., et al. 2017, *ApJL*, **850**, L1
- Lundquist, M. J., Paterson, K., Fong, W., et al. 2019, *ApJL*, **881**, L26
- Mahabal, A., Rebbapragada, U., Walters, R., et al. 2019, *PASP*, **131**, 038002
- Margutti, R., Berger, E., Fong, W., et al. 2017, *ApJL*, **848**, L20
- Masci, F. J., Laher, R. R., Rebbapragada, U. D., et al. 2017, *PASP*, **129**, 014002
- Masci, F. J., Laher, R. R., Rusholme, B., et al. 2018, *PASP*, **131**, 018003
- Massey, P., Dunham, E., Bida, T., et al. 2013, AAS Meeting, **221**, 345.02
- Mazaeva, E., Pozanenko, A., Rummyantsev, V., Belkin, S., & Volnova, A. 2019, GCN, 25943, 1
- Mooley, K. P., Frail, D. A., Dobie, D., et al. 2018, *ApJL*, **868**, L11
- Moore, A. M., & Kasliwal, M. M. 2019, *NatAs*, **3**, 109
- Muthukrishna, D., Parkinson, D., & Tucker, B. E. 2019, *ApJ*, **885**, 85
- Nakaoka, T., Maeda, K., Yamanaka, M., et al. 2020, arXiv:2005.02992
- Nakar, E. 2020, *PhR*, **886**, 1
- Naoz, S. 2016, *ARA&A*, **54**, 441
- Nissanke, S., Kasliwal, M., & Georgieva, A. 2013, *ApJ*, **767**, 124
- Nordin, J., Brinnel, V., van Santen, J., et al. 2019, *A&A*, **631**, A147
- Oates, S., Klingler, N., Page, K., et al. 2020a, GCN, 27400, 1
- Oates, S., Page, K., Breeveld, A., et al. 2020b, GCN, 27153, 1
- Oates, S., Page, K., De Pasquale, M., et al. 2019, GCN, 26471, 1
- Oke, J. B., Cohen, J. G., Carr, M., et al. 1995, *PASP*, **107**, 375
- Patterson, M. T., Bellm, E. C., Rusholme, B., et al. 2019, *PASP*, **131**, 018001
- Perley, D., & Copperwheat, C. 2019a, GCN, 25720, 1
- Perley, D., & Copperwheat, C. 2019b, GCN, 26426, 1
- Perley, D. A. 2019, *PASP*, **131**, 084503
- Perley, D. A., Goobar, A., Kasliwal, M. M., et al. 2019a, GCN, 24331, 1
- Perley, D. A., Ho, A. Y. Q., & Copperwheat, C. M. 2019b, GCN, 25643, 1
- Pian, E., D'Avanzo, P., Benetti, S., et al. 2017, *Natur*, **551**, 67
- Piascik, A. S., Steele, I. A., Bates, S. D., et al. 2014, *Proc. SPIE*, **9147**, 91478H
- Piro, A. L., & Kollmeier, J. A. 2018, *ApJ*, **855**, 103
- Pozanenko, A. S., Barkov, M. V., Minaev, P. Y., et al. 2018, *ApJL*, **852**, L30
- Rhodes, L., Fender, R., Williams, D., et al. 2019, GCN, 24226, 1
- Rigault, M., Neill, J. D., Blagorodnova, N., et al. 2019, *A&A*, **627**, A115
- Roming, P. W. A., Kennedy, T. E., Mason, K. O., et al. 2005, *SSRv*, **120**, 95
- Rosell, M. J. B., Rostopchin, S., Zimmerman, A., et al. 2019, GCN, 25622, 1
- Rosswog, S. 2005, *ApJ*, **634**, 1202
- Sagués Carracedo, A., Bulla, M., Feindt, U., & Goobar, A. 2020, arXiv:2004.06137
- Salsamo, I., Tomasella, L., Benetti, S., D'Avanzo, P., & Cappellaro, E. 2019a, GCN, 25618, 1
- Salsamo, I., Tomasella, L., Benetti, S., et al. 2019b, GCN, 25619, 1
- Schlafly, E. F., & Finkbeiner, D. P. 2011, *ApJ*, **737**, 103
- Shappee, B. J., Prieto, J. L., Grupe, D., et al. 2014, *ApJ*, **788**, 48
- Singer, L. P., Kasliwal, M. M., Cenko, S. B., et al. 2015, *ApJ*, **806**, 52
- Singer, L. P., & Price, L. R. 2016, *PhRvD*, **93**, 024013
- Skrutskie, M. F., Cutri, R. M., Stiening, R., et al. 2006, *AJ*, **131**, 1163
- Smartt, S., Srivastav, S., Smith, K., et al. 2019, GCN, 25922, 1
- Smartt, S. J., Chen, T. W., Jerkstrand, A., et al. 2017, *Natur*, **551**, 75
- Smith, K., Smartt, S., Young, D., et al. 2019, GCN, 26430, 1
- Soares-Santos, M., Holz, D. E., Annis, J., Chornock, R., & Herner, K. 2017, *ApJL*, **848**, L16
- Soumagnac, M. T., & Ofek, E. O. 2018, *PASP*, **130**, 075002
- Steele, I. A., Smith, R. J., Rees, P. C., et al. 2004, *Proc. SPIE*, **5489**, 679
- Stein, R., Andreoni, I., Coughlin, M., et al. 2019a, GCN, 25727, 1
- Stein, R., Kasliwal, M. M., Kool, E., et al. 2019b, GCN, 25899, 1
- Stein, R., Kool, E., Kumar, H., et al. 2019c, GCN, 25656, 1
- Stein, R., Reusch, S., Perley, D., Andreoni, I., & Coughlin, M. 2019d, GCN, 26437, 1
- Stein, R., van Velzen, S., Kowalski, M., et al. 2020, arXiv:2005.05340
- Stephan, A. P., Naoz, S., Ghez, A. M., et al. 2019, *ApJ*, **878**, 58
- Tachibana, Y., & Miller, A. A. 2018, *PASP*, **130**, 128001
- Tan, H.-J., Kong, A., Ngeow, C.-C., & Ip, W.-H. 2019, GCN, 26431, 1
- Tauris, T. M., Langer, N., & Podsiadlowski, P. 2015, *MNRAS*, **451**, 2123
- Tonry, J. L., Denneau, L., Heinze, A. N., et al. 2018, *PASP*, **130**, 064505
- Troja, E., Piro, L., van Eerten, H., et al. 2017, *Natur*, **551**, 71
- Utsumi, Y., Tanaka, M., Tominaga, N., et al. 2017, *PASJ*, **69**, 101
- Vacca, W. D., Cushing, M. C., & Rayner, J. T. 2003, *PASP*, **115**, 389
- Valeev, A., Hu, Y., Castro-Tirado, A., et al. 2020, GCN, 27060, 1
- Valeev, A., Hu, Y.-D., Castro-Tirado, A., et al. 2019, GCN, 25731, 1
- Valenti, S., David, J. S., Yang, S., et al. 2017, *ApJL*, **848**, L24
- Veitch, J., Raymond, V., Farr, B., et al. 2015, *PhRvD*, **91**, 042003
- Waxman, E., Ofek, E. O., Kushnir, D., & Gal-Yam, A. 2018, *MNRAS*, **481**, 3423
- Wei, J., Xin, L., Antier, S., et al. 2019, GCN, 25640, 1
- West, A. A., Morgan, D. P., Bochanski, J. J., et al. 2011, *AJ*, **141**, 97
- Wilson, J. C., Eikenberry, S. S., Henderson, C. P., et al. 2003, *Proc. SPIE*, **4841**, 451
- Wright, E. L., Eisenhardt, P. R. M., Mainzer, A. K., et al. 2010, *AJ*, **140**, 1868
- Yao, Y., De, K., Kasliwal, M. M., et al. 2020, arXiv:2005.12922
- Yao, Y., Miller, A. A., Kulkarni, S. R., et al. 2019, *ApJ*, **886**, 152
- Zackay, B., Ofek, E. O., & Gal-Yam, A. 2016, *ApJ*, **830**, 27
- Zhou, R., Newman, J. A., Mao, Y.-Y., et al. 2020, arXiv:2001.06018